Laser-induced Acoustic Transient by Facilitated Heat Transfer in Nanocomposite Materials for Cavitation and its Applications

by

Taehwa Lee

A dissertation submitted in partial fulfillment
of the requirement for the degree of
Doctor of Philosophy
(Mechanical Engineering)
in the University of Michigan
2015

Doctoral Committee:

Professor L. Jay Guo, Chair
Professor Katsuo Kurabayashi
Professor Kevin Pipe
Professor Xueding Wang

To my grandmother, whom I lost in the middle of my study,

and my family

Acknowledgements

It has been a great pleasure to tirelessly work with people at the University of University. Eventually, it is more than happy to reach this point and have an opportunity to express my gratitude to those who made this thesis possible. First and foremost, I would like to appreciate my advisor Professor L. Jay Guo for supporting me. I cannot thank him enough for his guidance and encouragement, which have been wonderful nutrients to my research and intellectual growth. Also, I would like to say that his insightful questions have always deserved good answers.

I would like to thank my committee members, Prof. Katsuo Kurabayashi, Prof. Kevin Pipe, and Xueding Wang for their invaluable suggestions and discussion throughout this study. Also, I would like to thank my previous advisors in Korea who had guided me. I cannot forget Prof. Donsik Kim, Prof. Moohan Kim, Prof. Simon Song who had advised me to find the right direction.

My special thanks goes to four persons: Prof. Hyoung Won Baac, Prof. Hong Seok Youn, and Dr. Jaeyong Lee. Not only did they help me shape my research, but also motivated me with indispensable support.

I am grateful to my past and current nanogroup members, Dr. Jong G. Ok, Dr. Jing Zhou, Dr. Masanori Fukuda, Dr. Wei Luo, Dr. Sung-Liang Chen, Dr. Tao Ling, Dr.

Alex F. Kaplan, Dr. Moon Kyu Kwak, Dr. Yi-Kuei Wu, Dr. Young Jae Shin, Dr. Yeotaek Yoon, Dr. Hui Joon Park, Dr. Youngki Hong, Dr. Dewei Zhao, Dr. Kyeong Jae Byun, Andrew E. Hollowell, Ashwin Panday, Cheng Zhang, Fan Yang, Yang Yang, Christina M. Jones, Chad M. Huard, Hyunsoo Kim, Kyeongwoon Jeong, Kyu-Tae Lee, Long Chen, Taehee Jang, Sangeon Lee, Hun Kim, Yeonjoon Jeong, Sunghyun Nam, Qiaochu Li, Chengang Ji, Suneel Joglekar Xi Chen, Zhong, Qingyu, Qingyu, Xiaodong Liu, Seongyong Seo for their kindness and help for my study.

Lastly, I am indebted to my parents, wife, son and all of my family for their love and support.

TABLE OF CONTENTS

LIST OF FIGURES

cavity lengths show different colors. (b) Light absorption spectrum. With the cavity length increased, the resonance frequency is red-shifted. (c) Measured acoustic pressure amplitude for different cavity lengths (without Al reflector: square symbol, with Al reflector: circular symbol). (d) Measured light absorption (at an optical wavelength of 532 nm). The dashed line is obtained by simulation.

Fig. 3.1 (a) Experimental setup for photoacoustic generation and measurement. A 6-ns pulsed laser is illuminated through an aperture (1 mm in diameter) to samples consisting of a metal layer (Cr 100 nm) and adjacent PDMS layer. Photoacoustic signals are measured by a PVDF broadband detector in the far field (the distance between the samples and the detector is 10 mm; the laser spot size is 1 mm). (b) Samples for the different boundary conditions using different backing materials: Glass for hard boundary, air for soft boundary, water for radiation boundary. The boundary conditions differ based on acoustic impedance difference between backing materials and the PDMS layers because the thin metal layer is acoustically transparent (metal layer thickness is much smaller than acoustic wavelength); hard boundary ($Z_{glass} \gg Z_{PDMS}$), soft boundary ($Z_{air} \ll Z_{PDMS}$), and radiation boundary ($Z_{water} \sim Z_{PDMS}$). (c) The measured photoacoustic signals for the different boundary conditions.

Fig. 3.2 (a) Photoacoustic generation for varying water layer in the air side (the water layer will be referred to as matching layer). The light absorber used here is a composite composed of PDMS and carbon nanotube fillers. Since the acoustic impedance of PDMS is similar to that of water, no significant reflection between the PDMS-based absorber and the water layer occurs. (b) Schematics of the phase cancellation. The two oppositely propagating waves (F, forward wave; B, backward wave) are simultaneously generated. The backward wave is reflected with a π phase shift (or polarity reversal) from the air-backed interface (B), cancelling the original forward-going wave. By varying the water matching layer thickness (d_m), photoacoustic signals are measured (c) and simulated (d). (e) Out-coupling efficiency (η) for different water matching layer thickness, defined by a ratio of the peak negative amplitude (P_0) to the peak negative amplitude for radiation boundary ($P_{R,0}$), i.e., $\eta = P_0/P_{R,0}$. The maximum out-coupling efficiency arises at $d_m = 0.5c\tau$. (f) Measured photoacoustic signals for the soft boundary with and without a PDMS matching layer. The photoacoustic amplitude for the sample with the matching layer is an order of magnitude larger than that for without the matching layer.

Fig. 3.3 Illustration of the phase cancellation in cylindrical and spherical objects. Two oppositely propagating waves (I: inward and O: outward) are produced by pulsed symmetric heating. As going through the center, the inward wave experiences a phase, then immediately following the original outward wave. For the spherical wave, a π phase shift (or polarity reversal) occurs, while for the cylindrical wave, a π/2 phase shift (bipolar waveform) occurs. The wave with the phase shift can interfere with the other wave, which depends

ABSTRACT

Owing to their exceptional ability to convert light to sound, polymer-based nanocomposites have been used for producing high-amplitude focused sound waves (positive amplitude: > 50 MPa, focal spot: < 100 μm) by pulsed laser beam irradiation. This laser-induced focused sound shows great promise in non-invasive micro-surgery. To realize this promise, scalable, robust, and highly efficient light-to-sound (photoacoustic) converters are called for. This thesis work addresses these issues while focusing on three main topics: (1) how the polymeric composites can be designed on the basis of a fundamental study on the light-to-sound conversion process; (2) how the single, short pressure pulses behave and interact with matters; and (3) how those two understanding can contribute to designing optoacoustic converters applicable for targeted therapies.

More specifically, photoacoustic generation in a metal-based composite consisting of a thin metal layer and the adjacent polymer layers is investigated, with an emphasis on heat transfer and optical resonance. This study proposes a design principle for developing an efficient photoacoustic transmitter. Also, enhanced out-coupling of generated photoacoustic waves, otherwise cancelled under a certain condition, is examined for further understanding of photoacoustic generation. Moreover, focusing of a short photoacoustic pulse (< 100 ns) leads to an interesting observation of anomaly

acoustic phase shift, which could benefit the understanding of the Gouy phase shift. Then, investigation of the interaction between a focused photoacoustic pulse and impedance-mismatched boundaries follows; at a sound hard interface, controlled generation of single micro-bubbles is demonstrated; at a sound soft interface, nozzle-free liquid micro-jetting. Lastly, we demonstrate free-field cavitation and its therapeutic applications by using an optimized optoacoustic transmitter.

CHAPTER 1

Introduction

1. 1 Background and Motivation

Laser-generated ultrasound, based on light-to-sound conversion, is of great interests due to its broadband frequency spectrum as well as its wide applicability to numerous light-absorbing materials, enabling various applications ranging from non-destructive examination and testing (NDE/NDT) of materials [2] to high-resolution imaging [3,4]. Nanocomposites consisting of light absorbing fillers embedded in polymers [5-7], with mechanical robustness [6] hardly accomplished by metal films, are capable of producing tightly-focused high-amplitude sound waves, thus expanding its horizon to therapeutic applications by showing great promise in minimally-invasive, targeted therapy with cellular accuracy [1,8].

It is well known that high-intensity focused ultrasound (HIFU) has enabled non-invasive therapy by selectively ablating diseased or damaged tissue within the acoustic focal region [9,10]. However, this approach typically produces a bulky focal volume (~mm) where the applied high-intensity ultrasound energy is converted into heat undesirable for some applications (e.g., gene therapy). More recently, a pure mechanical

treatment realized by acoustic bubble has been introduced as Histrotripsy [11,12], a new treatment approach that relies on strong tensile pressure to induce bubbles without significant heat deposition. Although this approach based on piezoelectric transducers is now in the stage of clinical trial, it has several disadvantages. First, the piezoelectric approach requires a bulky system (at least several cm) composed of an array of active piezoelectric elements so as to generate pressures strong enough to produce cavitation. The bulky system can limit its endoscopic applications. Second, an acoustic vocal volume produced by relatively low frequency (a few MHz) is still quite large (a few mm), leading to the enlarged treatment. Although the actual cavitation could be even smaller than the focal dimension (since cavitation is regulated by a negative pressure zone lower than the cavitation threshold of mediums), the large focal volume can lose controllability of cavitation in presence of unexpected foreign nucleation sites within the focal volume that can reduce the cavitation threshold.

These aforementioned limitations can be circumvented by taking an optoacoustic approach, where a nanosecond laser beam is irradiated on an optoacoustic transmitter. By using an efficient light-to-sound converting material, the optoacoustic transmitter could be miniaturized for integration with the endoscopic system. Also, because of its high frequency, the acoustic pulse produced by the optoacoustic transmitter can be focused down to a point about the size of a single biological cell. Despite the potentials, the optoacoustic approach needs to be further improved for therapeutic applications, because the generated pressure amplitudes are not sufficiently high to induce bubbles without the interference effect. In fact, this approach has been limited to a certain case where the

target samples should be placed on a hard material that can amplify the incident pressure due to the interference effect. Thus, my research focuses on investigation of photoacoustic generation in nanocomposites, with an aim of designing a highly efficient photoacoustic transmitter for cavitation and its applications.

1.2 Goal and Thesis Outline

This work aims to design a high performance light-to-sound (optoacoustic) converter that is capable of producing controlled micro-cavitation applicable to practical applications (e.g., high-precision cavitation therapy), with an emphasis on studying the light-to-sound conversion process in nanocomposite materials as well as on investigating the characteristics of laser-generated pressure pulses. Detailed theoretical frameworks and methodologies, and main results are described in the following chapters.

The thesis is organized as follows: **Chapter 2** demonstrates efficient photoacoustic generation in a thin metal film-polymer composite and proposes a theoretical framework to evaluate photoacoustic conversion efficiency of materials. **Chapter 3** exhibits enhanced out-coupling of photoacoustic pulses, otherwise cancelled in the light absorbing layer. **Chapter 4** describes anomaly phase shift observed when photoacoustic pulses pass through the focus. **Chapter 5** presents the interference of focused photoacoustic pulses at impedance-mismatched boundaries, which can allow for controlled cavitation and liquid micro-jetting. **Chapter 6** describes boundary-free cavitation and its therapeutic applications. **Chapter 7** summarizes the findings and

contributions of this work from perspective of scientific significance, engineering innovation, and practical usefulness, followed by the outlook.

CHAPTER 2

Laser-induced Acoustic Transient by Pulsed Excitation of Nano-composite materials

2.1 Introduction

Photoacoustic (PA) generation (light-to-sound conversion) has been used for a myriad of applications ranging from PA imaging [3,4] and characterization of materials of any phase (e.g., photoacoustic spectroscopy [13,14]) to non-destructive evaluation and test (NDE/NDT) [2]. For those applications, knowing of PA amplitude dependence is of fundamental importance for analyzing the measured PA signals. Meanwhile, PA signals usually need to be high enough to achieve a certain level of sensitivity (noise-equivalent) or need to be as high as possible, especially for PA imaging, where higher amplitude allows for imaging targets more deeply embedded in lossy surroundings. The high-amplitude requirement is much more specific for PA cavitation therapy recently demonstrated to produce micro-cavitation for precisely ablating or killing diseased cells, by requiring pressure amplitude beyond cavitation threshold (> 20 MPa in water) [1,15]. Generating high-amplitude PA signals involves increasing light input energy or choosing materials with high light-to-sound conversion efficiency, typically with good light absorption. The former is rather simple, but the maximum allowable light input can be

limited to a specific value associated with light-induced material damages and safety limits of biomaterials (tissue damage threshold, 20 mJ/cm^2 [16]). Instead, the latter could be more feasible. For example, by engineering materials, one can increase their light absorption.

PA conversion, particularly via the thermo-elastic effect, depends on material properties such as thermal expansion coefficient and light absorption coefficient, requiring both high thermal expansion and good light absorption. Owing to their decent light absorption (e.g., > 50% light absorption for Cr 100 nm at 532 nm wavelength) and easy fabrication, thin metal films (typically, hundreds of nanometers thick) have been widely used for PA generation. Also, such thin metals allow for high-frequency signals (> 50 MHz) [5] and thus high imaging resolution, whereas thicker absorbers (or more precisely, large optical penetration depth) can broaden PA pulses [17], thereby limiting its frequency. However, metals are usually considered to be inefficient in PA conversion because of their relatively low thermal expansion. Alternatively, polymers with higher thermal expansion coefficients than metals can be used, but they are typically transparent or weakly absorbing.

To meet the requirement of both good light absorption and large thermal expansion, a composite approach has been proposed [5-7,18,19], which combines low-thermal expansion light absorbers with high-thermal expansion transparent mediums. Specifically, an early attempt was to use carbon black mixed with polydimethylsiloxane (PDMS), which showed an order of magnitude high PA amplitude compared to a Cr

absorber [5]. Recently, beside carbon black, other carbon materials including CNTs [6,18], rGO [19], nanofiber [7] have been utilized, whose excellent light absorption has resulted in high-amplitude and high-frequency PA signals. Also, the resulting high PA signal amplitudes were believed to arise from rapid heat transfer in the composites, from the carbon materials to the adjacent materials [1,6], although it has not been proven thoroughly yet due to its complexity. The highly efficient PA conversion of the carbon-based composites has been demonstrated to be applicable for PA probes with micro-sized PA sources, even on the tip of optical fibers [18], and a high-precision therapeutic modality capable of selectively removing biomaterials, cells or tissues, by PA pressure-induced cavitation [1,8,20]. However, the composite approach poses challenges to be addressed for further improvement, which could open new possibilities. For example, the composites require arduous preparation processes (e.g., CVD growth of CNT forest [6]), and thickness control of the composite films commonly prepared by spin coating, which is critical to frequency response, is also difficult [6]. Moreover, patterning of the composite films, which could be useful for PA marking by spatial patterning of PA signals [21], would require more efforts. Those challenges are not that serious for thin metal films deposited through physical vapor deposition, although they are less efficient in PA conversion than the composites.

In this work, we present a highly efficient PA conversion in a thin metal film-polymer composite comprised of a metal film embedded in polymer layers, showing a 20 dB enhancement over a Cr film. The significant increase in photoacoustic (PA) amplitudes is accomplished by 1) using very thin metal layers (but less absorptive) that

can facilitate heat transfer to surrounding materials with high PA conversion efficiency and 2) compensating weak light absorption by additional thin metal reflector forming a Fabry-Perot resonance. This high efficient metal PA transmitter could be very useful. Also, such simple structure allows theoretical analysis (especially heat transfer from the carbon materials to the surroundings), although simple analysis is available. It can give an idea of designing contrast agents (metal) and contribution of surrounding and absorbers.

2.2 Theoretical Analysis: "Figure of Merit" for Light-to-sound Conversion

2.2.1 Estimation of pressure amplitude: short and long pulse regimes

Photoacoustic generation involves a series of energy conversion processes. First, materials absorb incident optical energy that is converted into thermal energy, which in turn increases temperature and expand the materials. When the materials are heated fast before expanding (i.e., the stress confinement condition is satisfied), acoustic pressure is generated (called as the thermoelastic mechanism). Photoacoustic pressure amplitude via thermoelastic mechanism can be estimated through the momentum balance by [4,22]

$$P_0 \cong \rho c U \,, \tag{2.1}$$

where ρ is the density, c is the sound speed, and U is the speed of thermoelastic volume expansion. By plugging the speed of thermoelastic volume expansion $U = \Delta V / S\tau$ and $\Delta V = E_{th}\beta / \rho C_p$, the photoacoustic pressure amplitude can be represented by

$$P_0 = \rho c\left(\frac{F_{th}\beta c}{\rho C_p l}\right) = \left(\frac{\beta c^2}{C_p}\right)\frac{F_{th}}{l}. \tag{2.2}$$

By using the Grüneisen parameter ($\Gamma = \frac{\beta c^2}{C_p}$), the photoacoustic signal amplitude can be expressed by [4]

$$P_0 = \Gamma \cdot \left(\frac{F_{th}}{l}\right). \tag{2.3}$$

This formula indicates that photoacoustic pressure amplitude is proportional to the collective material properties (or Grüneisen parameter) and energy volume density (F_{th}/l) [J/m^3]. Thus, large Grüneisen parameter is desirable for obtaining high pressure amplitude. Also, for constant acoustic energy, smaller l has higher energy density, thereby increasing the pressure amplitude.

To choose the proper characteristic length, the temporal photoacoustic signal needs to be considered. By assuming that heat conduction is negligible, the temporal shape of the photoacoustic pulse p(t) is determined with the retardation time ($\tau = t - z/c$) by the convolution integral of temporal heating function f(t) and spatial light absorption function g(z), i.e., $\int f(c\tau - z')g(z')dz'$ [17]. The two functions are characterized by the parameters: the optical pulse duration τ and the light absorption coefficient α. For comparison, the characteristic parameters can be represented in the length scales by the acoustic penetration depth during the optical excitation $c\tau$ and the optical penetration depth $1/\alpha$, respectively. In the limiting cases, either of the two lengths is much larger than

the other such that the convolution integral leads to $l \sim \max(c\tau, 1/\alpha)$. The photoacoustic pressure amplitude can expressed by

$$P_0 = \begin{cases} \Gamma \cdot \dfrac{F_{th}}{c\tau} & (c\tau \gg 1/\alpha; \text{long pulse regime}) \\ \Gamma \cdot \dfrac{F_{th}}{1/\alpha} = \Gamma \alpha F_{th} & (c\tau \ll 1/\alpha; \text{short pulse regime}). \end{cases} \tag{2.4}$$

The pressure amplitude for the short pulse regime is commonly referred elsewhere [4]. As can be learnt from the derivation, the light absorption coefficient α is used to estimate the acoustic pulse duration rather than representing the actual light absorption. Instead, the thermal energy fluence F_{th} takes into account the light absorption (A), i.e., $F_{th} = A \cdot F$, where F is the incident optical energy fluence (although the light absorption can be influenced by the light absorption coefficient). On the other hand, the pressure amplitude for the long pulse regime is rarely used although many cases fall into this regime. The long-pulse pressure amplitude estimated from the momentum balance is consistent with that obtained by solving the governing equation [23], $P = (c\beta / C_p) I$, where I is the thermal peak power [W/m^2]. In the reference, the thermal peak power I can be approximated by F_{th}/τ, which leads to $\left(\dfrac{c\beta}{C_p}\right) I = \left(\dfrac{c^2\beta}{C_p}\right) \dfrac{F}{c\tau}$.

2.2.2 Figure of Merit

For efficient photoacoustic conversion, good light absorption and large thermal expansion coefficient are necessary. Owing to the large thermal expansion coefficient of

PDMS, PDMS-based nanocomposites are typically used [5-7,18]. However, the formula includes not only the thermal expansion coefficient, but also other material parameters, which means that large thermal expansion coefficient does not necessarily result in high photoacoustic conversion efficiency. Instead, the Grüneisen parameter is the measure of photoacoustic conversion. The table 2.1 shows the material properties. It should be noted that based on the Grüneisen parameters, gold is better than PDMS ($\Gamma_{Au}/\Gamma_{PDMS} \sim 5$). For the many cases where nanosecond laser is irradiated on small objects less than several hundreds of nanometers, the long pulse regime is satisfied. From the formula (2.4), it is noted that the characteristic length include an addition material property ($c\tau$). The capability of photoacoustic generation is determined by the Grüneisen parameters scaled by the sound speed (Γ/c). Figure 1(a) shows the scaled Gruneisen parameter as a function of the thermal expansion coefficient. Two metals (gold and silver) are still better than PDMS.

Material	Sound Speed (c) m/s	Acoustic Impedance $\left(\frac{Z}{Z_w}\right)$	Grüneisen Parameter $\left(\Gamma=\frac{\beta c^2}{c_p}\right)$ x10^{-6}
Water	1,500	1	0.111
Gold (Au)	3,240	41.7	3.391
Titanium(Ti)	6,070	18.2	1.817
Chrome (Cr)	5,940	28.5	1.426
Fused silica	5,968	8.8	0.033
PDMS	987	0.7	0.620
Parylene	2,200	1.9	0.713

Table 2.1 Material properties. Acoustic impedance is normalized to the acoustic impedance of water (Z_w).

In practice, the produced photoacoustic wave travels across an interface between different mediums. Since photoacoustic signals in water are of interest, we need to estimate the output pressure amplitude by considering acoustic transmission into water. The acoustic transmission (T_{12}) from the medium 1 to the medium 2 is represented by

$$T_{12} = \frac{2Z_2}{Z_1 + Z_2}, \tag{2.5}$$

where Z is the acoustic impedance (ρc) and the subscripts 1 and 2 correspond to the medium 1 and medium 2. This is good approximation when the medium is thick enough to neglect multiple acoustic reflection. For thin films, multiple reflection should be considered, as illustrated in Fig. 2.2. Thus, with the produced photoacoustic signal ($p(t) = P_0 f(t)$), the acoustic transmission can be represented by

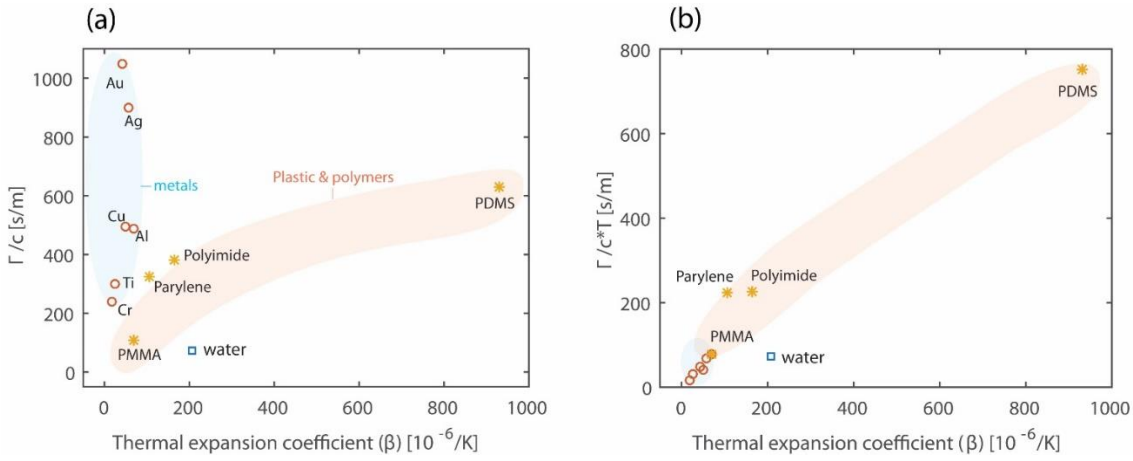

Fig.2.1 (a) The Grüneisen parameter scaled by the speed of sound. (b) The figure of merit for photoacoustic generation that considers the acoustic transmission into water.

$$p_t(t) = P_0 T_{12} f(t) + P_0 T_{12} R_{12} f(t - t_d) + P_0 T_{12} R_{12}^2 f(t - 2t_d) + \cdots$$

$$= P_0 T_{12} \sum_{n=1}^{\infty} R_{12}^{n-1} f\left[t - (n-1)t_d\right] \tag{2.6}$$

where the delay time corresponds to $t_d = 2d / c_1$. For the Gaussian temporal profile $f(t)=\exp(-t^2/\tau^2)$, the calculated transmitted pressure signals are shown in Fig. 2.3 for Parylene/water (a) and PDMS/water (b). The result is calculated by assuming that no acoustic attenuation occurs. If the delay time is much smaller than the acoustic pulse duration, transmitted photoacoustic pulses can be approximated by

$$P_t \cong P_0 \frac{T_{12}}{1 - R_{12}} = P_0 \frac{Z_2}{Z_1}. \tag{2.7}$$

Figure 2.3 shows the acoustic signals for different thicknesses. For Parylene, the acoustic signal increases with the layer thickness. It is also noted that negative phase follows positive phase.

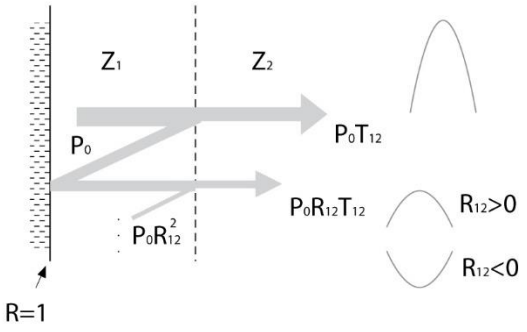

Fig. 2.2 Multiple acoustic reflection and transmission. Acoustic reflection can be either negative or positive value.

On the other hand, for PDMS, the acoustic amplitude decrease with the layer thickness and there is no negative phase. This difference arises from different acoustic reflection. As shown in Fig. 2.2, the acoustic reflection could be either negative or positive value, which depends on the relative magnitude of two acoustic impedances, i.e., if $Z_1 < Z_2$, then $R_{12} > 0$ and if $Z_1 > Z_2$, then $R_{12} < 0$. Figure 2.3(c) and (d) show the corresponding pressure amplitudes as a function of the layer thickness.

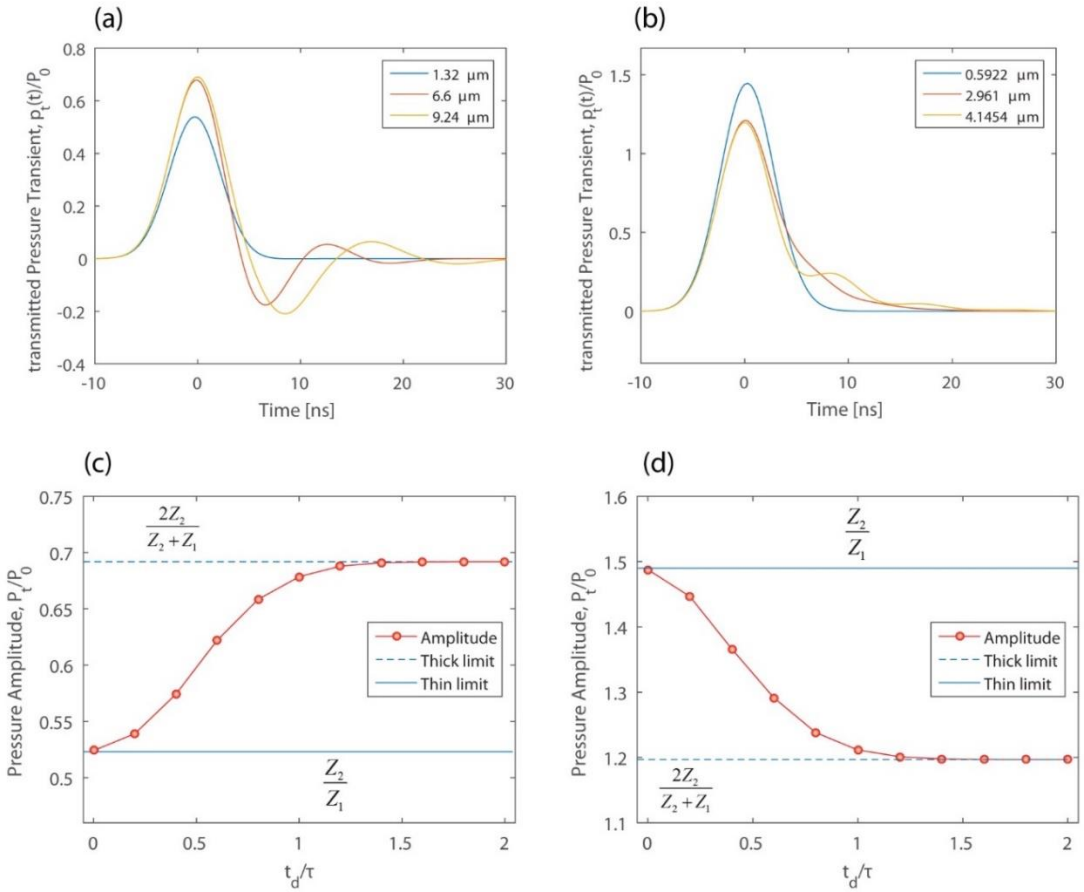

Fig. 2.3 Transmitted photoacoustic transients for Parylene/water (a) and PDMS/water (b). Pressure amplitudes for Parylene/water (c) and PDMS/water (d). The acoustic impedance of water is larger than that of Parylene and is smaller than that of PDMS, i.e., $Z_{Parylene} > Z_{water}$ and $Z_{PDMS} < Z_{water}$. For PDMS/water, $R_{12} > 0$. For Parylene/water, $R_{12} < 0$.

For thicker layer, the pressure amplitude approaches the value from the single acoustic transmission. However, for thinner layer, the pressure amplitude approaches one due to the multiple acoustic reflection. Thus, the maximum achievable acoustic transmission is expressed by

$$T_t = \max\left(\frac{2Z_2}{Z_1+Z_2}, \frac{Z_2}{Z_1}\right). \tag{2.8}$$

The output pressure amplitude can be represented by

$$P_t = A \cdot \left(\frac{\Gamma}{c}\right) \cdot T_t \cdot \frac{F}{\tau}. \tag{2.9}$$

Therefore, it is reasonable to define the figure of merit (FOM) that can be represented by

$$\eta = \left(\frac{\Gamma}{c}\right) \cdot T_t. \tag{2.10}$$

Figure 2.1(b) shows the Gruneisen parameter scaled by the sound speed and acoustic transmission (into water). Note that PDMS is an order of magnitude larger than the metals and water.

2.2.3 Heat transfer from optical absorber to surrounding medium: Green's function approach

From the FOM, the polymeric materials are better than the metal absorbers. However, the polymers are optically transparent. This issue can be addressed by combining the transparent polymers with light absorbing materials such as metals and

carbon materials. This strategy has been successfully implemented in the composites consisting of carbon fillers embedded in PDMS [5,6]. The efficient photoacoustic generation was explained by good light absorption of the fillers. Also, it is attributed to excellent heat transfer from the absorbers to the polymers, especially when the absorbing fillers are tens of nanometers in size.

To understand heat transfer, a simple structure comprised with thin metal absorber and polymers is used, as described in the inset of Fig. 2.4(a). The incident optical energy is absorbed in the thin metal layer, while some of the optical energy is loosen by optical reflection I and transmission (T), i.e., A = 1- R – T. The absorbed light energy is then converted into the thermal energy, some of which is transmitted into the adjacent PDMS layer.

$$P = P_{Metal} + P_{Polymer} = A \cdot \frac{F}{\tau}\left[\eta_M \gamma_M + \eta_P \gamma_P\right] \tag{2.11}$$

$$A \cdot F = F_{Metal} + F_{Polymer} \quad \text{or} \quad 1 = \frac{F_{Metal}}{A \cdot F} + \frac{F_{Polymer}}{A \cdot F} = \gamma_M + \gamma_P, \tag{2.12}$$

where γ is the thermal energy at each layer, normalized to the input thermal energy (M: metal and P: polymer).

Figure 2.4(a) shows the temperature distribution during the optical pulse excitation. The temperature distribution is calculated in absence of interfacial heat resistance and insulation boundary condition is applied to the left side of the metal layer. The temperature is approximately constant in the metal layer due to its high thermal

conductivity, whereas the temperature is exponentially decay from the interface. The temperature at the interface increases with time, as shown in Fig. 2.4(b). In absence of the interfacial heat transfer, the temperature of the metal layer reaches the constant temperature after the optical excitation. However, the interface temperature of the bilayer decreases after reaching the maximum temperature. The accumulated thermal energy at each layer is shown in Fig. 2.4(c).

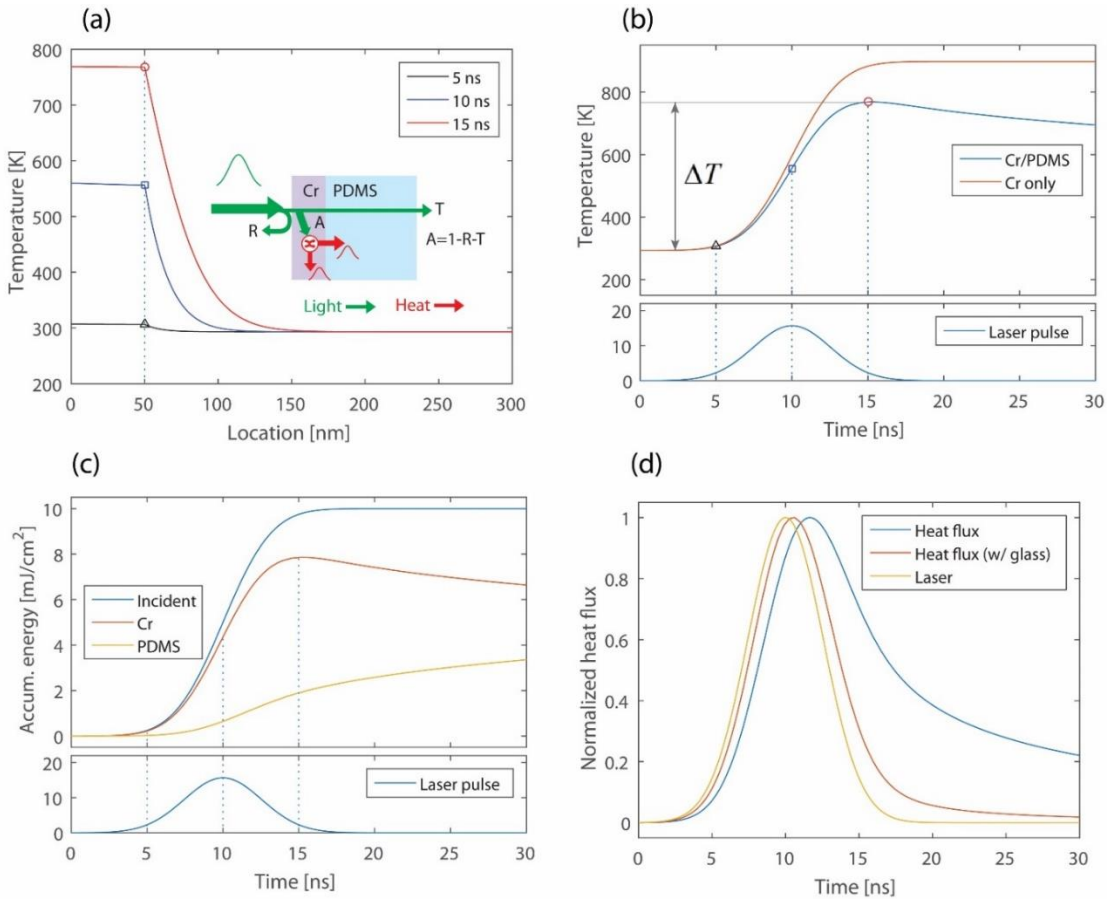

Fig. 2.4 (a) Temperature distributions at different times (t = 5, 10, 15 ns) for a bilayer composed of Cr (50 nm) and PDMS (300 nm) under a Gaussian heating pulse (pulse duration: 6 ns FWHM). (b) The corresponding temperature transient at the interface between Cr and PDMS. (c) The accumulated energy at each layer. (c) The interfacial heat flux.

During the optical excitation, the thermal energy increases for both layer. However, after the optical excitation, the thermal energy in the metal layer decreases, whereas the thermal energy in the polymer layer continues to increase. Thus, it is important to choose the right time scale that determines the output photoacoustic pressure. Since the photoacoustic signals for the long pulse regime have the same pulse duration as the optical pulse, it is reasonable to consider the thermal energy at each layer right after the pulsed optical excitation. The thermal energy in the metal layer is represented by

$$F_{Metal} = \rho C_P d \Delta T \,, \tag{2.13}$$

where ρ is the density, C_P is the heat capacity, d is the thickness, and ΔT is the maximum temperature increase.

For an infinite solid body under time-dependent surface heat flux ($f(t)$), by using the Green's function approach, the temperature increase and the appropriate Green's function ($g(z,t \mid z',t')$) are represented by

$$\Delta T(z,t) = \alpha \int_{-\infty}^{t} \frac{f(t')}{k} g(z,t \mid z',t')\, dt' \,, \tag{2.14}$$

$$g(z,t \mid z',t') = \frac{1}{\sqrt{4\pi\alpha(t-t')}} \left\{ \exp \frac{-(z-z')^2}{4\alpha(t-t')} + \exp \frac{-(z+z')^2}{4\alpha(t-t')} \right\}, \tag{2.15}$$

where α is the thermal diffusivity. We can assume that the temporal profile of the interfacial heat flux is the same as that of the optical excitation, i.e.,

$f(t) = I_P \exp\left(-t^2/\tau^2\right)$. This is reasonable, as the calculated interfacial heat flux is shown in Fig. 2.4(d). With the assumption, the surface temperature increase is simply expressed by [24]

$$\Delta T(z=0,t) = \alpha \int_{-\infty}^{t} \frac{f(t')}{k} g(z=0,t \mid z'=0,t')\,dt' = \frac{1}{\rho C_p} \int_{-\infty}^{t} \frac{f(t')}{\sqrt{\pi\alpha(t-t')}}\,dt'$$

$$= \frac{0.9394}{(8\ln 2)^{1/4}} \frac{F}{\sqrt{\rho C_p k \tau}} \left[\mathrm{e}^{-t^2/2\tau^2} D_{-1/2}\left(-\frac{\sqrt{2}t}{\tau}\right)\right] = \frac{0.9394}{(8\ln 2)^{1/4}} \frac{F}{\sqrt{\rho C_p k \tau}} \eta\left(\frac{t}{\tau}\right), \qquad (2.16)$$

where $D_\nu(x)$ is the parabolic cylinder function. After the optical pulse excitation, the surface temperature increase and the thermal energy in PDMS are represented by

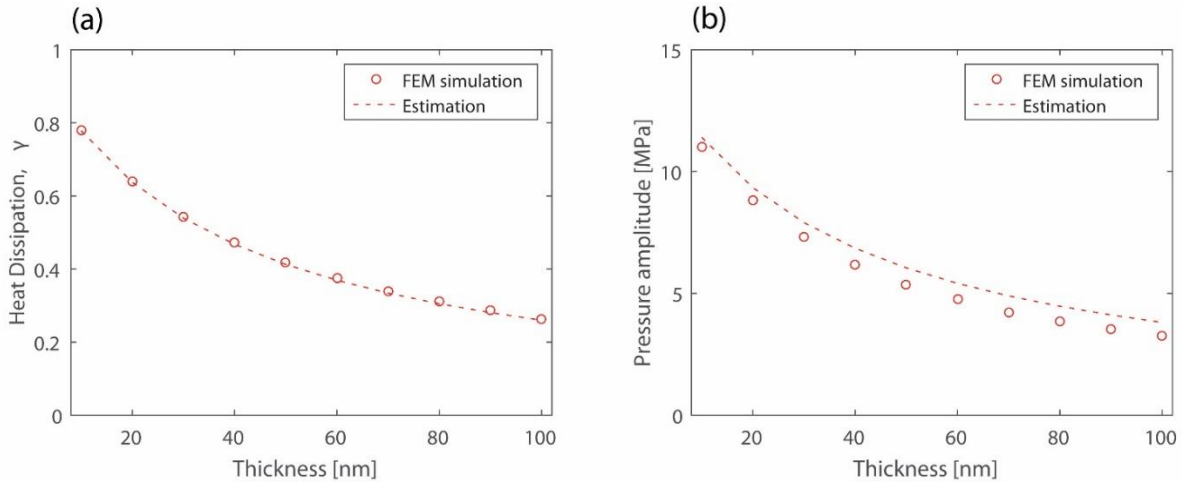

Fig. 2.5 (a) Calculated heat transfer from the metal layer to the surrounding polymer layer. (b) Calculated rressure amplitude assuming 100 % light absorption. The symbol indicates the results obtained from the FEM simulation, while the dashed line is produced by the analytic formula.

$$\Delta T_s = \Delta T\left(z=0, t=0.55\tau\right) = 0.8876\frac{F_{PDMS}}{\sqrt{\rho C_p k \tau_l}}, \tag{2.17}$$

$$F_{PDMS} = 1.1266\sqrt{\rho_p C_{p,p} k_p \tau}\Delta T_s = 1.1266\rho_p C_{p,p} l_{th}, \tag{2.18}$$

where the thermal diffusion length is $l_{th} = \sqrt{\alpha_p \tau}$. By combining the equations (2.12), (2.13), and (2.18), the thermal energy at each layer, normalized to the input thermal energy, can be represented by

$$\gamma_{metal} = \frac{\rho_m C_{p,m} d_m}{\rho_m C_{p,m} d_m + 1.1266\rho_g C_{p,g} l_{th}} \tag{2.19}$$

$$\gamma_{PDMS} = \frac{1.1266\rho_p C_{p,p} l_{th}}{\rho_m C_{p,m} d_m + 1.1266\rho_p C_{p,p} l_{th}} = \frac{1}{0.8876\frac{\rho_m C_{p,m} d_m}{\rho_p C_{p,p} l_{th}} + 1}. \tag{2.20}$$

Figure 2.5 shows the calculated γ_{PDMS} for the structure consisting of a metal sandwiched by two PDMS layers (a) and the calculated pressure amplitude (b) using the equation (2.11). For comparison, the symbol indicates the pressure amplitudes calculated by solving the differential equations through the finite element method.

2.3 Thin Metal Film-Polymer Composite

2.3.1 Ultrathin Metal Film Sandwiched by Polymers

The structure of proposed metal-based photoacoustic (PA) transmitter is

illustrated in Fig. 2.6(a), which is composed of a thin metal absorber sandwiched by two Polydimethylsiloxane (PDMS) layers (top and bottom) built on a glass substrate. On top of the top PDMS layer, a thin Al layer is deposited for optical reflection. The metal absorber between the PDMS layers converts the absorbed optical energy into heat energy, some of which is then transmitted to the surrounding PDMS layers, top and bottom. Thus, all the heated regions can collectively contribute to output photoacoustic (PA) signal. Based on an assumption that the PA conversion of PDMS is much more efficient than those of typical metals (e.g., gold, chromium, and titanium), the metal absorber is chosen to be as thin as possible in order to facilitate heat transfer to the surrounding PDMS layers. This is because the decrease in the metal thickness can reduce heat storage in the metal layer ($\sim \rho C_P d$, where ρ, C_P, and d are the mass density, specific heat capacity,: metal thickness). However, the reduced metal thickness can lead to a decrease in light absorption, which is compensated by the Al reflector. The proposed composite shows a significant enhancement of PA amplitude (~ 20 dB) compared to a bare Cr (100 nm).

Figure 2.6(b) illustrates detailed PA generation process in the proposed structure. First, incident light is trapped in an optical cavity consisting of the Al reflector and the Cr layer, and thus is absorbed mostly in the Cr layer. Note that PA pulses produced in the heated regions should pass through the metal layers. However, no significant acoustic reflection occurs, because their thicknesses are much smaller than the acoustic wavelength. Also, it is noteworthy that the heated regions produce two oppositely-propagating waves (backward and forward); and the backward wave is reflected from the glass substrate. Because the reflected wave is delayed by twice the acoustic transit time

across the bottom PDMS layer, this bottom PDMS layer needs to be thin, otherwise it could lead to broadening and reduction of output PA pulse. The thickness of the bottom PDMS layer is approximately 200 nm, and its corresponding delay is 0.4 ns. Moreover, the thickness of the top PDMS layer is chosen for optical resonance.

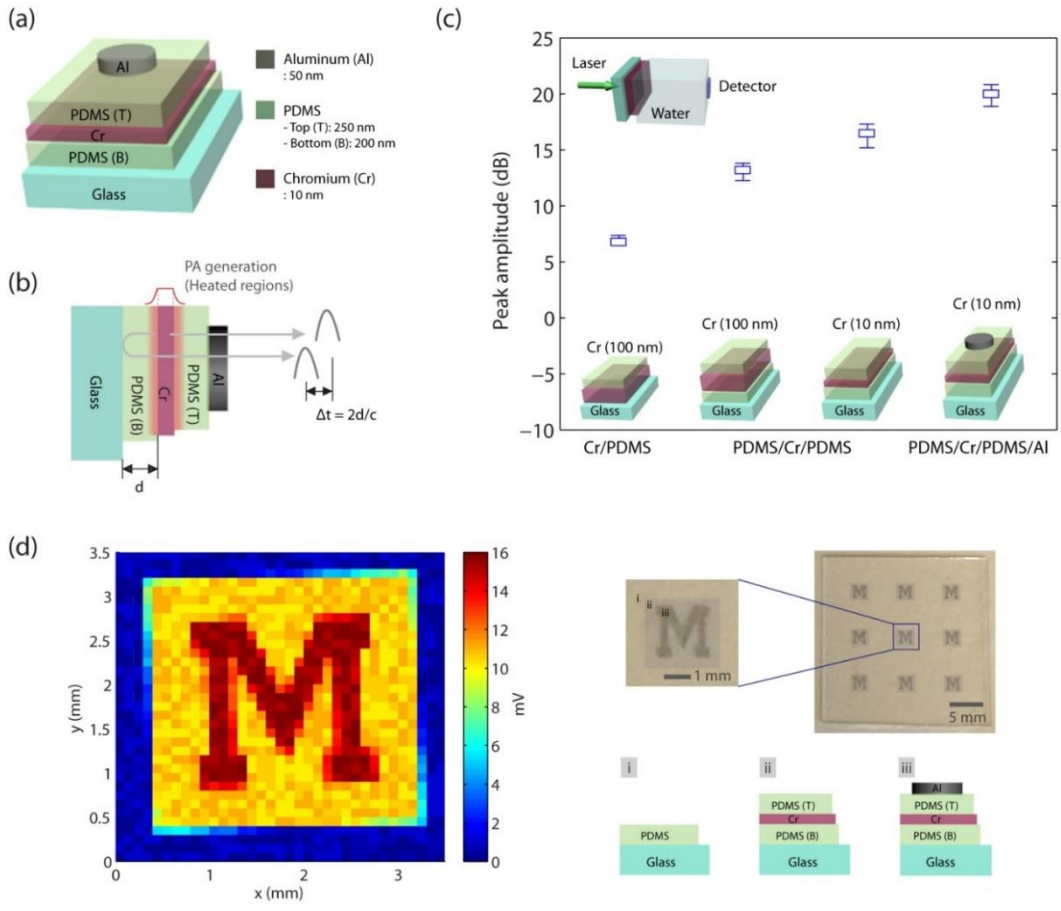

Fig. 2.6 (a) Device structure. (b) Photoacoustic signal generation. (c) Photoacoustic signal amplitudes, normalized to the bare Cr (100 nm) on a glass substrate. (d) Photoacoustic imaging of the patterned glass.

To better understand the significant enhancement of PA conversion in the proposed structure, PA amplitudes for different control samples are compared, as shown in Fig. 2.6(c). The PA signals, normalized to the peak amplitude of the bare thick metal sample (Cr 100 nm) in contact with water, are measured at laser fluence F = 2.35 mJ/cm^2. First, the Cr/PDMS sample shows approximately 6 dB increase in PA amplitude, because water is less efficient than the PDMS. Second, the two sandwiched structures are better than the Cr/PDMS sample. Here, the bottom PDMS layer can capture heat energy for PA generation, otherwise wasted in the glass substrate (negligible PA generation due to low thermal expansion coefficient).Interestingly, by comparing the two sandwiched structures, we observe that the thinner Cr layer is better because of the reduced heat storage in the Cr layer. However, the thinner Cr layer can reduce the light absorption, which is finally compensated by Al reflector forming an optical cavity. It should be empathized that the thermal management mainly contributes to the increased PA signal. The measured PA amplitude of the sandwiched structure integrated to the optical cavity is comparable to polymer composites (e.g., carbon black PDMS). This strategy introduced here could be implemented for PA imaging of implants and tools in biological samples. Also, the proposed structure could be used to create spatial PA signal patterns applicable for PA markings containing useful information[21].

To demonstrate this capability, we fabricated a school logo on the glass substrate and conducted PA imaging of it. Here, the logo consists of three regions with different PA conversion efficiency (i. glass/PDMS, ii. glass/PDMS/Cr/PDMS, iii. glass/PDMS/Cr/PDMS/Al), as shown in Fig. 2.6(e). Obviously, a PA image of the logo

shows the letter M with high PA conversion efficiency over the other regions, as shown in Fig. 2.6(d).

2.3.2 Facilitated heat transfer for efficient photoacoustic generation

For the sandwiched structures, the thinner metal layer can facilitate heat transfer to the surrounding materials, leading to more efficient PA conversion. To further study the dependence of PA conversion on metal absorber thickness, PA signals are measured by varying the absorber thickness for the two different metals (Cr and Ti). The measured PA amplitudes are shown in Fig. 2.7(a) and (b). For Cr samples, PA amplitude decreases with Cr layer thickness. However, above 70 nm of the Cr layer, PA amplitude begins to increase. This increase is likely due to increased light absorption (Fig. 2.7c). By normalizing PA amplitude to light absorption, we can clearly see the thickness dependence of PA conversion; the normalized PA amplitude decreases with the metal thickness (Fig. 2.7e). In other word, for the same light absorption, the thinner the Cr layer is, the higher PA amplitude is. Comparatively, for Ti samples, PA amplitude similarly decrease with the Ti layer thickness, as shown in Fig. 2.7 (b). Exceptionally, the thinnest Ti layer shows a low PA amplitude, because light absorption is too low (Fig. 2.7d). The PA amplitude normalized to light absorption shows the similar trend (Fig. 2.7f). The facilitated heat transfer indirectly observed in the measurement (in terms of PA amplitude) is now theoretically quantified. By assuming uniform temperature in the metal absorber and no interfacial resistance, the heat energy in each layer that produces PA signal is derived from the Green's function method (see the previous section for detailed

derivation). The heat energy (γ) normalized to the absorbed laser fluence (F) is represented by

$$\gamma_m + \gamma_s = 1 \quad \text{and} \quad \gamma_s = \frac{F_s}{F} = \frac{1}{\frac{\rho_m C_{p,m} d_m}{\rho_s C_{p,s} l_{th,s}} + 1}, \tag{2.21}$$

where the subscripts *m, s* denote the metal and surrounding material, respectively, d_m is the thickness of the metal layer, and $l_{th,s}$ is the heat penetration depth of the surrounding material $l_{th,s} = (1.269\alpha\tau)^{1/2}$, where α and τ are the thermal diffusivity and the laser pulse duration. Here, we made another important assumption that the heat transfer occurs within the laser pulse duration. This assumption is reasonable because the measured PA signals have the same pulse duration as the laser pulse. The heat energy in the surrounding material (γ_s) shows that the heat transfer is determined by a ratio of the two length scales ($d_m / l_{th,p}$). As shown in Fig. 2.8(a), the heat energy in the surrounding materials (γ_s) decreases with metal absorber thickness (d_m), whereas the heat energy in the metal absorber (γ_m) increases. Specifically, the thin metal absorber (10 nm) transfer almost 80% to the surroundings, while using only 20%. It is noteworthy that the calculated γ_s shows a similar trend as the measured PA amplitudes normalized to light absorption [see Fig. 2.7(e) and (f)].

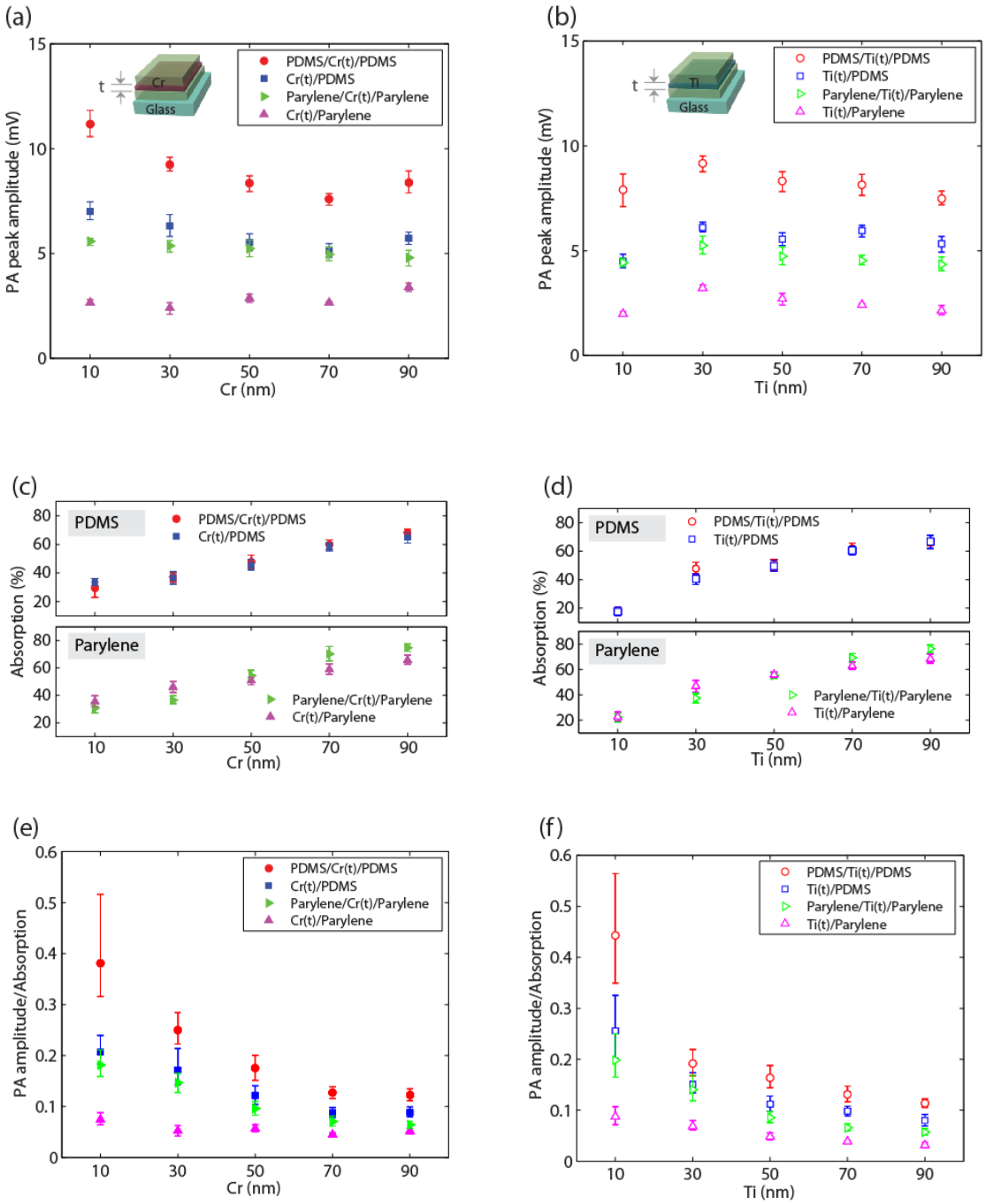

Fig. 2.7 Measured pressure amplitude for Cr (a) and Ti (b). Measured light absorption for Cr (c) and Ti (d). The pressure amplitude normalized to light absorption for Cr (e) and Ti (f).

This is because the PA signal produced in the surrounding materials (P_s) dominantly contributes to the output PA signal, i.e., $P = P_m + P_s \cong P_s$. Also, the P_s, normalized to the light absorption is proportional to the heat energy γ_s.

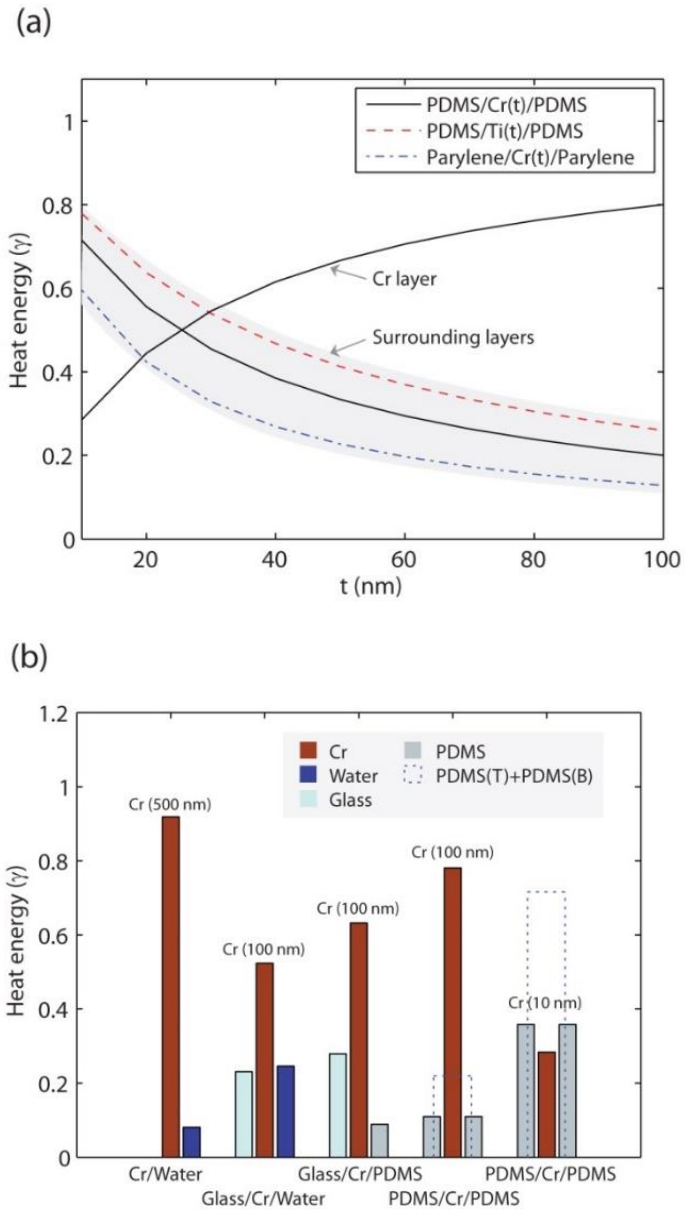

Fig. 2.8 (a) Calculated thermal energy at each layer for sandwiched structures. (b) Calculated thermal energy at each layer for different structures.

Figure 2.8(b) shows calculated heat energy for different structures. For thick Cr layer (500 nm) in contact with water, heat energy is mostly kept in the Cr layer (almost 90%). It is seen that the heat loss into the glass substrate is significantly high. By adding the top PDMS layer, heat energies in both the glass and metal layer increase, because of lower thermal diffusivity of PDMS layer. With the bottom PDMS layer, the heat energy in the Cr layer even further increases. However, the total heat energy in the surrounding PDMS layers accounts for only less than 30% (dashed bar). By reducing the thickness of the Cr layer down to 10 nm, the thermal energy is effectively transferred into the surrounding PDMS layers (almost 80%).

2.3.3 Optical cavity for light absorption

The thinner metal layer is effective in facilitating heat transfer into the surrounding, while reducing the light absorption. To compensate the low light absorption in the metal absorber, the photonic cavity (Fabry-Parot) is used, which consist of the Al layer and Cr layer. Here, the optical cavity length is important for optical resonance. As shown in Fig. 2.9(a), the reflective color changes with the cavity length, indicating a change in the resonance condition. The reflected light is red-shifted with the cavity length, as the absorption spectrum is shown in Fig. 2.9(b). Light absorption is significantly increased by implementing the cavity resonance. Specifically, the measured light absorption in the thin metal absorber is increased three times that in the structure without the reflector, as shown in Fig. 2.9(d). However, the PA amplitude is only increased by

about two times, as shown in Fig. 2.9(e). This might be due to temperature-dependent material properties. Indeed, there is a significant temperature difference between two structures with and without the reflector, which is estimated to be several hundreds of Celsius degree.

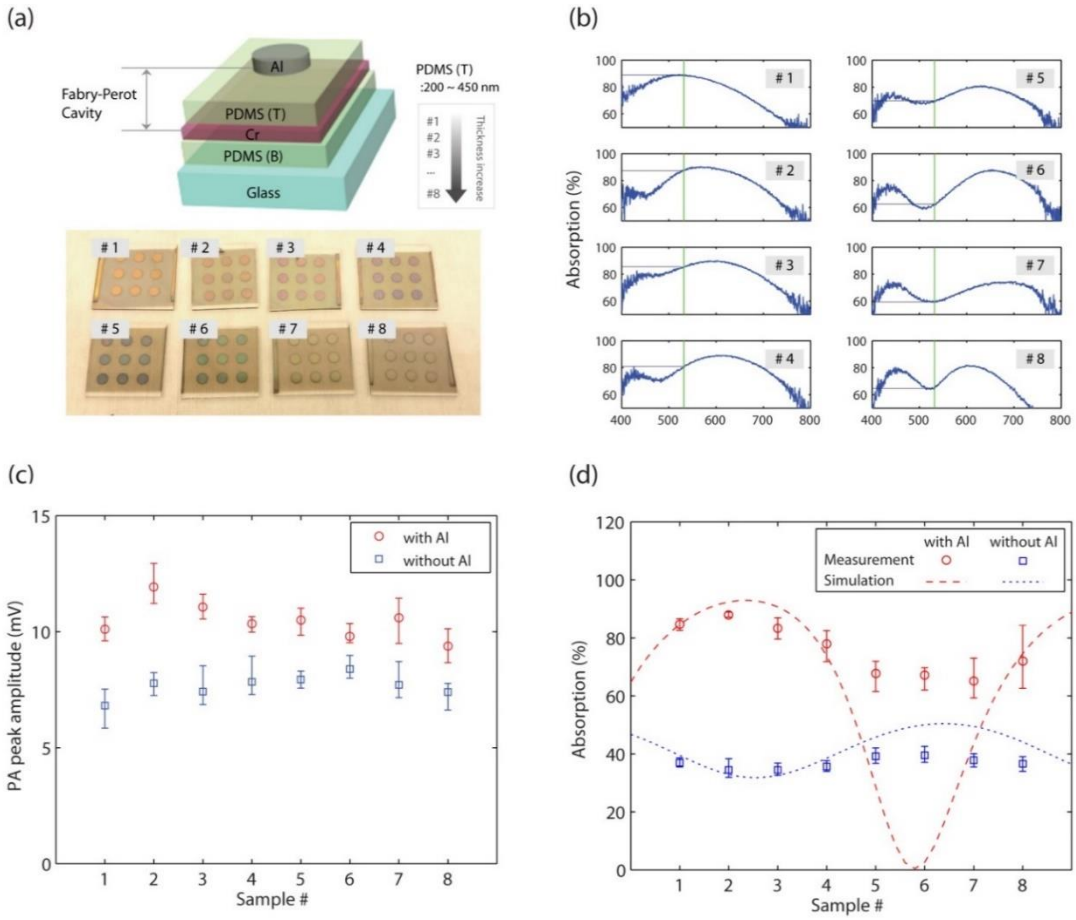

Fig. 2.9 Light absorption ehancement by using a photonic cavity (Fabry-Perot resonator). (a) Device structure with the cavity consisting of Cr and Al reflector. The cavity length is controlled by using different PDMS thickness. The fabricated samples with different cavity lengths show different colors. (b) Light absorption spectrum. With the cavity length increased, the resonance frequency is red-shifted. (c) Measured acoustic pressure amplitude for different cavity lengths (without Al reflector: square symbol, with Al reflector: circular symbol). (d) Measured light absorption (at an optical wavelength of 532 nm). The dashed line is obtained by simulation.

2.4 Conclusion

We have presented PA transmitters with a thin metal-based nanocomposite which is capable of efficiently transferring thermal energy to surrounding PDMS with high PA conversion efficiency and utilizing resonance cavity for enhanced light absorption. The PA signal is significantly enhanced as compared with thin bulk metal sample (an order of magnitude higher than), which even reach up to CNT based nanocomposites. Metal deposition and surrounding medium could be applicable to scalable process because it can be done using evaporation. Which open many possibility including PA enhancement for deep PA imaging, and new PA lens with large dimension (which cannot be achieved by spin coating process).

CHAPTER 3

Enhanced Out-coupling of Acoustic Transient by Control of Phase Cancellation

3.1 Introduction

Research on the photoacoustic (PA) effect, resulting from the absorption of electromagnetic radiation [25,26], has been motivated by various applications ranging from biomedical imaging [3,4], non-destructive test and evaluation (NDT and NDE) [2], to more recently, THz optoacoustic detection [27], and the study of the heat transport [28]. For those applications, knowing the amplitude dependence of the PA effect is essential for the interpretation of experimental data. Also, this knowledge could be used to increase photoacoustic amplitudes for applications, e.g., photoacoustic imaging and photoacoustic cavitation generation [8,15]. To obtain high-amplitude photoacoustic signals, focus has been typically placed on choosing materials with good light absorption and high thermal expansion coefficient, or simply increasing incident light intensity. However, given materials, their light-induced damages determine the upper-limit of the achievable photoacoustic signals.

Resonance phenomena due to the constructive interference of waves are often exploited to produce high-amplitude waves. However, the resonances are frequency

dependent such that it is difficult to implement for broadband photoacoustic pulses. Also, the short photoacoustic pulses make it even harder to meet the resonance requirement for the spatial and temporal overlap of the waves. Despite such difficulties, the interference of photoacoustic pulses cannot be ignored. In fact, the interference effect could be important for the actual photoacoustic generation, which was supported by work done by Diebold *et al*. [17,29,30]. To study photoacoustic monopole radiation in two and three dimensions, the authors considered two oppositely propagating photoacoustic waves simultaneously produced by pulsed optical heating. However, little attention has been paid to a significant change in photoacoustic amplitudes due to the time overlap of the two pulses, especially when one of the waves has opposite polarity. Furthermore, the individual contribution of the two propagating waves is rarely identified in the measured waveform. This is because the two waves are very close to each other such that the resulting photoacoustic wave is represented by the time-derivative of each wave. Besides two and three dimensions, photoacoustic waves in one dimensional absorbers for an air-backed boundary is also expressed by the time-derivative form [22,23], suggesting that the interaction of two photoacoustic pulses could play an important role.

In this work, we study the temporal overlap of the two propagating waves with a phase-lag that results in a change in photoacoustic amplitude. Such effect can occur when a planar light absorber is subject to the air-backed boundary condition, where the reflected wave experiences a π phase shift. If the reflected wave overlaps with the forward propagating pulse in space and time, significant amplitude cancellation is observed. To control the cancellation effect, we place an impedance matching layer on

the air side that is optically transparent and has the same acoustic impedance as that of the light absorber. By varying matching layer thickness, the cancellation can be effectively mitigated, thereby recovering strong photoacoustic amplitude. Furthermore, the cancellation effect for the planar absorber is extended to different dimensional absorbers, such as cylinders and spheres, providing further understanding of photoacoustic generation and an effective strategy for increasing photoacoustic amplitude in various applications.

3.2 Phase Cancellation in Planar Absorbers

3.2.1 Acoustic signal for different boundary conditions

Photoacoustic (PA) generation is studied for different acoustic boundary conditions. As the experimental setup is illustrated in Fig. 3.1(a), pulsed laser beam is illuminated on samples consisting of a thin metal layer and an adjacent polydimethylsiloxane (PDMS) elastomer layer. Here, the metal layer functions as a light absorbing medium that converts absorbed optical energy into thermal energy, while the PDMS layer serves as a substrate for metal deposition. As shown in Fig. 3.1(b), we apply three acoustic boundary conditions by using different backing mediums: Glass for hard boundary, air for soft boundary, and water for radiation boundary (i.e., no acoustic reflection occurs). PA signals are measured for the different boundary conditions, as shown in Fig. 3.1(c). Despite the same light absorbing layer, the generated PA signals vary a lot with the boundary conditions.

The hard boundary shows the highest signal amplitude, while the amplitude for the radiation boundary is only half the amplitude. Most notably, the soft boundary case produces significantly low amplitude, which is an order of magnitude lower than the others. Also, the waveform for the soft boundary is different from the others. In fact, the difference in the waveforms is well known and discussed elsewhere [23,31]. However, little attention is paid to the drastic change in PA amplitude.

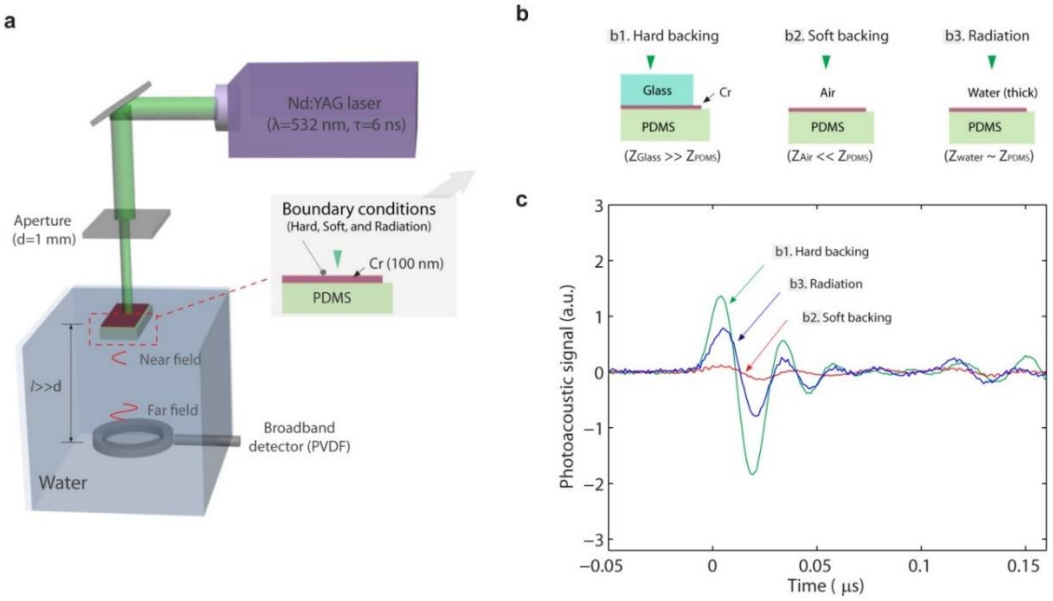

Fig. 3.1 (a) Experimental setup for photoacoustic generation and measurement. A 6-ns pulsed laser is illuminated through an aperture (1 mm in diameter) to samples consisting of a metal layer (Cr 100 nm) and adjacent PDMS layer. Photoacoustic signals are measured by a PVDF broadband detector in the far field (the distance between the samples and the detector is 10 mm; the laser spot size is 1 mm). (b) Samples for the different boundary conditions using different backing materials: Glass for hard boundary, air for soft boundary, water for radiation boundary. The boundary conditions differ based on acoustic impedance difference between backing materials and the PDMS layers because the thin metal layer is acoustically transparent (metal layer thickness is much smaller than acoustic wavelength); hard boundary ($Z_{glass} \gg Z_{PDMS}$), soft boundary ($Z_{air} \ll Z_{PDMS}$), and radiation boundary ($Z_{water} \sim Z_{PDMS}$). (c) The measured photoacoustic signals for the different boundary conditions.

3.2.2 Characterization of phase cancellation

The reduced amplitude for the soft boundary can be explained by the destructive interference of PA pulses that results in amplitude cancellation. Upon light absorption, the thin absorber layer launches both forward and backward waves simultaneously, as illustrated in Fig. 3.2(a). The backward wave experience a π phase shift when reflecting from the air-backed boundary. The π phase shift occurs for waves of any frequency, as the resulting reflected wave reverts its waveform in time, i.e., the amplitude flips its sign. The interaction between the reflected wave and the original forward wave is shown in the simulation results (Fig. 3.2c). If the temporal separation of the reflected wave and the original forward wave is large, the two propagates independently, as shown as the top two curves in Fig. 3.2(c). However, if the temporal separation is small enough such that the reflected wave is overlapped with the forward wave, significant amplitude cancellation can occur. An extreme case is shown as the blue curve in Fig. 3.2(c), where the two waves almost completely cancel each other, resulting in a drastically reduced wave amplitude. Interestingly, one can also make use of this effect to improve the wave amplitude. As shown in the green curve, when the propagating distance is chosen properly, the two pulses spatially overlap. And the portions of the pulses of same polarity overlap temporally, leading to enhanced wave amplitude (in this case, negative amplitude), and the overall pulse takes on an almost mono-polar waveform.

The cancellation and enhancement of PA pules is confirmed in an experiment where a carbon nanotube (CNT)-PDMS absorber, instead of the metal absorber, is used

for PA generation. To control the separation of the two PA pulses, we place an additional water layer on the air side and change its thickness (d_m), as shown in Fig. 3.2(b). Here, the water layer is chosen because of optical transparency and acoustic impedance matched with the polymer absorber, and will be referred to as matching layer. Figure 3.2(d) shows the measured PA signals. For a thick water layer (d_m = 5.28$c\tau$), we can observe two separated pulses, which are composed of a bipolar pulse followed by another bipolar pulse with opposite polarity. As the matching layer thickness decreases, the second pulse approaches the first one, Note that the two eventually merge into a single pulse with large negative amplitude. As expected, the two pulses with opposite polarity cancel out, when the water matching layer is completely evaporated (d_m = 0). Based on the interaction of the two PA pulses, it is easily understood that PA amplitude for the radiation boundary is only half that for the hard boundary; the backward wave does not interact with the forward wave.

For the soft-boundary condition, the matching layer allows the "out-coupling" of the photoacoustic waves, which otherwise cancel out. This finding suggests that we can define the out-coupling efficiency (η) represented by an amplitude ratio as $\eta = P_0/P_{R,0}$, where P_0 is the peak negative amplitude and $P_{R,0}$ is the peak amplitude for the radiation boundary. The out-coupling efficiency (η) is plotted as a function of matching layer thickness, as shown in Fig. 3.2(e). The symbols indicate the values obtained by the FEM calculation, while the dashed line represents those calculated by the one-dimensional (1D) analytical solution using the Green's function approach.

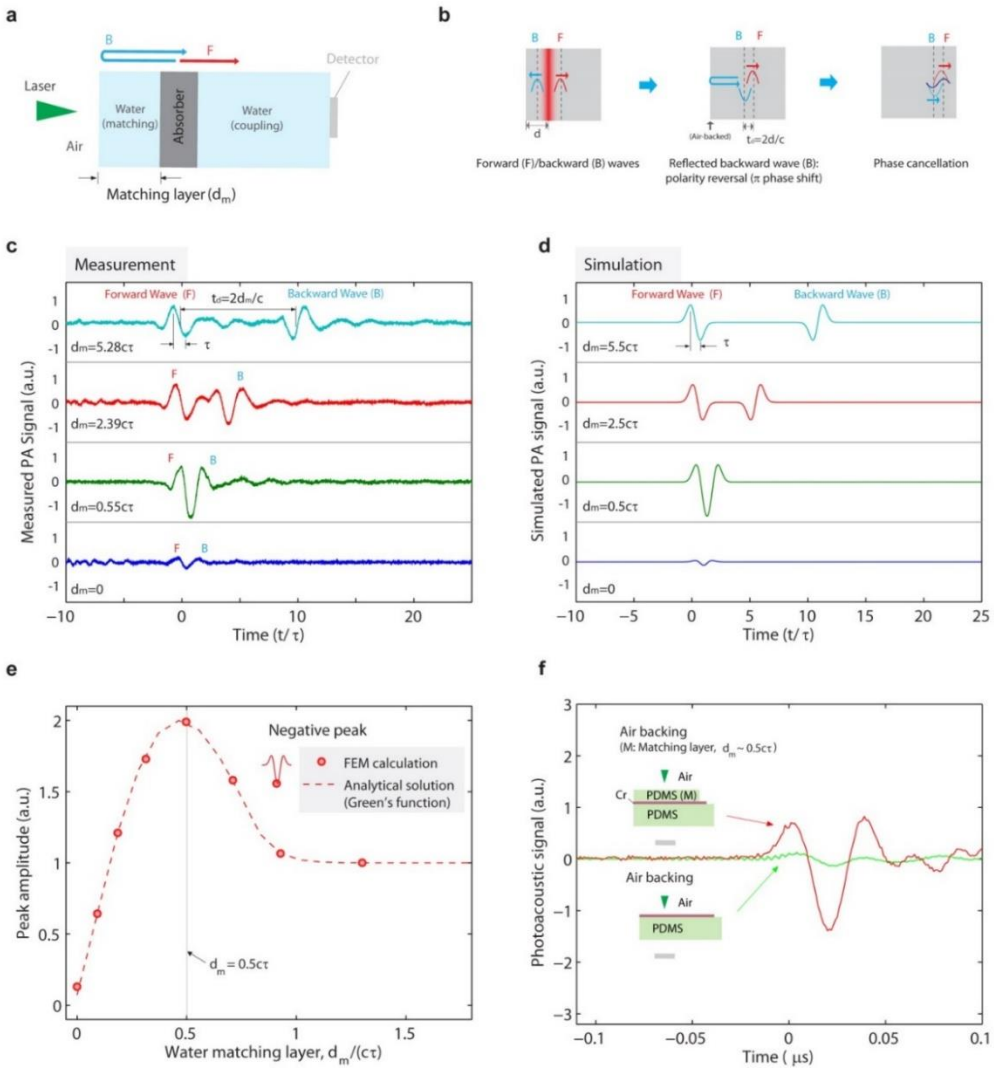

Fig. 3.2 (a) Photoacoustic generation for varying water layer in the air side (the water layer will be referred to as matching layer). The light absorber used here is a composite composed of PDMS and carbon nanotube fillers. Since the acoustic impedance of PDMS is similar to that of water, no significant reflection between the PDMS-based absorber and the water layer occurs. (b) Schematics of the phase cancellation. The two oppositely propagating waves (F, forward wave; B, backward wave) are simultaneously generated. The backward wave is reflected with a π phase shift (or polarity reversal) from the air-backed interface (B), cancelling the original forward-going wave. By varying the water matching layer thickness (d_m), photoacoustic signals are measured (c) and simulated (d). (e) Out-coupling efficiency (η) for different water matching layer thickness, defined by a ratio of the peak negative amplitude (P_0) to the peak negative amplitude for radiation boundary ($P_{R,0}$), i.e., $\eta = P_0/P_{R,0}$. The maximum out-coupling efficiency arises at $d_m = 0.5c\tau$. (f) Measured photoacoustic signals for the soft boundary with and without a PDMS matching layer. The photoacoustic amplitude for the sample with the matching layer is an order of magnitude larger than that for without the matching layer.

The two calculations show an excellent agreement. Maximum out-coupling occurs at a matching layer thickness of $d_m = 0.5c\tau$ (τ is the laser pulse duration). For that thickness, the reflected pulse has the right time delay such that the negative peaks of the two pulses are exactly overlapped, as also can be seen in Fig. 3.2(c) and (d). Note that the resulting negative amplitude becomes comparable to that for the hard boundary. Moreover, the matching layer approach can be applied to the metal-PDMS structures in Fig. 1. By adding a PDMS layer (~ 15 μm) on the air side as matching layer, the signal amplitude is greatly increased, as shown in Fig. 3.2(f). It is also interesting to note that the waveform remains the same.

3.2.3 Analysis of phase chancellation: Green's function method

Photoacoustic signals are calculated by solving the heat conduction equation and pressure wave equation. The heat conduction equation yields the time-dependent temperature field $T(\vec{r},t)$ induced by pulsed-laser heating , which is represented by

$$\rho C_P \frac{\partial T}{\partial t} = \nabla(k\nabla T) + H(\vec{r},t), \tag{3.1}$$

where ρ is the density, C_p is the specific heat capacity at constant pressure, k is the thermal conductivity, and $H(\vec{r},t)$ is the volumetric non-radiative heat generation due to light absorption (W/m^3). The above equation is based on the assumption that adiabatic heating induced by compressive pressure are negligible when C_p is almost identical to the specific heat capacity at constant volume C_V [14]. With the calculated temperature from

the equation (3.1), the pressure field $p(\vec{r},t)$ in a liquid can be determined by solving a wave equation for pressure represented by

$$\left[\nabla^2 - \frac{1}{c^2}\frac{\partial^2}{\partial t^2}\right] p(\vec{r},t) = Q_{aco} = -\rho\beta\frac{\partial^2 T}{\partial t^2}, \tag{3.2}$$

where c is sound speed, Q_{aco} is an acoustic source term modeled by thermoelastic mechanism, and β is the thermal expansion coefficient.

By using the equation (3.1) for negligible heat conduction (i.e., $\nabla(k\nabla T) = 0$), which corresponds to $\rho C_p \frac{\partial T}{\partial t} = H(\vec{r},t)$, the equation (3.2) can be alternatively represented by [4,17]

$$\left[\nabla^2 - \frac{1}{c^2}\frac{\partial^2}{\partial t^2}\right] p(\vec{r},t) = -\frac{\beta}{C_P}\frac{\partial}{\partial t} H(\vec{r},t), \tag{3.1}$$

This is valid when the heat does not diffuse over the spatial extent of the acoustic pulse defined by $l_{aco} = c\tau_{aco}$, where τ_{aco} is the acoustic pulse duration. In other word, heat diffusion length during the acoustic pulse duration ($l_{th} = \sqrt{\alpha\tau}$, thermal diffusivity $\alpha = k/\rho C_P$) is much smaller than l_{aco}. The one-dimensional form of the equation (3.1) is typically used and can be expressed by

$$\left[\frac{\partial^2}{\partial z^2} - \frac{1}{c^2}\frac{\partial^2}{\partial t^2}\right] p(z,t) = -\frac{\beta}{C_P}\frac{\partial}{\partial t} H(z,t), \tag{3.3}$$

where z is the spatial variable. The one dimensional equation in a liquid also holds for an isotropic solid when the sound speed c is substituted by the longitudinal sound speed

c_L and the thermal expansion coefficient β is replaced by the effective thermal expansion coefficient $\beta_{effective} = \beta\left(1-4c_T^2/3c_L^2\right)$, where c_T is the transverse sound speed [23].

Applying the Green's function approach to the one-dimensional wave equation (4) yields the general solution for pressure, which is represented by

$$p(z,t) = \frac{\beta c}{2C_P}\int_{-\infty}^{\infty} dz' g(z,t \mid z',t) H\left(z', t - \frac{z-z'}{c}\right), \tag{3.4}$$

where $g(z,t \mid z',t)$ is the Green's function for an infinite medium. The appropriate Green's function for $z > z'$ is $g(z,t \mid z',t) = 2\pi c u\left((t-t')-(z-z')/c\right)$, where u is the Heaviside function. Then, the excited photoacoustic pulses has the form of

$$p(z,t) = \frac{\beta c}{2C_P}\int dz' H(z', t - \frac{z-z'}{c}). \tag{3.5}$$

The one-dimensional Green's function above can be modified to take into account the reflected pulse from the interface, which is produced simultaneously with the original forward-propagating pulse. The modified Green's function can be represented by the sum of two one-dimensional Green's functions $g(z,t \mid z',t) + R \cdot g(z,t \mid -z',t)$, where R is the acoustic reflectance (-1 for a sound soft boundary and +1 for sound hard boundary) [17]. Thus, the photoacoustic signals for different boundaries can be represented by [17,30]

$$p(z,t) = \frac{\beta c}{2C_P}\int_{-\infty}^{\infty} dz'\left[H\left(z', t - \frac{z-z'}{c}\right) + R \cdot H\left(z', t - \frac{z+2d_m+z'}{c}\right)\right], \tag{3.6}$$

where d_m is the thickness of the additional layer between the reflecting boundary and the origin (the reflecting boundary is located at $z = -d_m$). Here, the heating function $H(z',t)$

can be expressed as product of temporal and spatial heating functions, $f(t)$ and $g(z')$ by $H(t,z') = I_0 f(t) g(z')$ (W/m^3), where I_0 is the peak intensity (W/m^2), $f(t)$ is related to energy fluence F through $F = \int I_0 f(t) dt$ (J/m^2), and $g(z')$ (1/m) is normalized for satisfying $\int g(z') dz' = 1$. With the retarded time ($\tau = t - z/c$), the first pulse of the equation (6) can be specified in mathematics by the cross-correlation integral $\int f(c\tau + z') g(z') dz'$, while the second reflected pulse can be by the convolution integral $\int f(c\tau - z') g(z') dz'$.

3.3 Phase Cancellation in Two- and Three- dimensional Absorbers

The cancellation effect observed in the 1D absorbers with the air-backed interface can similarly occur in spherical and cylindrical objects, where symmetric optical heating yields two oppositely propagating waves (inwardly and outwardly) [30]. As illustrated in Fig. 3.3, the inwardly propagating wave can experience phase shifts depending on dimension, known as Gouy phase shift (π phase shift for a spherical wave, $\pi/2$ phase shift for a cylindrical wave) [32]. The waves with the phase shifts can interfere with the original outgoing waves. If dispersion can be neglected, a pulse comprising of waves of a range of frequencies will follow similar phase shift, and interact with the original outgoing pulse when they are temporally overlapped.

To control the interaction of the two waves, transparent matching cores (analogous to the matching layer for a 1D absorber) can be used for sphere (3D) and cylinder (2D) with

light-absorbing shells. The simulated photoacoustic signals for the sphere with the core r_c and the shell d_{op} are shown in Fig. 3.4(a) for the long pulse regime ($\tau >> d_{op}/c$). The photoacoustic signals are normalized to the signal amplitude for $r_c = d_{op}$. For a uniform volumetric heating energy $H=H_0(t)$, the photoacoustic amplitudes significantly increase with the core radius r_c. Also, the photoacoustic pulses have the bipolar waveforms (the time-derivative of the temporal optical intensity profile) [17]. Interestingly, the acoustic signal for $r_c=25d_{abs}$ is two orders of magnitude higher than that for $r_c/t_{abs}=1$.

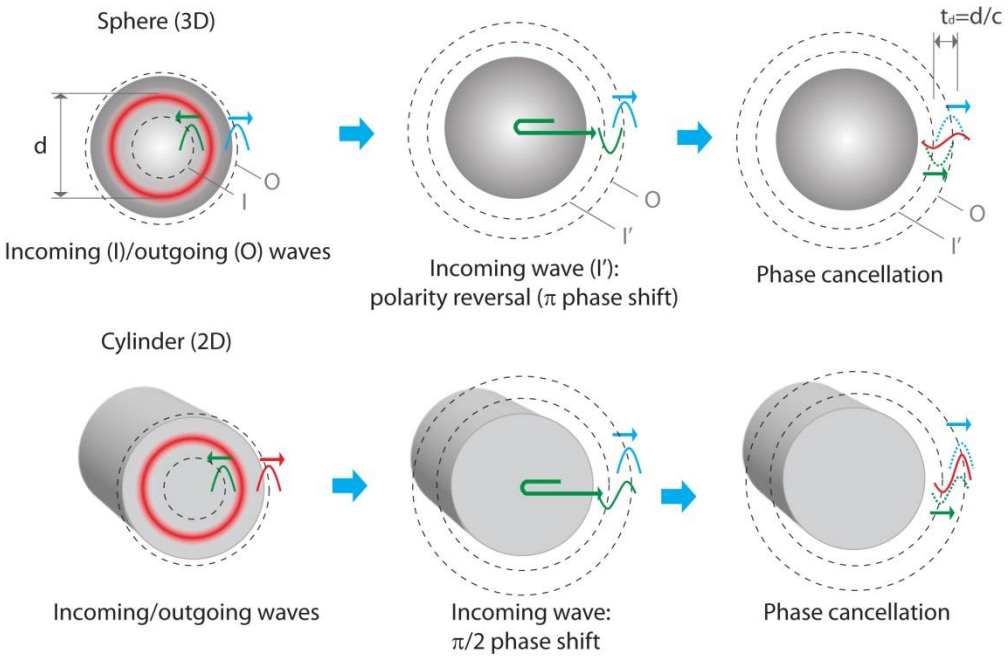

Fig. 3.3 Illustration of the phase cancellation in cylindrical and spherical objects. Two oppositely propagating waves (I: inward and O: outward) are produced by pulsed symmetric heating. As going through the center, the inward wave experiences a phase, then immediately following the original outward wave. For the spherical wave, a π phase shift (or polarity reversal) occurs, while for the cylindrical wave, a π/2 phase shift (bipolar waveform) occurs. The wave with the phase shift can interfere with the other wave, which depends on the delay time between the two waves.

However, such difference cannot be solely explained by the cancellation effect, but rather by the combined effect of the PA cancellation and the 1/*r* amplitude decay of spherical acoustic waves.

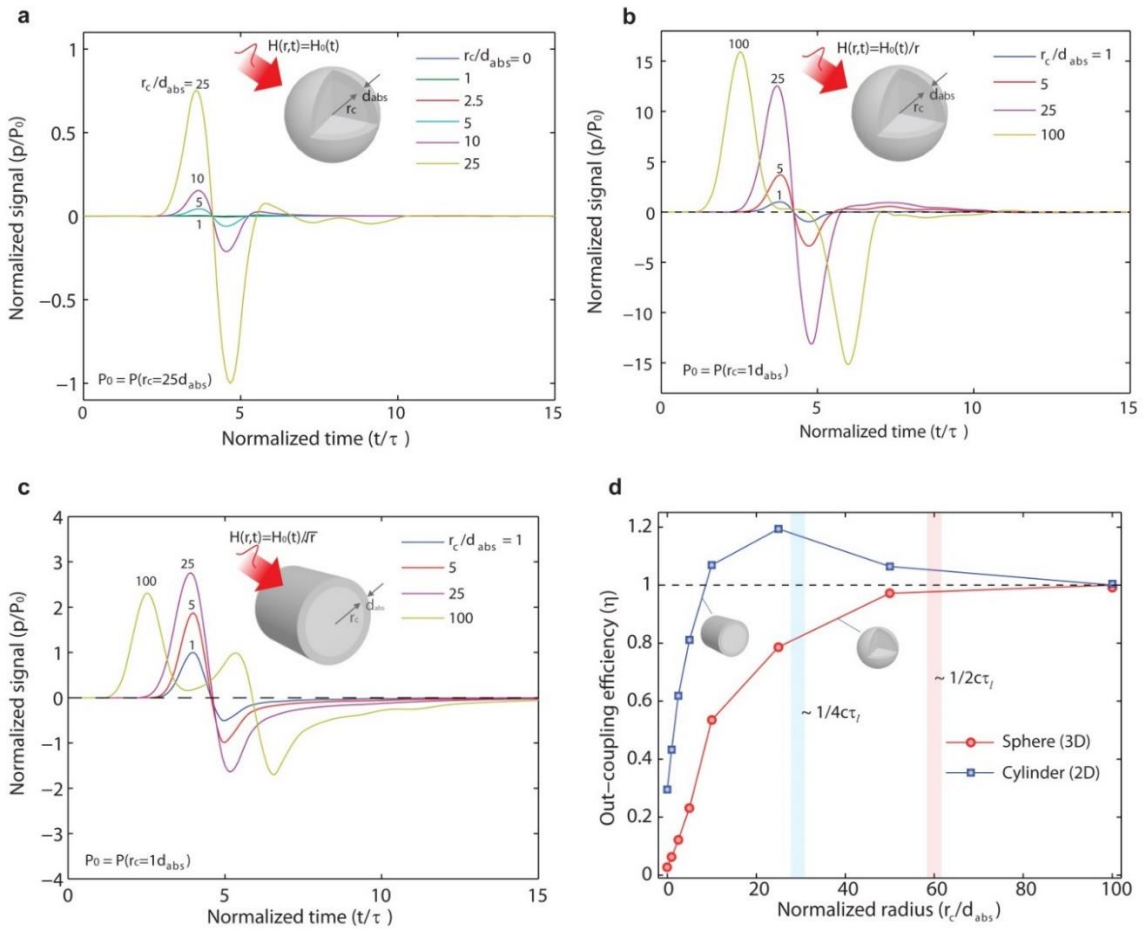

Fig. 3.4 (a) Simulated photoacoustic signals of a sphere with a transparent core (r_c) and an absorbing shell (d_{abs}). The transparent core has the same acoustic impedance as that of the shell, thus serving as matching medium analogous to the matching layer for the planar absorber. By using uniform heating $H_0(t)$, the signals for different matching core radius are obtained at a distance of r_{obs} from the center. Also, the signals are normalized to the pressure amplitude ($P_0 = P(r_c=1d_{abs})$). (b) Photoacoustic signals for non-uniform heating ($H_0(t)/r$). (c) Simulated photoacoustic signals for the cylinder ($H_0(t)/r^{0.5}$). (d) The out-coupling efficiency (η) for sphere and cylinder with the constant shell thickness (d_{abs}) as a function of the core radius (r_c).

With larger radius r_c, the photoacoustic source is much closer to the observation location r_{obs}, thus reducing the acoustic decay. To evaluate only the contribution of the cancellation effect, the photoacoustic signals are re-calculated by using the heating energy H(t) scaled with $1/r$, i.e., $H(r,t)= H_0(t)/r$. As shown in Fig. 3.4(b), the scaled photoacoustic amplitudes increase with the core radius. Also, the inward wave is completely separated from the original outward wave at r_c=100 d_{op}. The time delay between the two pulses is identified to correspond to an acoustic transit time across the core diameter ($2r_c/c$). Moreover, the interaction of the two pulses observed here for different time-lag are similar to that for a 1D absorber in the near field.

Figure 3.4(c) shows the simulated acoustic signals for the cylinder with the transparent core and the light-absorbing shell. Here, the heating energy is scaled by $1/ r^{0.5}$ for the acoustic decay of cylindrical waves. Similar to those for the sphere, the photoacoustic signals show bipolar waveforms, but with higher positive amplitude than negative one (which follows the one-half time-derivative of the optical radiation intensity) [17]. It is clear that the amplitude increases with the core radius r_c. And the two waves are completely separated at a core radius of r_c=100 d_{op}, which gives a sufficient delay to the inwardly-propagating wave. The delayed wave has a bipolar waveform due to a $\pi/2$ Gouy phase shift, while the original out-going wave shows a mono-polar waveform. It is noteworthy that the amplitude increase by the matching core is much smaller than that of the sphere. This is because the delayed wave cannot completely cancel the original out-going wave in the 2D case. Thus, the transparent matching core is less effective in the cylinder case than in the sphere case. For further comparison with the sphere, the out-

coupling efficiency is plotted in Fig. 3.4(d). Unlike the sphere case with the monotonic increase, the cylinder case exhibits an efficiency overshoot exceeding one at a core radius of $r_c = 30 d_{abs}$. At that radius (its corresponding time delay is $1/4c\tau$), the two positive peaks of the two waves are overlapped, leading to the highest amplitude.

3.4 Conclusion

We have systematically investigated the cancellation effect that is responsible for significantly low photoacoustic (PA) pressure amplitude for the soft boundary. Here, the phase cancellation arises because pulsed optical heating yields two oppositely propagating waves, one of which is reflected with polarity reversal from the soft boundary, cancelling the other. In typical measurement, the two waves with opposite polarity are so close to each other that each wave has hardly been identified. However, by using the transparent matching layer that gives a delay time to the reflected wave, the two pulses can be separated, minimizing the cancellation effect and thus increasing photoacoustic amplitudes. Eventually, we can observe the two pulses completely separated.

The phase cancellation effect is influenced by the optical penetration depth. For small optical penetration depth, the cancellation effect is significant such that the matching layer is very effective in recovering the PA amplitude. However, for large optical penetration depth, the cancellation effect is less significant. This is because the optical penetration depth provides with the intrinsic time delay between the two waves.

On the other hand, although an increase in the optical penetration depth can increase their time delay, the two waves cannot be completely separated, because large optical penetration depth also broadens the acoustic pulse duration.

The cancellation effect observed in the planar absorber can be similarly seen in the other dimensions including 2D and 3D. Unlike the 1D and 3D cases, the cylinder case shows the minimized phase cancellation, since the delayed wave has a bipolar waveform (a $\pi/2$ phase shift) that is different from a monopolar waveform of the original outward wave. Moreover, the phase overlap between the bipolar and monopolar waveforms gives an idea of why the resulting wave is the bipolar waveform, but with the positive amplitude twice larger than the negative one. This understanding provides useful guidelines in developing photoacoustic contrast agents.

The cancellation effect for a 1D absorber can be prevented by using the hard boundary, which is, however, typically not practical. Also, it is challenging to choose the right matching medium that is optically transparent and has the same acoustic impedance as that of the light absorber. For example, an important application of laser ultrasonics is in non-destructive test and evaluation (NDT & NDE). It is know that direct laser incident onto the metal surface produces only weak PA longitudinal wave into the metal. This can be interpreted as the cancellation of the reflected wave due to zero delay. However, the cancellation effect can be mitigated by using a transparent matching layer whose acoustic impedance is much smaller than that of the light absorber. For example, a thick water matching layer is added on to the bulk metal. In such way, the reflection from the water/metal interface is low as compared to the reflection from the air/metal interface,

leading to reduced cancellation.

CHAPTER 4

Focusing of Laser-induced Acoustic Transient: Observation of Acoustic "Gouy" Phase Shift

4.1 Introduction

A spherical converging wave propagating through a focus experiences an additional π phase shift (*i.e.*, the Gouy phase shift) with respect to a reference plane wave or a carrier envelope. The phase anomaly has been subject of study because it arises from a general wave nature that is governed by wave equation. Thus, experimental observations have been reported in optics [33-37]. In particular, the polarity change of single-cycle terahertz pulses has been directly observed [33-35]; in addition, the Gouy effect on focused few-cycle laser pulse was demonstrated owing to stabilization of the carrier-envelope phase [36]. On the other hand, in acoustics, experimental demonstrations for the phase shift have been reported only for some special cases, e.g., a plane acoustic source[38] and a two-dimensional (2D) focusing surface wave[39], where a $\pi/2$ phase shift occurs, although the phase shift of three-dimensional (3D) focusing acoustic wave has not been reported.

Despite such valuable experimental demonstrations, the physical origin of the phase anomaly continues to be a matter of debate, producing much work positing

different physical origins. Specifically, the phase anomaly has been related to quantum mechanics and the uncertainty principle [40,41] and to geometrical properties of Gaussian beams [42-44]. Some earlier studies tried to provide the intuitive explanation of Gouy phase shift [44] (more references). Still, the axial phase shift requires good physical explanation for better understanding.

Meanwhile, many works have reported that the waveform of focusing acoustic waves (generated by the conventional piezo-transducer) was observed to be changed during propagation [45,46]. However, the observed results have not been related to the Gouy phase shift. This is presumably because of the edge wave that is radiated from the edge of the source surface. Unlike the Gaussian light beam whose intensity decay exponentially in the lateral direction, the uniform acoustic beam typically yielded the edge wave. Accordingly, the presence of the edge wave may impede recognize the physical similarity between focusing acoustic and optical waves and thus the associated phase shift.

In this work, we analyze the edge wave to understand the phase shift of a focusing wave. Based on the analysis, we provide an intuitive explanation of the Gouy phase shift by using the Huygens' the concept of secondary waves and the Rayleigh integral. The physical origin of the phase shift is attributed to facts that individual secondary wave contributes with temporal derivative of a source waveform to the consequent waves, and that secondary waves from different point sources change their axial sequence after a focus. Accordingly, the superposition of the secondary wave

determines the polarity of the resulting waves and hence the phase shift, depending on the axial sequence of the resulting waves. We also demonstrate direct observation of the polarity change of a single nanosecond acoustic pulse and confirm with simulation results.

4.2 Direct Observation of Acoustic Phase Anomaly

4.2.1 Characterization of acoustic phase shift

We performed an experiment of a focused acoustic wave that was generated by pulsed optical excitation of the carbon nanotube (CNT)-polymer composite coated on the transparent concave substrate (Namely, CNT lens) [1]. The nano-composite film (< 5 μm) serves as an excellent broadband light absorber (CNT) and as an high thermal expansion medium (PDMS) for efficient optoacoustic conversion [6]. The temporal profile of the optically excited acoustic pulse is determined by two competing timescales (the acoustic transit time t_{ac} across the absorbed length of the composite versus laser pulse duration t_p). Because our experimental condition falls into a long pulse regime ($t_{ac} < t_p$), the generated acoustic wave approximates the temporal profile of the exciting laser [17]. The acoustic wave leaving the CNT lens is converged at the focus that is the center of radius of curvature of the concave lens surface (f = 9.2 mm). The converging acoustic beam is diffracted by acoustic diffraction, consequently experiencing the phase shift.

By using laser flash shadowgraphy [47], we first visualized acoustic wavefronts propagating at a speed of 1500 m/s (sound speed of water). The imaging technique is

capable of capturing a fast-moving object with nanosecond time resolution (in principle, time resolution is determined by pulse width of laser flash, ~ 1 ns FWHM). As induced by refractive index contrast (or density change) due to the acoustic wave, shadow images under laser flash are recorded by a normal CCD camera (exposure time: ~ ms). Figure 4.1(a) shows acoustic wavefronts: simulation results (top) and experimental results (bottom).

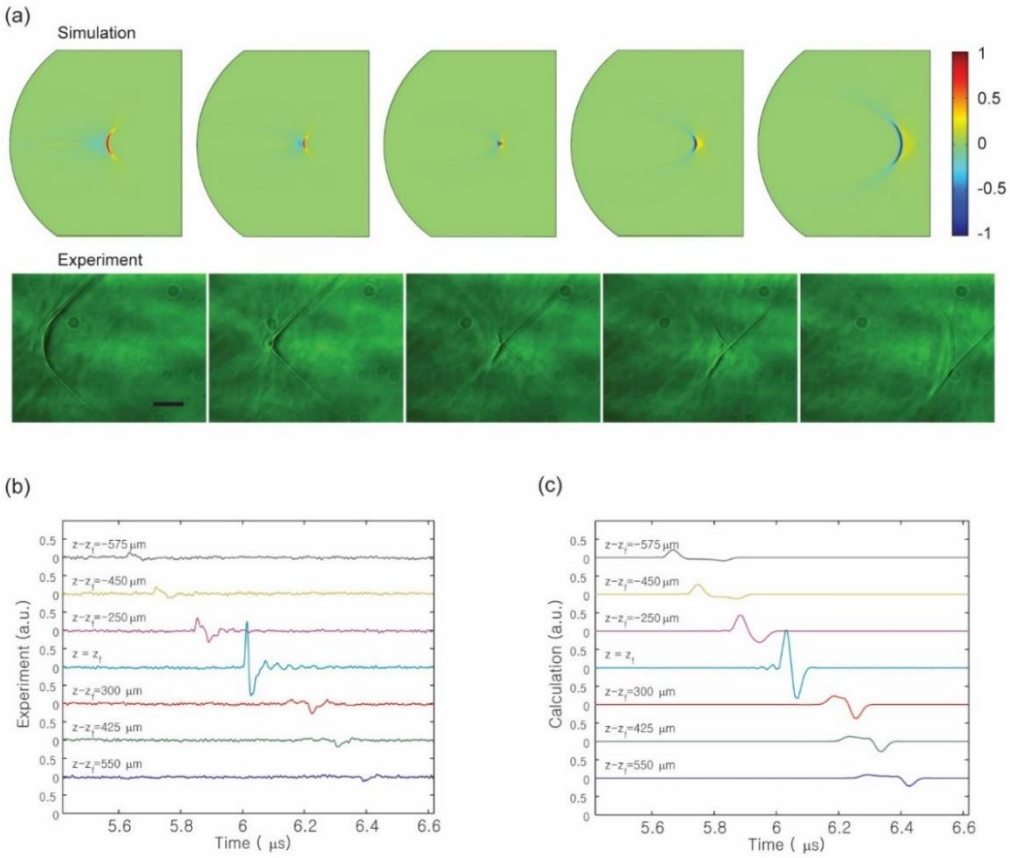

Fig. 4.1 (a) The acoustic wave propagation for the normalized simulation result (top: t = t_f-1μs, t_f-0.5μs, t_f, t_f+0.5μs, t_f+1μs, t_f is the time when the wave is arrived at the focus) and the shadowgraph images (bottom: t = t_f-140ns, t_f-70ns, t_f, t_f+70ns, t_f+140ns). The scale bar indicates 100 μm. (b) Pressure transient (Experiment) with respect to different locations. (c) Pressure transient (simulation) with respect to different locations.

The CNT lens was illuminated by collimated uniform light beam, which determines lateral pressure intensity on the source surface. The visualized images show a good match with the simulated acoustic fields (axisymmetric simulation), each normalized to their maximum amplitudes. Moreover, the simulated wavefronts clearly show the sequence change (from the leading wave to the trailing wave) that is responsible for the polarity reversal (discussed above). Consequently, the geometrical wave changes its polarity from positive to negative, as the color change (from red to blue) is shown in the simulation result (Fig. 4.1(a)). Meanwhile, in the visualized images, negative phases identified in the simulation are less discernible; after the focus, the geometrical wavefront (from positive to negative) is less prominent than before the focus, while the edge wave (from negative to positive) becomes distinct (it is hardly seen before the focus). This can be an indirect signature of polarity change.

Next, the focused acoustic signals were directly measured by using a fiber-optic hydrophone. The detection zone of the hydrophone (a core diameter of 6 μm) is much smaller than the acoustic spot size (FWHM 75 μm), thus it can be regarded as a point detector. To see the polarity change near the focus, the detector was scanned in the z direction ($z - z_f$ = -575~550 μm). The measured acoustic signals are shown in Fig. 4.1(b). We clearly observed the polarity change (*i.e.* phase shift): before the focus ($z - z_f$ = -575 μm), the signal is positive; after the focus ($z - z_f$ = 550 μm), the signal becomes negative. Again, such polarity reversal is a direct consequence of the Gouy phase shift.

The measured signal at the focus becomes a bipolar waveform (i.e., time-

derivative of the input source), which is well known as phenomenon induced by a wave diffraction. By employing the concept of Huygens' secondary wave, such phenomenon can be easily understood. Because all the secondary waves emanated from the concave surface arrive simultaneously at the focus, they are all in phase (constructive interference). Therefore, the waveform at the focus is ideally identical to that of the individual secondary wave. As indicated above by the Rayleigh integral, the secondary wave has time-derivative of the input pressure, so does the resultant wave at the focus.

The acoustic signals (Fig. 4.1(b)) evolving through the focus were qualitatively consistent with the simulated values (Fig. 4.1(c)). However, unlike the measured signals (not clearly seen in the measured signals), the simulated results (Fig. 4.1(c)) clearly show the 'wake' region ahead of the wavefront after the focus and behind the wavefront before the focus, as it is also shown in Fig. 4.1(a) (the colored region between the edge and geometrical wave). The wake arises because of non-uniform lateral pressure intensity on the source surface. Although we applied the collimated light beam with uniform intensity, on the source surface the generated photoacoustic signal determined by the absorbed light intensity varies with position because of angle-dependence of the absorbed light intensity ($I_{abs}(\theta) = I_0 \cos(\theta)$, where $\theta = \sin^{-1}(r/d)$). For the CNT concave lens with D = 15mm and f = 9.2 mm, the source pressure decays gradually with r, and thereby decrease by 40% at the edge. The non-uniform secondary waves are not completely cancelled out, instead producing the plateau (wake region) between the geometrical and edge waves. Furthermore, the wake makes the edge wavefront less discernable. This is in sharp contrast to the uniform pressure source, where the wake region does not appear because

of completely destructive interference of the secondary waves; and the edge wave is very distinct in the absence of the wake.

4.2.2 Effect of lateral acoustic intensity on phase shift

The phase anomaly is originated from the axial sequence change of secondary waves, which is consequently recognized as the order change between the geometrical wave and the edge wave. In this regard, the edge wave emergence is a key clue to the reasoning behind the phase shift. However, the presence of the edge wave may also prevent from relating the polarity reversal to the Gouy phase shift. This is because in the measurement a leading positive wave (geometrical wave before focus, edge wave after focus) is firstly detected before and after focus; it is difficult to tell whether phase shift occurs, although each wave experiences the polarity change.

The edge wave, radiating from the edge of the source surface, is influenced by the lateral distribution of source intensity. With lowering the edge pressure, the edge wavefront is less pronounced and even completely disappears for the Gaussian source. However, the same explanation for the phase shift can be applied to the Gaussian source whose magnitude decays exponentially with distance from the z-axis. To illustrate this, we show the secondary waves along the z-axis for two different lateral intensities. For the uniform source, the secondary waves from all the source points remain same, and therefore resulting in both the edge and geometrical waves. On the other hand, for the Gaussian source the magnitude decays exponentially, thus the edge wave disappears. Regardless of

the presence of the edge wave, the geometrical wave, initially leading the secondary waves, becomes trailing waves, thus experiencing a π phase shift. The measured axial acoustic pressures are plotted in the Fig. 4.2 as a function of time (*t*) and position (*z*) in the focal region. The acoustic transient at each position is normalized to its maximum amplitude. The two straight lines corresponding to the edge and geometrical waves are observed clearly, interacting at the focus.

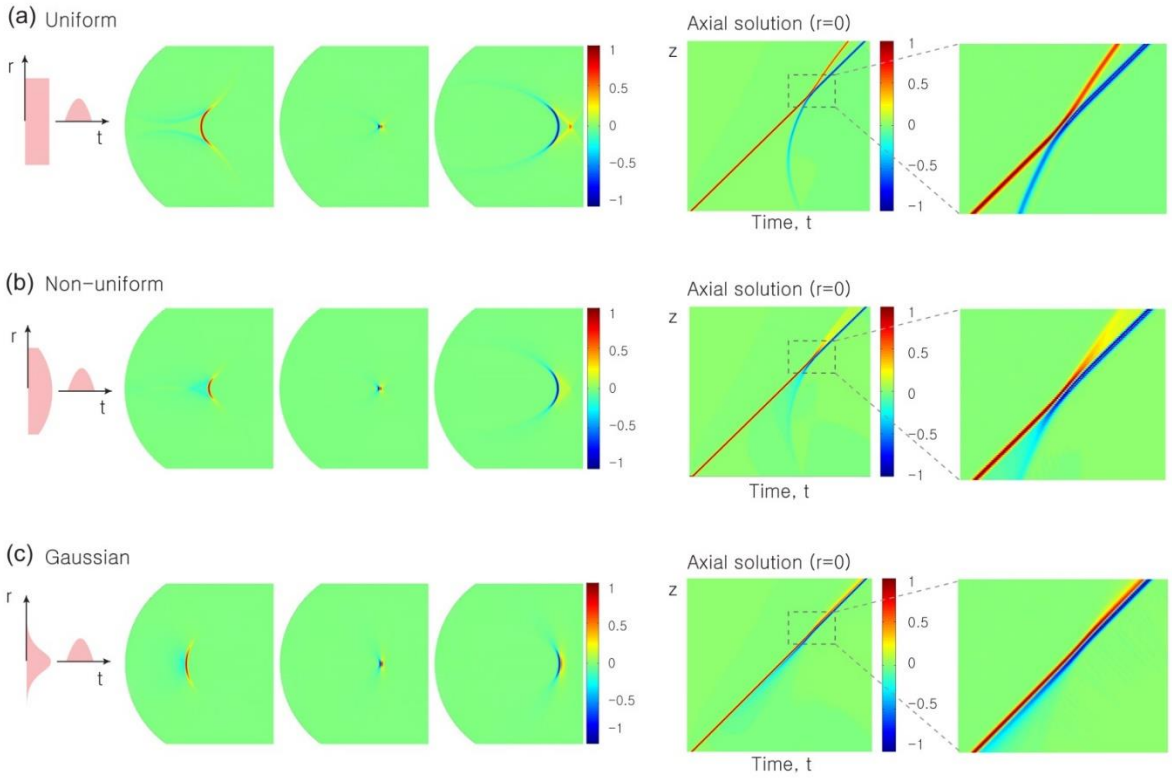

Fig. 4.2 Simulation result for different lateral intensity (uniform (a), non-uniform (b), and Gaussian (c). Also, the corresponding axial solutions are plotted. The focal regions are magnified.

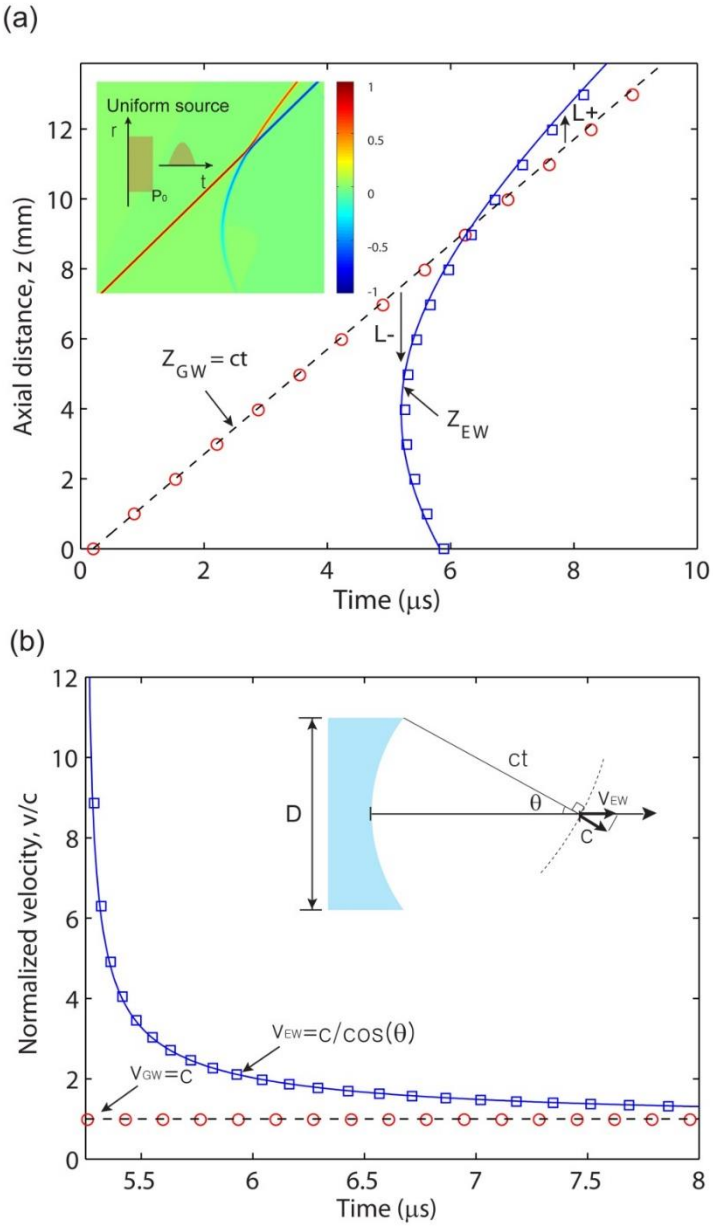

Fig. 4.3 (a) Location of wave-front. The straight line indicates the geometrical wave, and the curved line for the edge wave. (b) Axial acoustic speed. The symbol represents the slope of the lines of (a). The straight line is the constant acoustic speed (c) for the geometrical wave, while the curved line corresponds to the edge wave, which is determined ($v = c/\cos\theta$).

As the line for the geometrical wave changes its color into blue after the focus, it becomes negative values. Such color change indicates that a π phase shift occurs because the polarity of the initial temporal profile was positive (*i.e.*, red). It is also interesting to note that the edge wave changes its color from blue to yellowish after the focus, and thereby experiences the same phase shift. The cross lines indicate the sequence change between the waves; the edge wave become ahead of the geometrical wave after going through the focus.

The simulated axial pressure clearly shows a wide range of time and position, as shown in Fig. 4.3(a) for the non-uniform source (the same input as the experiment). The geometrical wave remains linear throughout all time, while the edge wave is a curved line. The region between two lines has non-zero value ('wake' discussed above). For the uniform source, in contrast, the region between the lines has zero value, showing the distinct lines as shown in Fig. 4.3(a). These clear lines suggest that the waves inside the region interfere destructively. The order change between the edge wave and geometrical wave, which is explained by geometrical properties of focusing wave, is also understood as a difference in axial phase velocity between the two waves. The velocity of the edge wave is higher than that of the geometrical wave.

The axial phase velocity is plotted in the Fig. 4.3(b). The axial velocities (symbol) are derived from the slop of the crossing lines (Fig. 4.3(a)). The geometrical wave propagates at a constant speed of sound (c), whereas the velocity of the edge wave exceeds the sound speed ($v > c$), decreasing rapidly, and approaching to c. The solid line

for the edge wave geometrically determined ($v = c/\cos\theta$, where θ is the angle between the normal to the edge wave-front and the z-axis) show good fit with the values from the slop. The edge wave with higher velocity overtakes the geometrical wave, resulting in the order change.

4.2.3 Intuitive explanation of phase shift

Huygens' Principle indicates that a propagating wave-front results from the superposition of secondary spherical waves radiating from every point located at the preceding wave. Accordingly, the interference of the secondary waves can capture the characteristic of the resulting waves. Especially, such concept enables better understanding of geometrical properties of spherical converging wave, and even its phase shift. Based on Huygens' concept, the geometrical change of converging wave before and after focus is first examined. Figure 4.4(a) illustrates the secondary waves with radius R_s that radiate from the representative point sources on the axisymmetric concave surface with radius of curvature f and transverse diameter D. In specific, the secondary waves superimposed construct two propagating wavefronts: the geometrical waves (GW; resembling the shape of the source surface) and edge waves (EW; emanated from the edge of the source surface). Moreover, the secondary Huygens wavelets explain why wavefront experiences geometrical change as it propagates through the focus. Specifically, when the radii of the secondary waves are smaller than the focal length (f), the edge wave is located behind

the geometrical wave; but for $R_s > f$, the geometrical wave changes its sign of curvature and follows the edge wave.

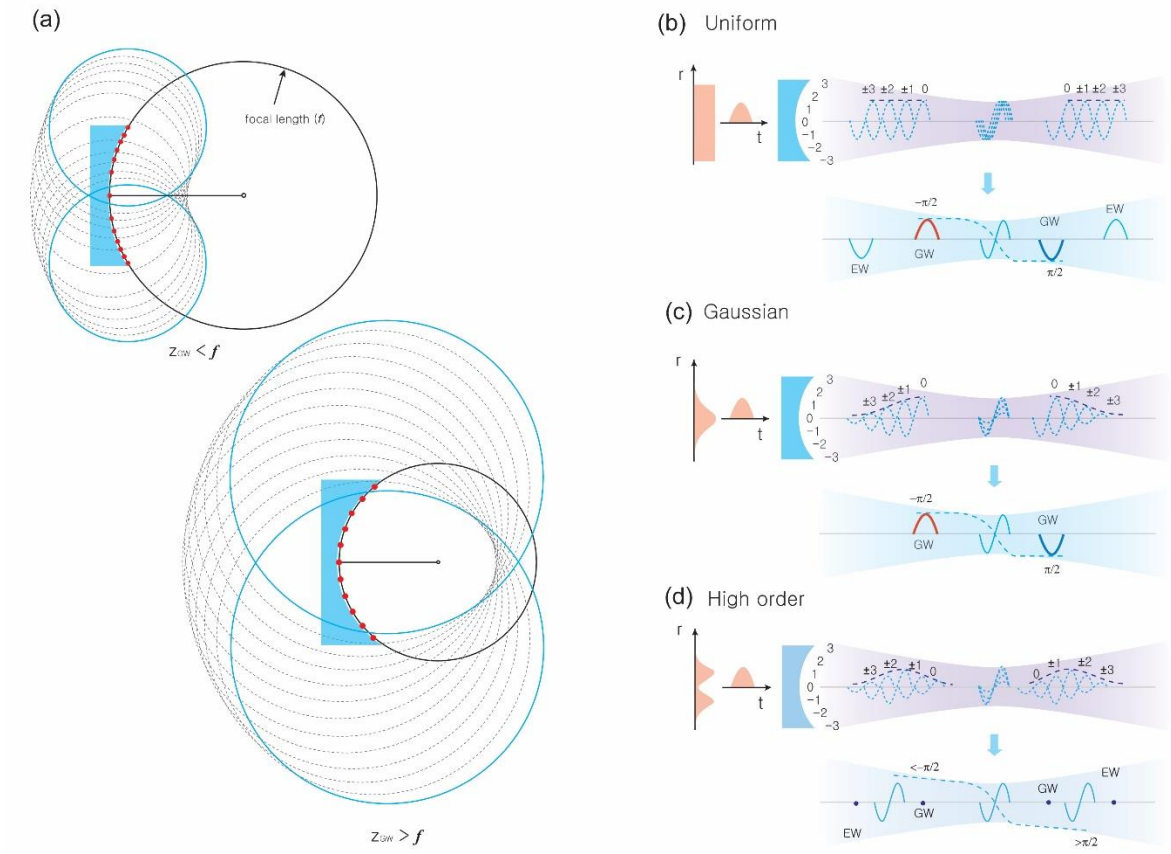

Fig. 4.4 (a) The spread (L), defined as a distance between the edge and geometrical waves, and the spherical secondary waves for radius less and larger than the focal length, respectively. The axial secondary waves (top) and the resulting waves (bottom) for the uniform (b) and Gaussian sources (c). We consider the secondary spherical waves (radius z_{GW}) radiating from the point sources on the axisymmetric concave surface with radius of curvature f and transverse diameter D.

4.2.4 Correlation of phase shift to spread (L)

The polarity reversal is clearly confirmed when the edge and geometric waves are sufficiently separated each other. Furthermore, the phase shift is closely related to the order change. These findings suggest that the phase shift of the focusing waves is correlated with a parameter (L) that quantizes both the sequence change and the distance between the geometrical and edge waves. We will refer L as "spread" in the sense that the secondary waves are distributed over a length of L along the z-axis at an instant time, as illustrated in Fig. 4.5(a). The spread L, the position of the geometrical wave relative to the edge wave ($z_{EW} - z_{GW}$), is geometrically determined with the focal length f and diameter D as follows, $L(z) = L_{\max} + \sqrt{(z+f)^2 - (D/2)^2} - (z+f)$, $L_{\max} = f - \sqrt{f^2 - (D/2)^2}$, where the maximum spread $L_{\max}$ is a length between the edge and the center of the spherical surface along the z-axis. The spread L as a function of the location of the geometrical wave (relative to focal length) are plotted in Fig. 4.5(a) for different source dimensions. The shaded region represents a spread less than the effective wavelength ($\lambda_{eff} = c\tau_d = 1$ mm) that is defined using temporal width of the acoustic wave. The spread L captures the main features of focusing wave. The spread (L) changes its sign from negative into positive with respect to the focus, showing the order change. As the geometrical wave approaches the focus, the amplitude of L decreases, eventually becoming zero (i.e., the two waves arrive simultaneously at the focus). With increasing diameter (D) (*i.e.*, large f/#), the spread increases more drastically with z.

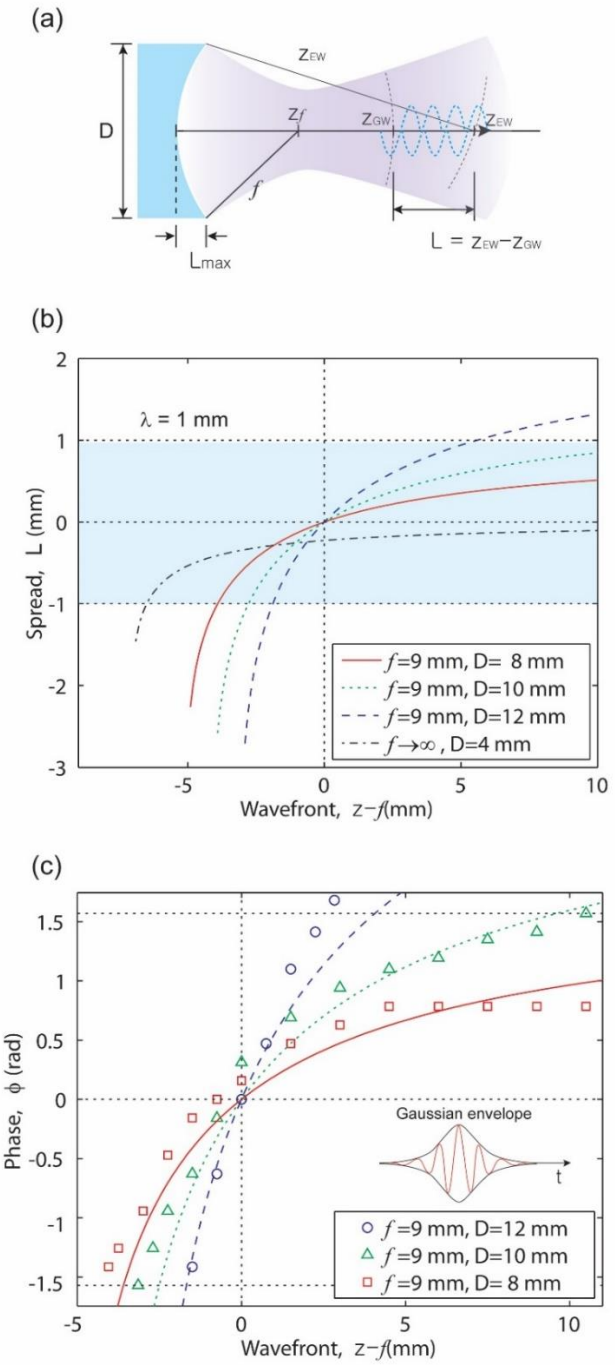

Fig. 4.5 (a) The spread (L) of the secondary waves along the z-axis. The shaded region represents a spread less than the wavelength (λ) (b) Phase shift (ϕ) as a function of z. The symbols indicate the simulation results. The lines are derived from the spread (L).

In a far field ($z\rightarrow\infty$), the spread approaches to $L_{\max}$, because the two waves become parallel to the z-axis. For the planar source ($f\rightarrow\infty$), however, the spread approaches asymptotically to zero, since the edge wave cannot be ahead of the geometrical wave, which could be a reason for a $\pi/2$ phase shift.

The simulated and experimental results show the distinct change in the polarity (i.e., phase shift), especially when the spread (L) is sufficiently large compared to the effective wavelength (λ_{eff}). This suggests that the phase shift (ϕ) could be a function of $L_{\max}/\lambda_{eff}$. Using the paraxial and Gaussian beam approximation, the maximum spread $L_{\max}$ can be expressed as $w_0^2 z/2z_R^2$ where w_0 and z_R are a focal spot size and the Rayleigh length. Thus, the phase shift is represented as $\phi = f(L_{\max}/\lambda_{eff}) = f(z/z_R)$. The result is consistent with that of Gaussian light beam ($\phi = \tan^{-1}(z/z_R)$).

To further understand the relation between the spread (L) and phase shift (ϕ), we simulated phase shift (symbols), then compared with the fit lines (ϕ_{Fit}) that were derived from the spread, more precisely the linearly-scaled spread [$\phi_{Fit} = \alpha\pi L(D,z)/\lambda_{eff}$, where α is a fitting parameter]. Figure 4.5(b) shows the simulated phase shifts and the best-fit lines. In the simulation, since a few-cycle pulse modulated by the Gaussian envelope (see the inset of Fig. 4.5(b)) is applied, the phase shift is calculated by the shift of the carrier wave with respect to the envelope wave. The general trend of the calculated phase shift is well match with the phase shift determined by the linearly-scaled spread. For smaller aperture diameter (D), the spread (L) transits more gradually with z, leading

to gradual phase shift across the focus. In contrast, for large D, the drastic change of the spread results in radical change of the phase. This is analogous to the phase shift Gaussian light beam where large diameter (or small *f*-number) can lead to small focal spot size and thus short Rayleigh length ($z_R = \pi w_0^2 / \lambda$), and ultimately resulting in the drastic phase shift ($\phi = \tan^{-1}(z / z_R)$).This analysis indicates that the spread is indeed in strong correlation with the phase shift. Therefore, the spread, together with secondary waves contributing with temporal derivative of the source waveform, can explain the physical origin of the Gouy phase shift.

4.3 Conclusion

We have demonstrated the Gouy phase shift of a focused acoustic wave using the CNT optoacoustic transmitter, and offered the intuitive explanation of the physical origin of Gouy phase shift. By using Huygens' concept of secondary wave and the Rayleigh integral, the phase anomaly has been understood as a result of a natural sequence change in secondary waves (each contributing with temporal-derivative of the input source), which was parameterized with the spread (*L*). We have found that the parameter *L* could fit the simulated phase shift.

Although the lateral Gaussian source does not produce the edge wave (the order change cannot be explicitly seen), the same explanation is applicable to the phase shift. In this work, the phase shift near a focus exhibited asymmetry, which is contrast to the symmetry phase shift of focused Gaussian beams about the focal point. The difference

might be originated from the fact that sound wave is radiated from the sound baffle (the baffle does not allow backward radiation). The understanding of the phase shift would benefit high-resolution acoustic imaging, e.g. picosecond ultrasonics.

CHAPTER 5

Interference of Laser-induced Acoustic Transient at Impedance Mismatched Boundaries for Controlled Cavitation

5.1 Introduction

Acoustically induced bubbles have been extensively used in applications ranging from ultrasonic cleaning [48] and medical imaging and therapy to sonochemistry [49], because radial collapse of bubbles and liquid jetting (resulting from symmetry breaking) can deliver spatially localized impacts [50]. In particular, bubble formation at solid surfaces has been increasingly important for selective surface modification for functional surfaces [51,52], nano-composite formation [53], and single-bubble sonoluminescence [54]. Moreover, in the recent demonstration of laser-generated focused ultrasound (LGFU) that produces high-amplitude (>50 MPa) and high-frequency (>15 MHz) pressure with a small focal spot size (<100 μm diameter) [1], acoustically induced micro-bubbles can disrupt single cancerous cells, thereby detaching them from the cultured substrate without affecting neighboring cells [20]. This points to a new direction in histotripsy therapy targeting at the cellular-level. Such precise bubble localization can also allow the exploration of microscopic cell responses to high-frequency, high-amplitude acoustic

pressure, e.g., for drug delivery to individual cells [55]. In this regard, reproducible generation of bubbles at desired locations with high spatial accuracy represents a major interest and promising opportunity. However, the control of bubble nucleation at surfaces remains a challenging problem, primarily because of surface heterogeneity that results in uncontrolled (or heterogeneous) bubble nucleation.

Heterogeneous bubble nucleation is the formation of gas bodies stabilized by nucleation sites such as impurities (e.g., hydrophobic particles) and cavities on the surface. The size and hydrophobicity of these nucleation sites determine the nucleation threshold, i.e., a critical tensile pressure required for the bubble nucleation. Thus, the bubble formation process at solid surfaces is stochastic in nature and less controllable, relying on the distribution of the nucleation sites. Successful control of bubbles has been accomplished by either employing artificial nucleation sites such as particles [56] and gas-filled pits [57,58] or by selectively controlling surface wettability [51].

On the other hand, focused ultrasound, which does not require surface modification and introduction of the bubble nuclei, is a promising method for bubble generation as it enables spatial localization of cavitation within a focal volume. High-amplitude focused ultrasound (HIFU) has helped to realize this promise [9,10,12,59-61]. For example, minimally-invasive targeted therapies have been demonstrated in histotripsy [12,60,61]. However, such approaches have typically used low frequencies that lead to a relatively large focal dimension (~ mm), in which bubbles nucleate randomly, or form a cloud of bubbles. Recently, Brujan *et al.* reported generation of a

single micro-bubble near a metal block (aluminum) by using multiple ultrasound pulses with dual-frequency components (~ μs) [62]. However, such an approach is most likely dependent on surface quality, thus it might produce different nucleation characteristics (less controllable) for other surfaces.

In this work, we demonstrate controlled generation of single micro-bubbles, irrespective of the influence of surface heterogeneity on the bubble nucleation process. Surface-insensitive micro-bubble generation is made possible by highly localized negative pressures (negative focal spot size ~ 200 μm) from single short pulse laser-generated focused ultrasound (< 100 ns). Furthermore, due to the acoustic interference by the impedance boundary, the peak negative pressure amplitude (> 50 MPa) exceeds the cavitation threshold of distilled water in a free-field (or boundary-free) condition (-33 MPa [63]). This approach enables single micro-bubble nucleation in a controllable and reproducible manner, offering a new method to explore various interactions between acoustic bubbles and solid materials including biological objects, e.g., cells and tissues.

5.2 Interference of Focused Acoustic Transient at Impedance Mismatched Boundaries

5.2.1 Simulation of acoustic propagation

To study the bubble nucleation process on a water-glass interface subject to a focused acoustic wave, we first examine acoustic interference due to wave reflection by

the impedance boundary. The pressure field in the presence of the interface is substantially different from that in a free-field (boundary-free) condition, thereby having a significant effect on bubble nucleation [64]. To calculate the pressure field, the axisymmetric linear wave equation (in a lossless medium) is numerically solved using a finite element method (the Courant number CFL<0.05; COMSOL Multiphysics 4.3b). Since we focus on a diffraction-limited acoustic spot and the interference effect, the effects of nonlinearity and acoustic attenuation are assumed to be negligible for simplicity. Instead, with an appropriate choice of the initial conditions (initial acoustic pulse), the simulation confirms that, in the absence of the acoustic reflector, the calculated signals at the focus can be well matched with acoustic signals that are measured in a free-field condition.

5.2.2 Acoustic interference at hard boundary

The peak negative pressure field near the glass substrate [$P_i(r,z)$, where r and z are radial distance and axial distance from the acoustic focal point (z=0, r=0)] calculated by the axial-symmetric simulation is shown in Fig. 5.1(a). The amplitude of the pressure field is normalized to the maximum peak negative pressure amplitude in a free-field condition (the boundary-free peak negative pressure, $P_f(r,z)$, has a maximum value at the focus, i.e., $P_f(r=0,z=0)$). Indeed, the acoustic pressure field near the surface (r < 50 μm, z < 50 μm, the blue region) is significantly enhanced by the flat reflector. Importantly, the pressure enhanced blue region is closely related to bubble nucleation

zones that were observed in the experiment. The peak pressure distributions for the lateral (r) and axial (z) directions are shown in Fig. 5.1(b) and (c). The free-field pressure in z direction, $P_f\left(r=0,z\right)$, remains constant within a range of z (z < 200 μm),

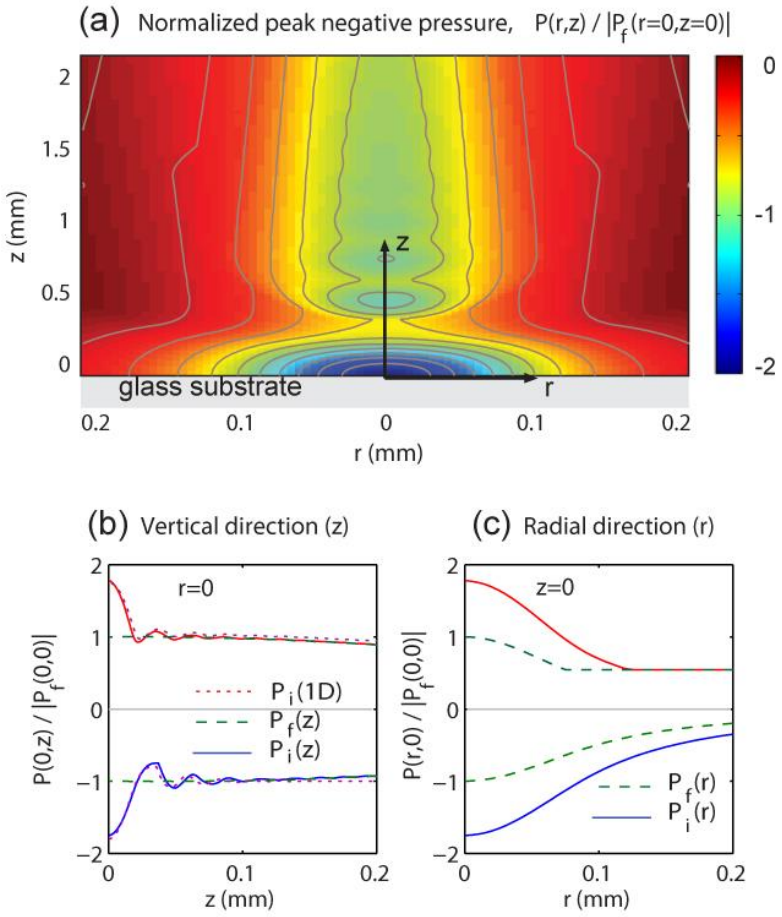

Fig. 5.1 (a) The calculated peak negative pressure field, $P_i(r,z)$, near the glass surface (surface plot with contour lines), normalized to the maximum peak negative pressure amplitude in a free-field (or boundary-free) condition, $P_f(r=0,z=0)$. (b) The peak pressures in the z direction. The interfered pressure, $P_i(\mathrm{z})$, is compared with the free-field pressure, $P_f(\mathrm{z})$. The interfered pressure based on a one dimensional reflection model, $P_i(\mathrm{1D})$, is also plotted for comparison. (c) The peak pressures in the r direction (Gaussian-like profile).

because the upper limit is much less than the Rayleigh length (~ $0.3z_R$) that is determined by using $z_R = \pi w_0^2 / (c / f_c)$, where f_c, c, and w_0 is the center frequency of the measured acoustic signal (~15 MHz), speed of sound in water, and acoustic spot size at the focus, respectively. The interference pressures at the interface, $P_i(z=0)$, are greatly increased up to 1.8 times ($P_i = P_f + R \cdot P_f = 1.8 P_f$). The 1-D reflection model, $P_i(z,t)_{1D}$, which does not consider wave diffraction, is in agreement with the axial-symmetric simulation results, indicating that the pressure augmentation near the interface can be understood as reflection and interference. Meanwhile, the interference pressure amplitudes decrease with r, having a Gaussian-like profile $P(r) \sim \exp(-a \cdot r^2 / w_0^2)$, as shown in Fig. 5.1(c).

By taking the interference effect into account, we can estimate optoacoustic pressure amplitudes that are applied to the solid interfaces for bubble nucleation. Based on the free-field (or boundary-free) pressure amplitudes previously reported [1], the maximum positive pressure at the interface can be estimated as +100 MPa ($1.8 P_{f+}$) and the negative pressure as -50 MPa ($1.8 P_{f-}$). The negative pressures have even higher amplitudes than the acoustic cavitation threshold of distilled water in a free-field condition ($P_{\text{th,water}}$ ~ -33 MPa [63]).

5.2.3 Acoustic interference at soft boundary

Figure 5.2(a) shows the calculated peak negative pressure field (surface plot with contour lines) in water near the free surface, normalized to the maximum negative pressure amplitude in the free field.

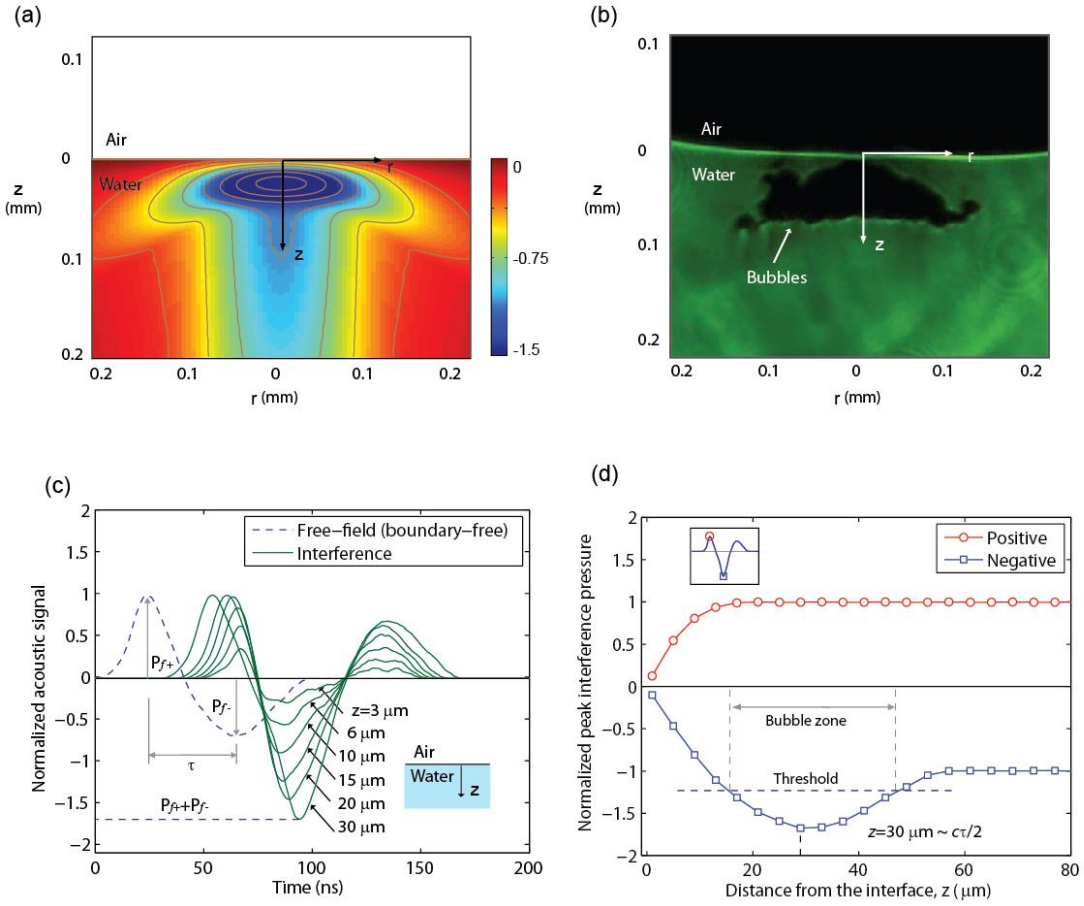

Fig. 5.2 Acoustic interference effect by the air-water interface. (a) The peak negative pressure field near the free surface (surface plot with contour lines, width x height = 400 μm x 200 μm), normalized to the maximum free-field negative amplitude. (b) The shadowgraph image of bubble nucleation zone (laser energy E = 50 mJ/pulse). (c) Normalized pressure transients for different distances form the interface (r = 0; z = 3, 6, 10, 15, 20, and 30 μm). The free-field pressure transient with a bipolar waveform (the positive amplitude = a, the negative amplitude = b, the peak-to-peak time delay = τ) is plotted with a dashed line. The maximum negative amplitude corresponds to the sum of the free-field positive and negative amplitudes (i.e., P_{f+}+P_{f-}) (d) Normalized negative (symbol: blue square) and positive peak amplitudes (symbol: red circle) as function of z. The maximum negative amplitudes at z_{max} = 30 μm (~ $c\tau/2$, where c is the speed of sound).

The blue colored region with high negative amplitudes is laterally confined because of tight focusing of the pressure pulse, which is in good agreement with the measured acoustic spot size of approximately 100 μm. This high-amplitude region is also localized near the interface (z<100 μm). This localization is due to the acoustic interference; the short acoustic wave is reflected from the interface and then is interfered with the rest of the incoming wave. Notably, the blue region with a crescent shape is well matched with the shape of the bubble cloud observed in the shadowgraph image (Fig. 5.2(b)), indicating that the bubbles favorably nucleate in the high-amplitude zone.

To further examine the interference effect, the simulated pressure transients are plotted in Fig. 5.2(c) for different distances (z) along r=0. The dashed signal indicates the free-field optoacoustic signal at the focus that has a bipolar waveform with a leading positive amplitude (P_{f+}), a trailing negative amplitude (P_{f-}), and a peak-to-peak time delay (τ ~ 45 ns). The interference signal transients (solid lines) calculated at different locations (z = 3, 6, 10, 15, 20, 30 μm) carry an additional positive phase (i.e., tri-polar waveforms) due to the acoustic reflection. With increasing the distance z, the signal amplitudes gradually increase. At the locations z>10 μm, the negative amplitudes become higher than that of the free-field, reaching to the maximum value at the distance $z_{\max} = 30\ \mu\text{m}$, which corresponds to the sum of the free-field negative and positive amplitudes (i.e., $P_{f+} + P_{f-}$). The maximum location $z_{\max}$ can be calculated using the peak-to-peak time delay τ by $z_{\max} = c\tau/2 \cong 30\ \mu\text{m}$ (c is the speed of sound) because the maximum occurs when the two peaks of the free-field signal are exactly overlapped. This

suggests that the location of the bubble cloud from the interface, which significantly affects the characteristics of the jetting, can be controlled by the acoustic waveform (more precisely, the peak-to-peak time delay τ). The optoacoustic waveform can be tuned by a laser pulse duration and the thickness of the CNT layer. As shown in Fig. 5.2(d), the positive and negative peak interference pressure (P_i) are plotted as function of *z*. Beyond $z_{\max}$, the negative interference pressure amplitudes decrease down to the free-field amplitude, while the positive pressure amplitudes remain constant. As indicated in the plot, the bubble nucleation zone is defined as a region where the interference negative pressure amplitudes are higher than the threshold pressure.

5.3 Interference at Solid Surfaces: Controlled Generation of Single Micro-bubble at solid surfaces

5.3.1 Bubble dynamics

The bubbles were apparently formed within the duration of the short acoustic pulse (further discussion will follow). Thus, the initial stages of bubble growth are dominated by inertia due to their high rarefaction stress and short duration. The radius of isolated bubbles (*R*) is calculated by using the Rayleigh-Plesset equation assuming spherical symmetry and an adiabatic gas law [65,66]

$$R\ddot{R}+\frac{3}{2}\dot{R}^2=\frac{1}{\rho}\left\{\left(p_0+\frac{2\sigma}{R_0}-p_v\right)\left(\frac{R_0}{R}\right)^{3\gamma}+p_v-\frac{2\sigma}{R}-\frac{4\eta\dot{R}}{R}-p_o-P(t)\right\} \quad (5.1)$$

where R, R_0, ρ, σ, η, p_v, p_0 and $P(t)$ are bubble radius, initial bubble radius, density (ρ = 1000 kg·m^{-3}), coefficient of surface tension (σ = 0.073 N·m^{-1}), water viscosity (η = 1.0×10^{-3} Pa·s), water vapor pressure, static ambient pressure, and applied acoustic pressure, respectively. In the experiment, the acoustic pulse duration (<100 ns) was two orders of magnitude shorter than the measured bubble lifetime. After bubble nucleation, the rest of the bubble dynamics are driven by inertia under static ambient pressure (*i.e.* transient bubble) [67]. The initial bubble radius (R_0) is chosen by a condition that for a given pressure (-20 MPa) bubble expansion is minimal below a certain value for R, whereas above this value much greater bubble growth is observed.

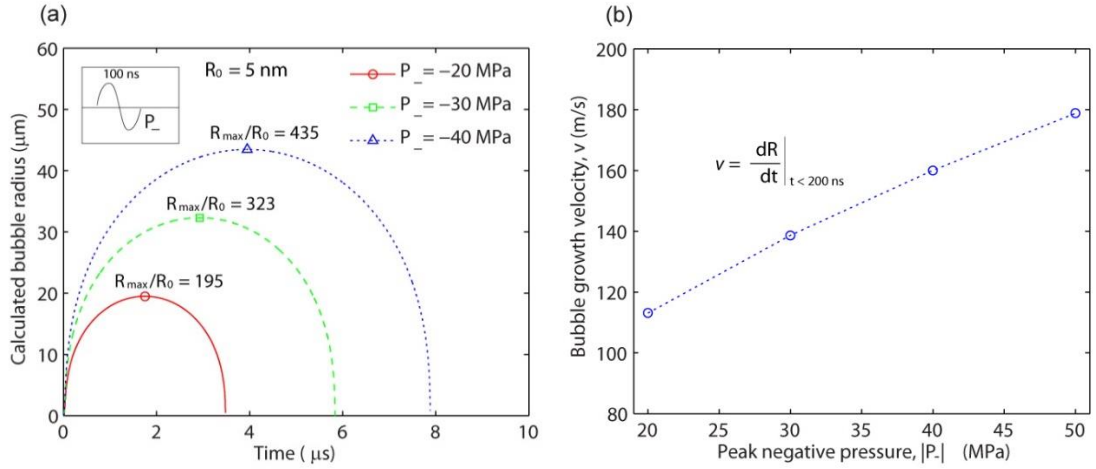

Fig. 5.3 (a) Calculated dynamics of isolated single bubbles for negative pressures (P_-= 20, 30, 40 MPa). (b) The velocity of seed bubble growth at an early time (t < 200 ns).

Figure 5.3(a) shows the calculated bubble radii for different negative pressures with an initial radius of 5 nm. With the short pressure pulses applied, bubbles explosively grow and subsequently shrink (symmetric behavior). The maximum bubble radius increases with the negative pressure amplitude. The ratio of the maximum radius to the initial radius (R_{max}/R_0) is calculated to be over 100. Moreover, bubble lifetime is calculated to be much longer than the acoustic pulse duration. The velocity of the bubble wall reaches as high as 100 m/s as shown in Fig. 5.3(b). Here, our calculation is limited to the isolated free-boundary bubbles. In the experiment, densely packed bubbles nucleated at solid surfaces, interacting with one another. A more rigorous theoretical analysis of bubble nucleation on solid surfaces can be found elsewhere [58,68]. Furthermore, bubble-to-bubble interaction and coalescence are discussed in the literature [57,69].

5.3.2 Shadowgraphs of bubble nucleation, growth, and collapse

Laser-induced acoustic waves and bubbles were visualized by laser-flash shadowgraphy [70]. This imaging technique is a pump-probe method that allows a probe laser pulse (N_2-pumped dye laser, FWHM = 1 ns) to obtain shadow images of the bubbles at a different temporal moment specified by the time delay between the pump (Nd:YAG laser) and the probe pulses through a delay generator (Stanford Research Systems, DG535). Flat glass substrates mounted on a rotational stage were adjusted to obtain images in top view and side view, as shown in Fig. 5.4(c). Single micro-bubble generation, visualized by laser flash shadowgraphy, is summarized in Fig. 5.5 for laser energy of 36 mJ/pulse (~ -41 MPa). Figure 5.5(a) shows bubble dynamics at the glass interface (side view, $\theta = 0°$). The

acoustic wavefront (A_{inc}) generated by the optoacoustic lens was first captured before bubble nucleation (t = -100 ns). The reflected wave (A_{ref}) was observed (t = 100 ns), followed by the primary shock wave (S1) induced by the explosive bubble growth. At a delay time of 1 μs, a thin bubble layer was formed at the surface, and its shape closely matched the blue region of the simulated peak pressure field in Fig. 5.1 (a). The bubble preferentially grew upward and reached the maximum size (t = 11 μs), and then it started to shrink. Interestingly, the shrinkage of the bubble took place in two stages: slow and fast shrinkages. In the slow shrinkage stage, the height of the bubble was nearly constant, while the side walls of the bubble caved inover a relatively long time (from 12 μs to 20 μs), evolving into a "mushroom" shape.

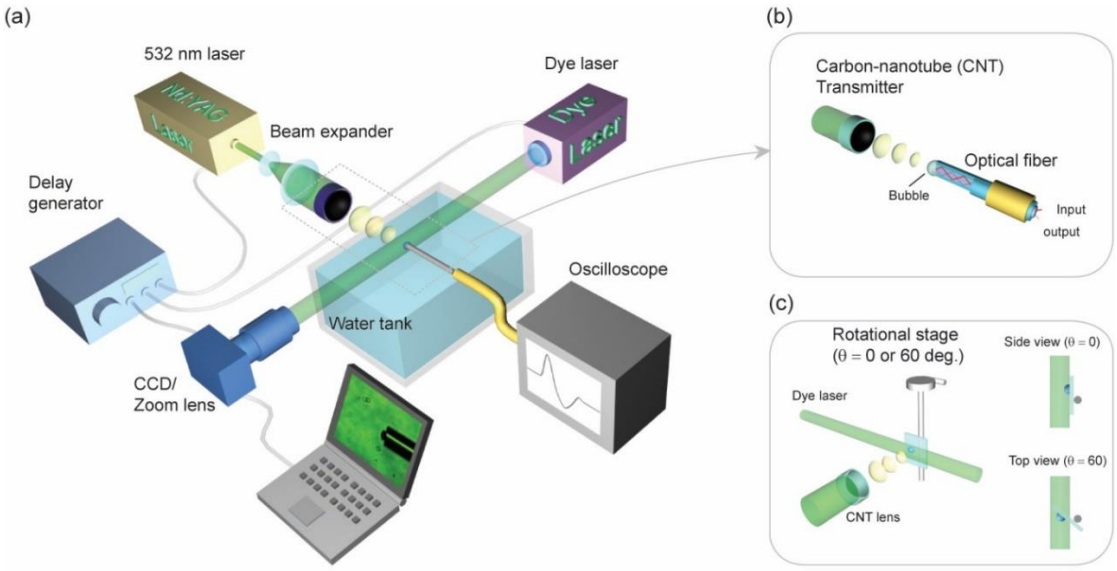

Fig. 5.4 (a) Acoustic signal measurement with and without bubble using a fiber-optic hydrophone. (b) The enlarged illustration of fiber-optic hydrophone measurement and bubble. (c) Visualization of bubble and acoustic wave by varying the angle of the glass substrate: side view (θ = 0°), top view (θ = 60°).

This slow shrinkage process was followed by the fast one, in which the radial collapse of the bubble started (t = 21.7 μs), producing a cavitation shockwave (S2, t = 22.2 μs).

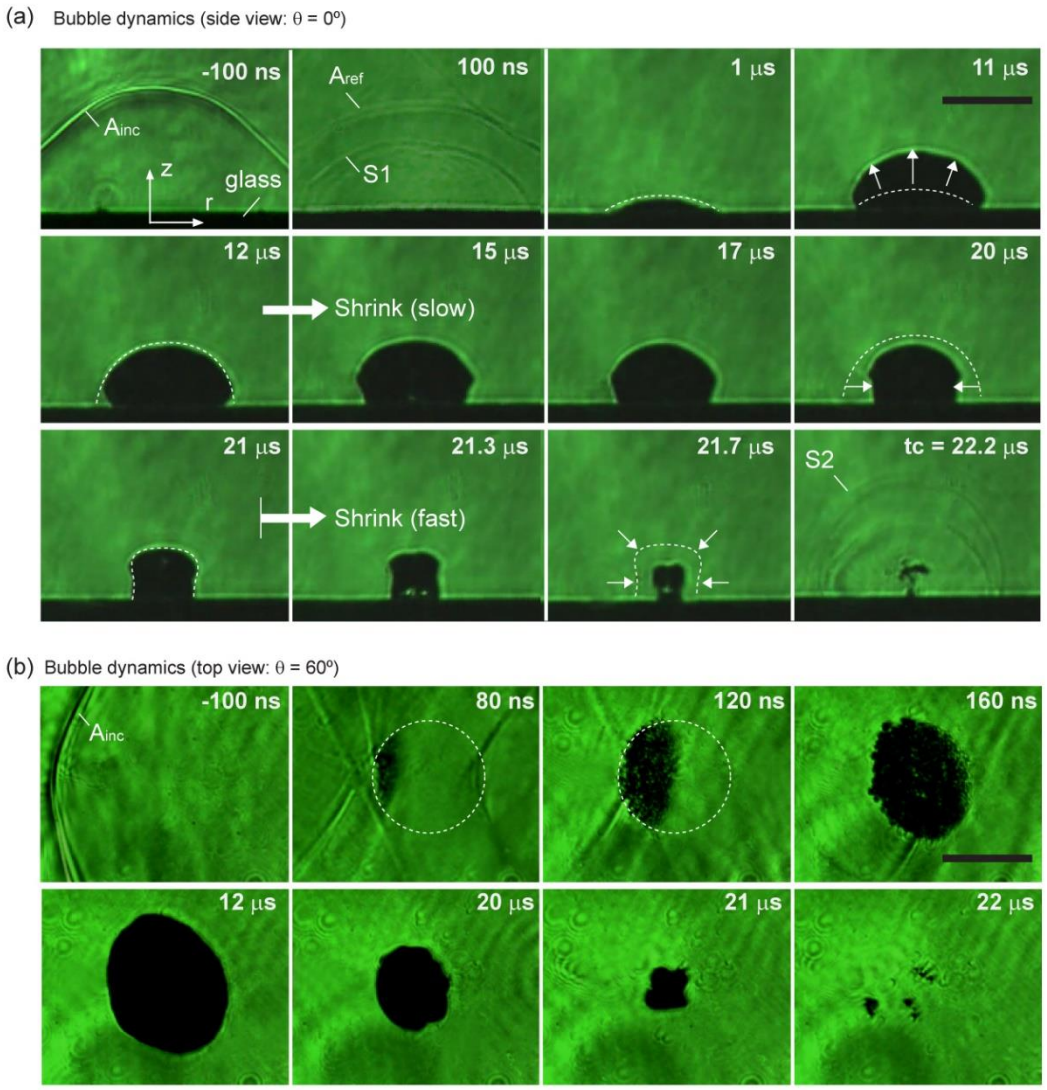

Fig. 5.5 (a) Shadowgraph images of focused acoustic wave and bubbles nucleation at the laser energy of 36 mJ/pulse (~1.8E_w). The single optoacoustic pulses (A_{inc}) are targeted on the flat glass surface. The reflected wave (A_{ref}) followed by the primary shock wave (S1) is observed (t =100 ns). The dashed lines are drawn for comparison. (b) Top-view images in an early stage of bubble nucleation at the glass surface. The surface is slightly tilted with respect to the vertical axis. The circular dashed line represents a nucleation zone. The bar indicates a length of 100 μm.

Since the acoustic bubble here was evolved from the thin bubble layer at the interface, the bubble dynamics exhibit similarity with those induced by the laser excitation of a thin absorbing liquid layer in contact with a glass substrate [47].

The early stage of the bubble nucleation is shown in Fig. 5.5(b) for a top view ($\theta = 60°$). Closely spaced small bubbles started to appear on the left edge of the circular zone (dashed circle) at the glass surface (at t = 80 ns). Note that the glass substrate was tilted with respect to the vertical axis ($\theta = 60°$), thus the left half of the glass was closer to the CNT lens, as illustrated in Fig. 5.4(c). Although some seed bubbles were observed at the edge of the circular area, the dense bubbles formed a thin layer, covering most of the focal area (~100 μm) on the glass surface (by t = 160 ns). The individual seed bubbles were rarely identified after 1 μs as they grew and coalesced into a single large bubble, exhibiting a defined bubble edge in the images. The coalescence of bubbles observed in this experiment stands in sharp contrast to conventional approaches, in which many bubbles form a cloud of separated bubbles[71].

5.3.3 Controlled bubble generation

Merged bubble radii with respect to time are plotted in Fig. 5.6(a) for different laser energies (*E = 14, 19, 22, 39, 51 mJ/pulse*). By assuming hemispherical bubbles, the bubble radius was calculated from the bubble area in the side-view shadowgraph images. The maximum bubble radius and lifetime increased with increasing laser energies.

Characteristic times as a function of the maximum bubble radius are shown in Fig. 5.6(b) for bubble collapse (t_c) and bubble lifetime (t_l). The Rayleigh collapse time (t_R) [72] is plotted for comparison (dotted line). The bubble lifetime (t_l) was more than two times longer than the bubble collapse time (t_c), indicating that the bubble shrinkage proceeded faster than its expansion.

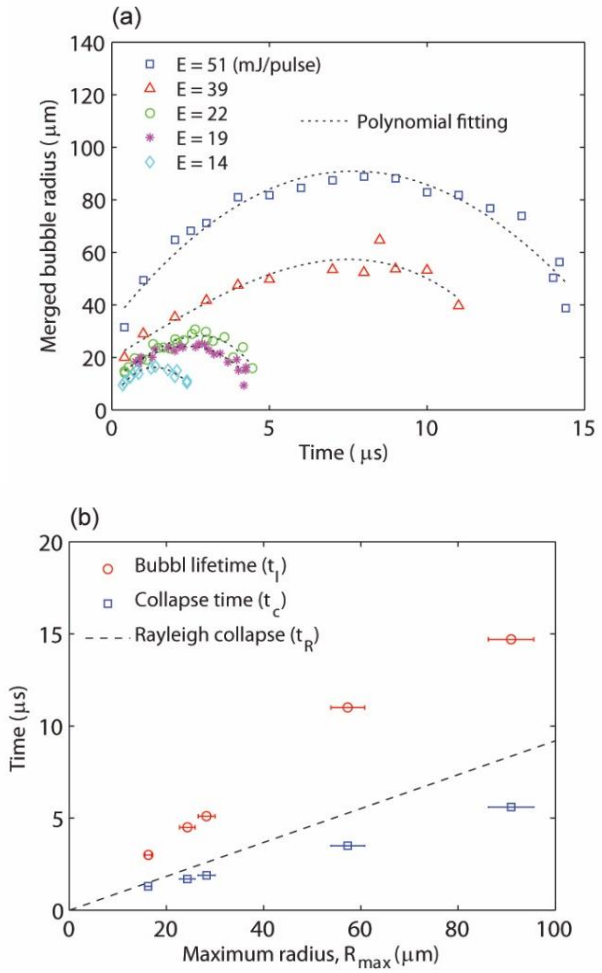

Fig. 5.6 (a) Merged bubble radius as a function of time for laser energies (E = 14, 19, 22, 39, 51 mJ/pulse) and third order polynomial fit lines. (b) Characteristic times of bubble dynamics: bubble lifetime (t_l), collapse time (t_c), and Rayleigh collapse time (t_R).

This might be due to the bubble-bubble interaction and their merging during the bubble growth [56]. Note that the collapse time was even shorter than the Rayleigh collapse time. This discrepancy is because the Rayleigh collapse is defined to describe the symmetric motion of a spherical bubble in an infinite liquid, rather than the asymmetric one shown in our case. The bubble coalescence behavior on the solid boundary was further investigated by monitoring the hydrophone signals. Figure 5.7(a) shows the measured acoustic signals for different laser energies (E = 14, 19, 22 mJ/pulse).

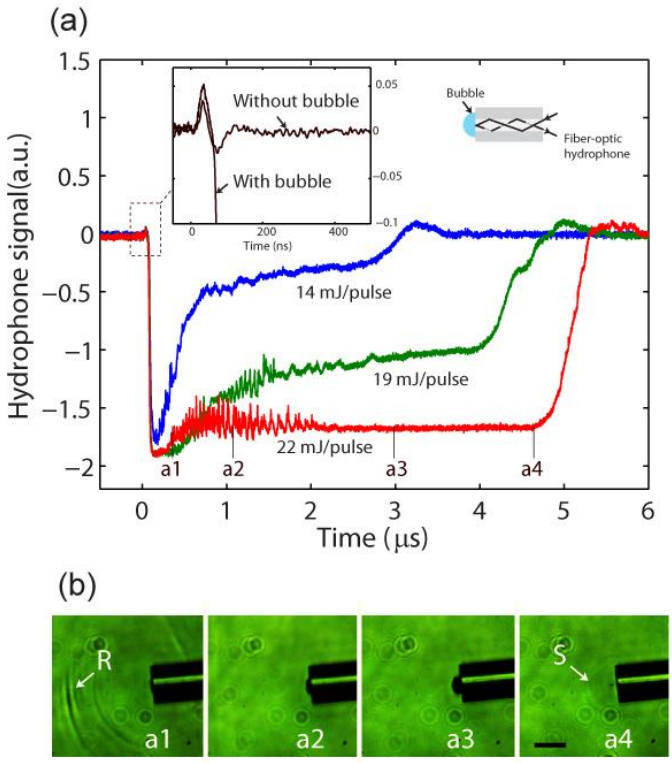

Fig. 5.7 (a) The hydrophone signals for laser energies (E = 14, 19, 22 mJ/pulse). The temporal durations of the signals corresponded to the bubble lifetimes. The inset shows difference between signals with and without bubbles at the tip of the hydrophone. (b) The shadowgraph images of bubbles at the tip of fiber-optic hydrophone (6 μm core and 125 μm cladding diameter) at a laser energy of 22 mJ/pulse (1.6 E_{th}) for correlating the measured acoustic signal. The bar indicates a length of 100 μm.

The measured signals exhibited different characteristic depending on the presence of bubbles at the tip of the hydrophone, as shown in the inset of Fig. 5.7(a). Without bubbles, the hydrophone detected a single bipolar acoustic pulse (<100 ns pulse duration). However, with bubbles, the hydrophone cannot capture full (positive and negative) acoustic signals, because the negative signals were distorted by the bubbles that can significantly increase negative signal amplitudes due to a large refractive index contrast between the vapor bubble and the hydrophone tip. Instead, the negative signals contained useful information on bubble dynamics. Firstly, the rapid increase in the negative amplitude reveals that the bubble starts to expand rapidly within the acoustic pulse duration as short as t<100 ns. Secondly, the temporal duration of the signal corresponded to the bubble lifetime. Once the negative amplitude reached its maximum value, it then decayed over a relatively long period, on the order of several μs. The signal eventually returned to a positive value after the bubble collapsed. Thirdly, the negative signals showed a signature of the merging process of individual micro-bubbles. By correlating the measured hydrophone signals (E = 22 mJ/pulse) with time-resolved images (a1~a4 in Fig. 5.7(b)), we confirmed that during bubble merging, the signals were highly oscillatory (0.1~2 μs). After bubble merging, the hydrophone signals became relatively stable over a longer time (> 2 μs), because the single merged bubbles completely covered the sensing zone on the fiber tip (6-μm core and 125-μm cladding diameter). Figure 5.8(a)-(c), lower panel, show the bubble nucleation for the two different glass surfaces. Depending on pressure amplitudes, bubble nucleation exhibited different characteristics; in weak negative pressures bubbles nucleated preferentially at the micro-holes, whereas strong

negative pressures made the micro-structure irrelevant, generating a large merged bubble. Specifically, when the negative pressure amplitudes were slightly higher than the nucleation threshold of the glass substrate with the micro-holes but less than the threshold of the smooth glass ($|P_{th,micro}| < P_{-} < |P_{th,nano}|$), a few micro-bubbles (< 10 μm) nucleated only at the micro-holes on the patterned glass, as shown in Fig. 5.8(a) for P_{-} = 16 MPa.

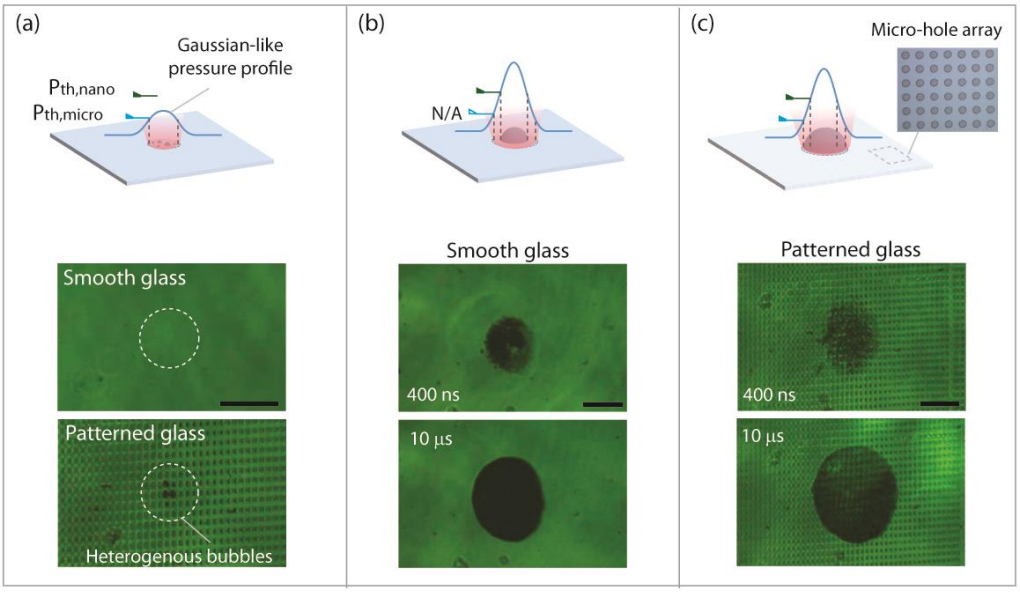

Fig. 5.8 (a) At low negative pressure ($|P_{th,micro}| < P_{-} < |P_{th,nano}|$), heterogeneous bubble nucleation on the patterned glass ($P_{th,nano}$ = -24 MPa, P_{-} = 16 MPa, $P_{th,micro}$ = -14.3 MPa). At high negative pressure amplitudes ($P_{-} >> |P_{th,nano}|$; P_{-} = ~ 44.8 MPa), controlled micro-bubbles on the smooth glass (b) and on the patterned glass (c). The inset of (c) shows the microscope image of the glass patterned with a micro-hole array (8 μm in diameter, 20 μm in spacing). The bar indicates a length of 100 μm.

The observed bubbles are typical characteristic of heterogeneous bubble nucleation (thus, we will refer the zone as a 'heterogeneous' nucleation zone, and its diameter as d_H). In contrast, at strong negative pressures (P_- = 44.8 MPa > $|P_{th,micro}|$), the glasses with and without the micron holes showed no qualitative difference in the bubble nucleation process. As shown in Fig. 5.8(b) and (c), the densely-packed tiny bubbles (t = 400 ns) were merged into a single large bubble (~ 100 μm) at a later time (t = 10 μs).

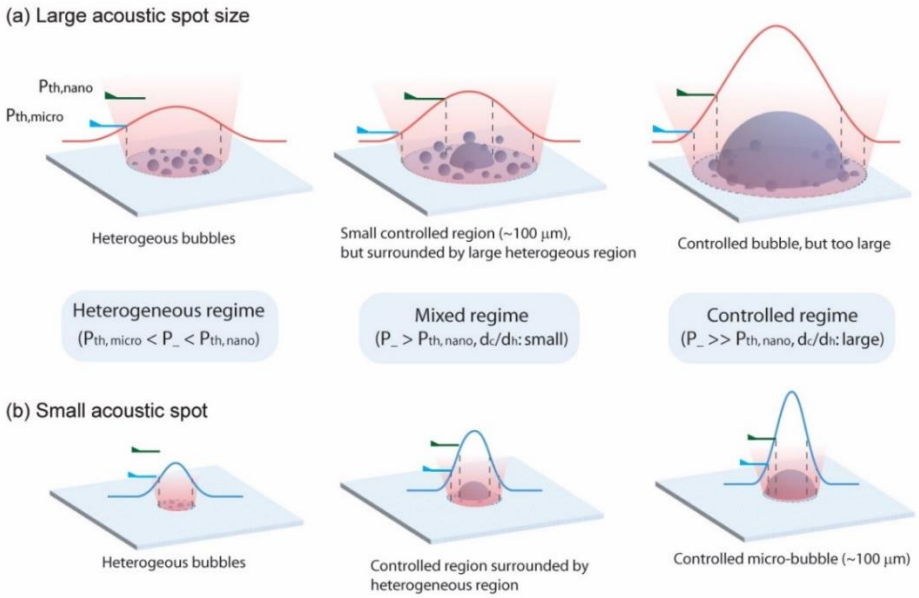

Fig. 5.9 Bubble nucleation characteristics categorized by three regimes for a large acoustic spot (a) and a small acoustic spot (b): Heterogeneous regime ($|P_{th,micro}| < P_- < |P_{th,nano}|$), Mixed regime ($P_- > |P_{th,nano}|$), and Controlled regime ($P_- >> |P_{th,nano}|$). (a) For a large acoustic spot, small controlled region (~ 100 μm) can be produced in the mixed regime, but it is surrounded by a large heterogeneous region. By further increasing pressure amplitudes (controlled regime), controlled bubbles nucleate, but too large (close to spot size, w_0). (b) For a small spot size, controlled micro-bubbles nucleate in the controlled regime.

However, the bubble zone and the merged bubble were slightly increased by the micro-holes (Fig. 5.8(c)). Bubble nucleation characteristics can be categorized by three regimes: heterogeneous regime, mixed regime, and controlled regime, as illustrated in Fig. 5.9 for large and small acoustic spot sizes. In the heterogeneous regime where peak negative pressure amplitudes are higher than $\left|P_{\text{th,micro}}\right|$, but lower than $\left|P_{\text{th,nano}}\right|$, bubbles nucleate preferentially. In the mixed regime ($P_{-} > \left|P_{\text{th,nano}}\right|$), a small controlled region is surrounded by a large heterogeneous region (i.e., low $d_{\text{C}} / d_{\text{H}}$). In this regime, even with a large acoustic spot, a small controlled bubble ($d_{\text{C}} \sim$ 100 μm) can be produced, but a much larger heterogeneous bubble zone is unavoidable due to potential surface heterogeneity (or lower nucleation threshold). By further increasing negative pressure amplitudes, the characteristics of bubble nucleation fall into the controlled regime where densely populated bubble nucleate and subsequently coalesce, forming a single large bubble. In the controlled regime ($P_{-} >> \left|P_{\text{th,nano}}\right|$) with high $d_{\text{C}} / d_{\text{H}}$, the size of the merged bubble approaches to the acoustic spot size (w_0); with a large acoustic spot, large controlled bubbles nucleate. Thus, controlled micro-bubble (~ 100 μm) requires not only small acoustic spot, but also high pressure.

5.4 Interference at Free Surface: Nozzle-free, high-speed Liquid Micro-jets by Homogeneous Nucleation

5.4.1 Nozzle-free liquid microjetting

Liquid jetting accompanied by droplet formation is widely observed in nature. The underlying mechanisms of liquid jetting vary with different driving forces, leading to different characteristics of jets (e.g., jet column width and jet speed). Particular interest has been given to micro-sized liquid jets for applications ranging from needle-free drug injection [73,74] to high-resolution inkjet printing [75]. Among various jetting methods, the simplest one is based on the incompressibility of liquid; a small amount of liquid is pushed out of a nozzle due to the volume change induced by the deformation of a piezoelectric-driven membrane [76] or by the expanding bubble within a liquid container that is thermally generated by a pulsed laser [77], an electric discharger [78], or an electric heater [79]. Alternatively, high-speed jets are produced by an impulsive acceleration that occurs when a tube filled with a liquid falls under its own weight onto a solid surface [80,81]. More recently, Tagawa *et al*. reported supersonic micro-jets (jet speed up to 850 m/s) produced by laser-induced bubbles and consequent shock waves in an open liquid-filled capillary when the liquid surface inside the tube forms a concave meniscus [82].

The aforementioned approaches either require nozzles (or equivalent) to eject liquids from containers or to form a concave liquid meniscus, which makes it vulnerable to nozzle clogging, especially when jetting liquids contain flakes, particles, or surface-adhesive biological molecules (e.g., proteins). Some applications such as drug injection require high-speed jets to penetrate resistive and lipid-rich skins [73]. These call for a

nozzle-free high-speed jetting. The existing nozzle-free jetting schemes have shown promise, but they have limitations [73,83-86]. For example, a high intensity acoustic beam can lead to liquid ejection when it is focused to the air-liquid interface, but the jets have relatively slow speed [83]. Earlier work showed that high-speed jets (up to 250 m/s) could be produced by bubble collapse near the air-liquid interface, but in an uncontrolled manner [84]. Recently, jetting of a highly viscous liquid was demonstrated through the interaction between a laser-induced spherical bubble and the air-liquid interface [85,86]. In this process, the bulk liquid needs to be optically transparent to laser light. Moreover, the laser-based method may not be suitable for thermally unstable materials since high temperature can change the material properties (e.g., the efficacy of drugs, especially protein-based materials), limiting its use in some practical applications.

In this work, we demonstrate nozzle-free, high-speed liquid micro-jetting through a non-thermal process by using a short focused acoustic pulse (<100 ns), which is generated by a recently developed carbon-nanotube (CNT) optoacoustic transmitter capable of tight focusing (approximately 100 μm spot size) [1]. High-speed jets (up to 200 m/s) are induced by the impingement of the short acoustic pulse on the air-water interface and subsequent cavitation. Due to the acoustic scattering from the pressure-release boundary, the negative amplitude of the optoacoustic pulse is significantly increased up to 80 MPa, even exceeding the homogeneous nucleation threshold of water. Two types of jets during the process are observed: primary slow jets caused by initial bubble growth and secondary fast jets produced by bubble collapse. We show two possible applications: liquid printing on a substrate and liquid injection into a tissue-

mimicking material.

5.4.2 Visualization setup of liquid microjetting

The jetting process is visualized by the laser-flash shadowgraph technique [8,15,70], a pulsed pump-probe method that allows a probe laser pulse (N_2-pumped dye laser, FWHM = 1 ns) to obtain images at different temporal moments specified by the time delay between the pump (for exciting optoacoustic wave) and the probe pulses through the delay generator (Stanford Research Systems, DG535). Time-resolved images of the acoustic waves, bubbles, and jets can be captured in the nanosecond resolution, which is determined by the probe beam with a short exposure time of 1 ns. The visualization experiment is conducted with two different setups: the air-side setup for examining jetting and the water-side setup for bubble dynamics, as illustrated in Fig. 5.10(b). This is because significant light scattering from a non-flat liquid meniscus induced by surface tension makes it difficult to monitor phenomena that occur in close proximity of the air-water interface. For the air-side imaging, the chamber is slightly overfilled with the water, forming the free surface with a concave-down meniscus. For the water-side imaging, we use a large air pocket (a few mm in diameter) injected by a glass syringe through a capillary tube (inner diameter: 500 μm). The air pocket forms the air-water interface with a concave shape and is much larger than the bubbles formed by the focused acoustic waves. The location of the interface relative to the acoustic focus is precisely controlled by moving the air pocket along the acoustic propagation direction.

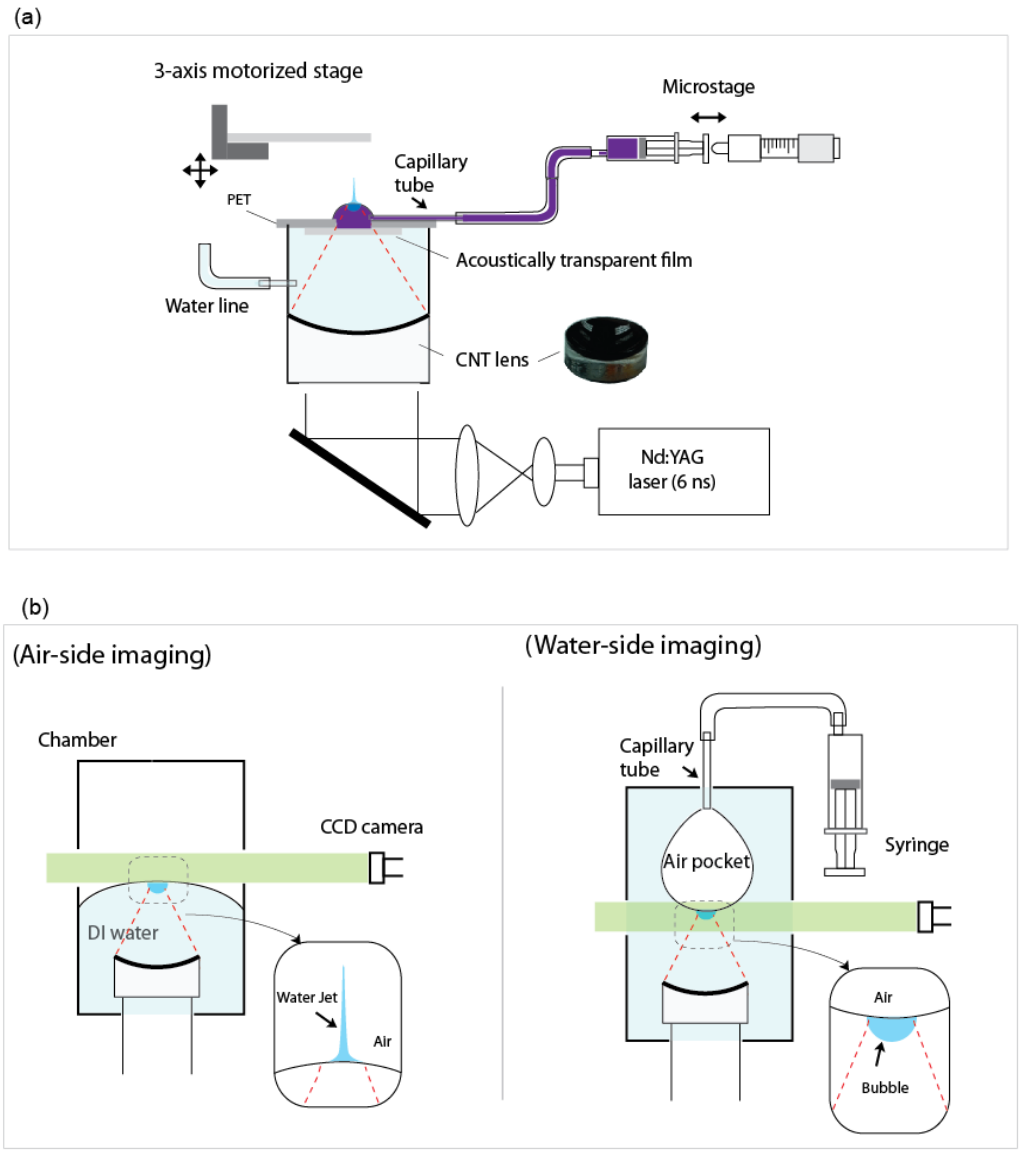

Fig. 5.10. (a) Experimental setup for bubble generation and liquid jetting. The focused optoacoustic wave is generated by pulsed excitation of the carbon-nanotube (CNT) optoacoustic transmitter (i.e., CNT lens). The jetting liquid fed through a capillary tube is separated from water by an acoustically transparent film. (b) Visualization of jetting with the air-side imaging setup where the chamber is overfilled with water, forming the free surface with a concave-down shape. (c) Visualization bubble nucleation with the water-side imaging setup where the large air pocket forms the air-water interface with a concave-up shape.

5.4.3 Shadowgraphs of micro-jets

The optoacoustic waves generated by the concave CNT lens propagate in the water toward the air-water interface, impinging on the interface and consequently producing water jets in the air.

To examine the jetting process, micro-jets in the air are monitored by the back-illuminating shadowgraphy technique. The time-resolved images are summarized in Fig. 5.11(a). At a laser energy of E=50 mJ/pulse, two consecutive micro-jets are observed for 15 μs after the impingement of the waves: a primary slow jet and a secondary fast jet. First, the primary jet starts to emerge from the air-water interface after the focused optoacoustic pulse arrives at the interface (t=1 μs). The water jet continues to grow until it reaches its maximum height and then the height of the jet decreases due to surface tension, which is in turn followed by the secondary fast jet (t=9 μs) that grows more rapidly than the primary jet. The jet height evolution is plotted in Fig. 5.12(a), exhibiting two different peaks, each corresponding to the primary and secondary jets, respectively**.** It is observed that the second peak is higher than the first one, as the height of the secondary jet is higher than that of the primary jet. Moreover, the secondary jet is much faster than the initial jet. As shown in Fig. 5.12(b), the jet speed linearly increases with laser energy. With E>50 mJ/pulse, the secondary jets can reach up to 200 m/s, while the primary jets up to 50 m/s.

To elucidate the mechanism underlying the consecutive jet formation, we then

visualize the water side at the same laser energy as for the jet imaging (Fig. 5.11(b)).

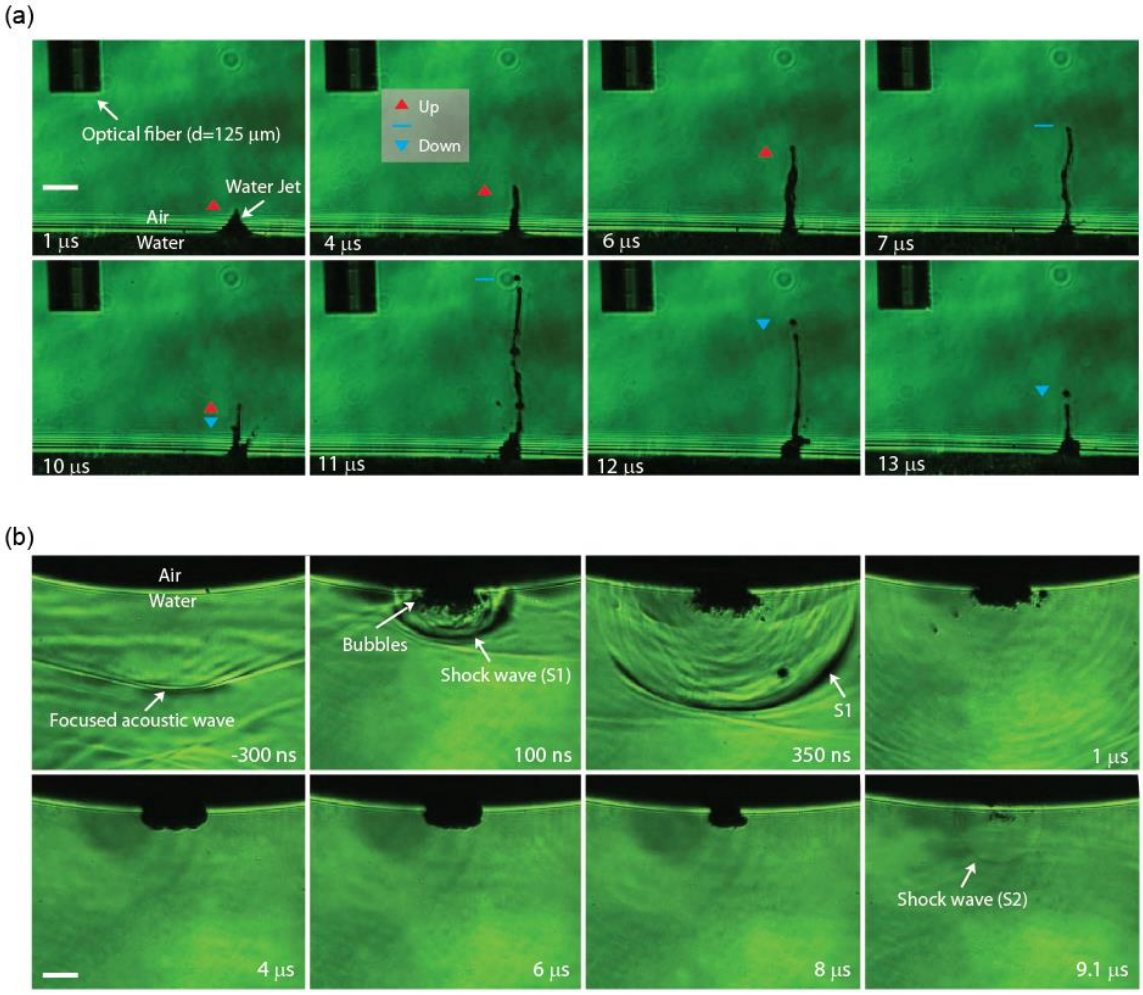

Fig. 5.11 Shadowgraph images of water micro-jets (a) and bubbles (b) at the air-water interface (laser energy E = 50 mJ/pulse). (a) Jet formation in the air side. The light-scattering objects such as the free surface with a concave-down shape, the jets, and the optical fiber look black, while the air is colored as green. The optical fiber (125 μm in diameter) is recorded as a reference object with a distance of approximately 350 μm from the free surface. The symbols indicate the up/down of the jets. (b) Bubble nucleation at the air-water interface. Note the change in the color scheme: the transmitted light through water is colored green, whereas the air pocket, bubbles, and shock waves that can scatter back-illuminating light are colored black. Two shock waves are observed: the primary shock wave (S1) generated by bubble nucleation, the secondary shock wave (S2) by collapse of the bubble. The bar indicates a length of 100 μm.

The densely-packed bubbles nucleate in the immediate subsurface 100 ns after the short focused pressure pulse hits the air-water interface.The rapid bubble formation can contribute to the primary jet production by pushing the surrounding water, which is evidenced by the observation of the shock wave (marked as S1).

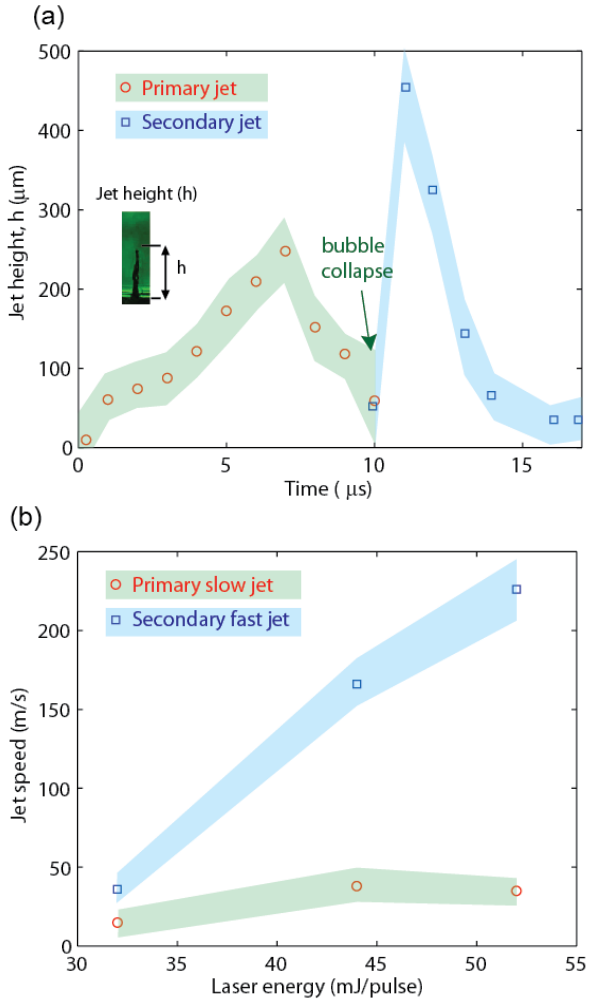

Fig. 5.12 The characteristic of water micro-jets. (a) The height (*h*) of micro-jets as a function of time (*E* = 50 mJ/pulse). The two different jets indicated by shaded regions with different colors are observed before and after the bubble collapse: the primary slow jets (before the bubble collapse) and the secondary fast jets (after the bubble collapse). The bubble collapse is marked with a green arrow. (b) The jet speed as a function of laser energy (mJ/pulse). The primary jets with a relatively slow speed (symbol: red circle) induced by the bubble growth (up to *V* = 35 m/s). The secondary jets with a high speed (symbol: blue square) produced by the bubble collapse (up to *V* = 250 m/s).

Note that the shock wave can be differentiated from the incoming optoacoustic wave with larger radius of curvature (*t*=- 300 ns). The bubble cloud coalesces into a single large bubble with a defined bubble edge, but the bubble zone remains similar in size until *t*=6 μs because bubbles can leave the bubble nucleation zone before coalescing. Finally, the bubble collapses at *t*=9.1 μs, generating a secondary shock wave (S2). By correlating the cavitation images with the jetting images, we find that the bubble collapse coincides with the inception of the secondary jet. This indicates that the secondary fast jet is induced by the bubble collapse, while the primary slow jet is related to initial bubble growth and the impingement of the focused optoacoustic wave. As compared with the bubble growth, the bubble collapse can yield a localized pressure, thus producing the secondary jet with higher speed and smaller column width than the primary jet.

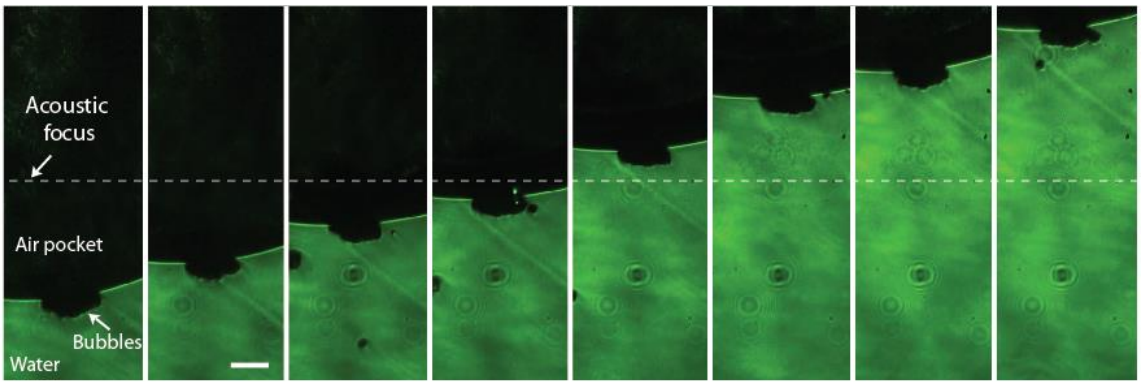

Fig. 5.13 Bubble nucleation tolerable to a change in the position of the free surface (*E* = 50 mJ/pulse). The acoustic focus indicated by a dashed line is fixed while by adjusting the position of the air pocket the air-water interface is moved up and down within the acoustic focal length (approximately 500 μm). All the images are captured at *t* = 1 μs (unless otherwise specified). The scale bar indicates a length of 100 μm.

The shape of the air-water interface is crucial for the jet formation and the bubble hydrodynamics. It has been reported that a concave-up interface (toward the air) with a smaller radius of curvature can promote the kinematic focusing of the liquid, thus producing high-speed jets, whereas the focusing is lost for the interface with a concave-down shape [10]. In this work, for the air-side imaging, the interface is almost flat, no significant focusing is expected. In contrast, for the water-side imaging, the liquid interface is noticeably curved, forming a concave-up shape with a radius of curvature 2 mm (much larger than the bubble zone 200 μm in diameter). To compare with the work above where they examined the effect of contact angle (as the concavity of the interface) on liquid focusing, we estimate the contact angle by assuming a capillary of 400 μm in diameter to, which is higher than 80°, possibly leading to reduced liquid focusing. However, the important thing is whether the curved surface would significantly change the bubble lifetime. If so, the comparison between the results from the two setups is no longer valid. As reported in the literature[87], bubble lifetime (first oscillation) decreases with decreasing radius of curvature. Using the radius of curvature, the distance between bubble and liquid interface, and bubble radius, a decrease in the lifetime is calculated to be less than 5% compared to that for the flat interface (see the supporting material for the detailed calculation)

Similarly, the two consecutive jets were observed elsewhere [88] by employing a shock-wave lithotripter for acoustic cavitation. Contrast to our nozzle-free jetting, their approach used a micro-hole in a silicon plate, which not only served as an bubble

nucleation site but also as a nozzle to eject a water jet. However, possibly, because of the friction between the water and the micro-hole (500 μm in depth), the jet speed was slower than ours, and the primary jet was overlapped with the secondary jet (referred to as the ring jet in their work). Moreover, our jetting is different from what was observed in laser-induced spherical bubbles interacting with the free surface [85,86]. The thermal bubbles did not generate the secondary jets, but primary slow jets toward the air and simultaneously a counter-jet toward the bulk liquid. This difference may arise because the dynamics of the laser-induced single spherical bubbles is substantially different from that of the non-spherical bubble cloud in this work.

5.4.4 Potential applications

We show two potential applications including printing on a substrate and liquid injection into a material. First, we demonstrate liquid printing on a glass substrate. Since it is confirmed that the jetting depends on the applied laser energy, the jetting can be tuned to eject a single droplet by regulating the laser energy (E = 32 mJ/pulse) to realize controllable printing. We find that the size of the single droplet, which determines the printing resolution, is approximately 20 μm in diameter at such a laser energy. By moving the substrate through a motor-driven stage, liquid droplets are deposited on the glass substrate, as shown in Fig. 5.14(a). Each spot is formed by multiple laser pulses to obtain a sizable liquid droplet. With the motorized system, the letter ‘M’ is printed on the

glass substrate, and a microscope image is shown in Fig. 5.14(b). The line width is approximately 30 μm, slightly larger than the droplet diameter. This demonstrates capability of our jetting method for high-resolution printing. However, the printed letter had slight liquid splashes, which can be improved by optimizing several parameters, including laser operating conditions (such as energy, repetition rate), substrate moving speed, and more importantly a distance between bubbles and the liquid surface.

Using the high-speed jets jets (up to 200 m/s), we demonstrated liquid injection into a tissue-mimicking gel (agarose gel). For visual confirmation, we used a watercolor blue ink as a drug substitute.

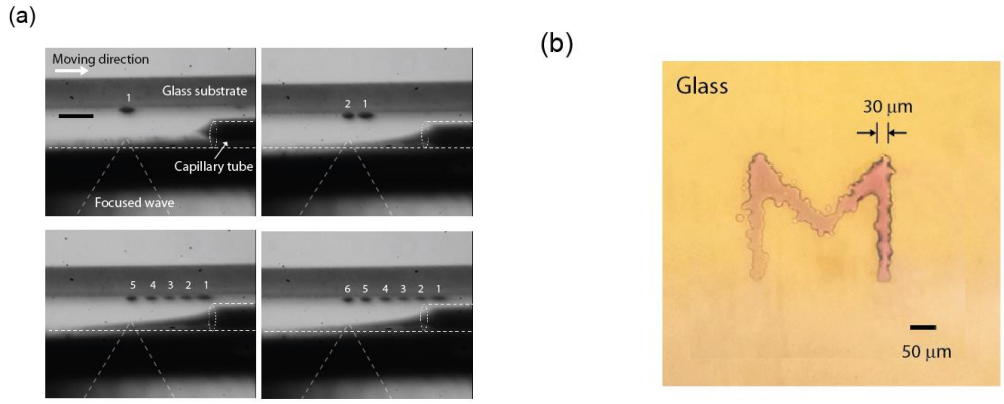

Fig. 5.14 (a) Liquid printing onto the glass substrate (E = 35 mJ/pulse). Each spot is made by multiple droplets while moving the glass substrate toward the right. The bar indicates a length of 500 μm. (b) Microscope image of the letter 'M' printed onto the glass substrate (E = 35 mJ/pulse). The line is a width of 30 μm, which is surrounded by liquid splashes or droplets. The bar indicates a length of 50 μm.

Figure 5.14 shows jet-induced injection of the ink into the gel. The gel with 1 mm thickness is placed right above the air-ink interface. The color ink can penetrate into the material by applying several jets, which is clearly shown as the number N of applied jets increase (N = 0, 1, 2, 3, 10, and 20). The jets can be used for drug injection that requires a significant driving force to penetrate resistive, lipid-rich skins. Although additional optimization may be necessary for actual skins, this preliminary result demonstrates the feasibility of our approach to needle-free drug injection.

5.5 Conclusion

We have demonstrated and analyzed controlled generation of a single micro-bubble at solid surfaces. Our approach enables a tight confinement of a single merged micro-bubble with micro-scale accuracy, regardless of surface-induced heterogeneity.

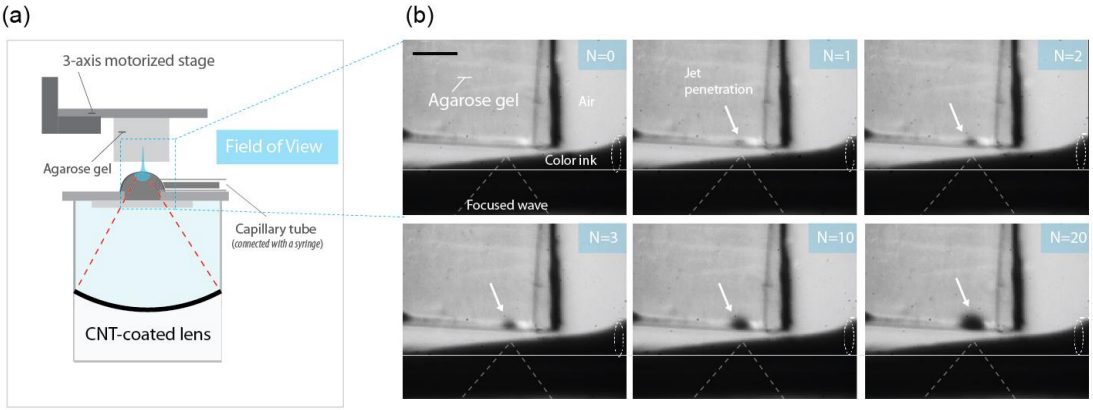

Fig. 5.15 Color ink injection into a tissue-mimicking material (agarose gel, thickness: 1 mm) at E = 50 mJ/pulse. The blue ink penetrates into the gel (marked as white arrows) for different number N of applied jets (N = 0, 1, 2, 3, 10, and 20). The bar indicates a length of 500 μm.

The ability to control bubble formation can lead to new applications in cell level therapy, e.g., ablation of individual cancerous cells (micro-histotripsy), and precise cell sonoporation or disruption [8,20] and selective surface modification, all enabled by a single, nanosecond pressure pulse produced from the optoacoustic lens.

Also, we have demonstrated a nozzle-free high-speed liquid micro-jet produced by acoustically generated bubbles near the air-water interface. The micro-bubbles were homogeneously nucleated by a focused nanosecond-long pressure pulse generated by the efficient carbon nanotube (CNT)-based light-to-sound converter. The homogeneous bubble nucleation was enabled by the acoustic scattering of a nanosecond-long pressure pulse from the air-water (pressure-release) boundary. Two consecutive micro-jets were influenced by bubble dynamics: primary slow jet by initial bubble growth and primary fast jet by bubble collapse.

Our approach has several practical advantages. First, this approach can broaden choice of jetting materials. With the nozzle-free method, we can even use materials that contain particles or flakes whose sizes are comparable to the size of typical nozzles. This acoustic approach frees one from choosing only optically (or weakly absorbing) and thermal stable materials. Second, high-speed jets (> 200 m/s) are readily attainable by taking advantage of bubble collapse, which can allow liquid injection to skins. Third, our jetting method is quite tolerable to a change in the position of the liquid surface within the acoustic focal length (approximately 500 μm), which makes our process more

controllable even when the liquid level is slightly changed for some reasons such as evaporation and jetting liquid consumption.

Based on the above advantages, our process can allow many potential applications. We demonstrated two possible applications, among others: printing and liquid injection into tissue mimicking materials.

CHAPTER 6

High Focal Gain for Boundary-free Cavitation and its Application

6.1 Introduction

Laser-generated focused ultrasound (LGFU) is an emerging modality that enables high-precision ultrasonic treatment *via* shock and cavitation effects onto a microscale focal spot [1,8,20]. Instead of using typical piezoelectric transducers, this approach utilizes a pulsed laser beam to excite a light-absorbing transmitter and produce high-amplitude ultrasound by photoacoustic effect [23]. Due to an availability of narrow temporal widths (<10 ns) of laser pulses, broadband and high-frequency (f >15 MHz) ultrasonic pulses could be generated and focused to a tight spot of ~75 μm [1]. Simultaneously, high-amplitude pressure output (tens of MPa) could be produced by using a thin-film transmitter that efficiently converts an input optical energy to the output focal pressure. For LGFU, a focal transmitter called photoacoustic lens has been used such as a carbon-nanotube (CNT)-polydimethylsiloxane (PDMS) composite film that exhibits an extraordinary photoacoustic conversion efficiency with two orders-of-magnitudes higher than those of typical metal films [1]. Under pulsed laser excitation, the photoacoustic lens could produce a peak positive pressure of >50 MPa and a peak negative (tens of MPa) sufficient for acoustic cavitation on a detector surface [1].

As both high frequency and high amplitude are achieved together, LGFU has been employed for a variety of areas for precision ultrasonic treatment: selective removal of a single cell from neighboring cells and a substrate [1], micro-ultrasonic cleaving of a chunk of cells [8], stone fragmentation [1], drug delivery [20], controlled generation of a single micro-bubble [15], and nozzle-free liquid micro-jetting [89]. For these applications, acoustic cavitation under LGFU plays a central role of enabling mechanical micro-erosion of solid materials and localized disruption on single cells and the tissue. It has been experimentally confirmed that LGFU-induced cavitation can be generated under a strong tensile pressure over a threshold level [15]. Moreover, the cavitation process has been fully visualized by using a laser-flash shadowgraphy [8]: *i.e.* bubble inception, growth, shrinkage, and then collapse leading to a liquid jet and secondary shockwaves.

Despite successful demonstration over various applications, a tensile pressure amplitude from photoacoustic lenses fell short of a threshold pressure level in order to produce the microscale cavitation in the middle of water without any supporting boundary such as the detector substrate and the tissue. It is challenging to produce such free-field cavitation particularly over a high-frequency ultrasound regime (*e.g.* $f > 15$ MHz), as the threshold pressure increases with $f^{1/2}$ [90]. For bubble formation, the supporting material can work essentially as a boosting reflector due to acoustic impedance mismatch, creating an enhanced pressure zone in the vicinity of the reflection plane where the incident and the reflected acoustic waves are spatio-temporally superposed. However, it is impractical to bring such supporting material (*e.g.* glass) onto a site of focal treatment, whenever required, for effective reduction of cavitation

threshold. For the tissue, the cavitation threshold significantly varies according to its composition and morphological characteristics [91]. For therapeutic applications, these issues ultimately require LGFU amplitudes strong enough to produce free-field cavitation without any supporting boundary. Recently, as an alternative method, a superposition approach has been introduced to enhance a focal pressure amplitude by spatio-temporally overlapping LGFU with additional focused ultrasound obtained from a piezoelectric transmitter [8]. Although free-field cavitation has been demonstrated by the superposition of two focal transmitters, this still shows lack of the LGFU amplitude obtained from a single-element photoacoustic lens.

In this work, we develop a photoacoustic lens with a deep spherical curvature and a low *f*-number of ~0.62 that enables high focal gain and pressure enhancement. We characterized the new lens and its output in terms of a focal profile, input laser energy *versus* output pressure strength, and LGFU-induced cavitation. Significant reduction in the cavitation threshold was observed on the solid boundary as compared to those reported previously using lenses with *f*-numbers > 0.9 [1]. In terms of a pulse laser energy (*E*) to generate the pressure, only 1.5 mJ/pulse was required to reach the pressure threshold for cavitation (*cf.* 10~12 mJ for previous lenses). Then, we demonstrate free-field cavitation in water. By counting a cavitation event per a single pressure pulse, we determined a cavitation probability quantitatively. The progress in this work shows that an LGFU amplitude can be increased up to a level sufficient for free-field cavitation by a single-element photoacoustic lens. The increased pressure strength also implies that high-precision treatment by LGFU can be extended over a deeper region.

6.2 High Focal Gain

A frequency-dependent geometrical gain of the acoustic lens (G) was consi dered as a major design factor to achieve tight focusing. The gain (*i.e.* a ratio of the focal pressure to the surface pressure) can be represented by [92]:

$$G = \frac{2\pi f}{c_0} r\left(1 - \sqrt{1 - \frac{1}{4f_N^2}}\right) \tag{6.1}$$

where f, c_0, r, and f_N are the acoustic frequency, the sound speed, the radius of curvature, and the f-number, respectively. Here, we defined the f-number approximately as a ratio of the radius-of-curvature (instead of using an exact focal length) to the diameter of lens aperture.

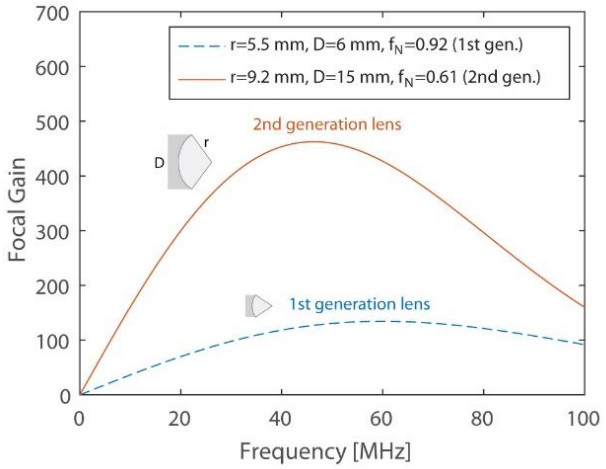

Fig. 6.1 (a) Frequency-dependent focal gain for optoacoustic lenses (calculation) and (b) experimental schematic for LGFU characterization. In (a), the gain spectrum of the new lens is compared with that of the previous lens used in [1].

Our lens was designed to have f_N =0.62 that is significantly smaller than those used in typical HIFU transducers (f_N = 2–3) and even smaller than those used in other works (f_N = 0.92 and 0.96) [1,6,20]. We multiplied the above geometrical gain G with the acoustic attenuation coefficient in water (2.2×10^{-3} dB/(cm MHz^2)) in order to estimate an effective focal gain (G_{eff}). Figure 6.1(a) shows the effective focal gain versus the acoustic frequency. Two gain curves were compared: one for the current photoacoustic lens with f_N = 0.62 and the other for the previous lens with f_N = 0.92. The lens with f_N = 0.62 exhibits a 4-fold higher focal gain than the previous one over a frequency spectral range of 0–40 MHz. Our major interest is placed over 5–30 MHz corresponding to the 6-dB bandwidth from the characteristic center frequency of LGFU (15 MHz). With the current lens (f_N = 0.62), we could achieve a high gain of $G_{eff} \approx 220$ at 15-MHz frequency while the previous design just allowed $G_{eff} \approx 54$.

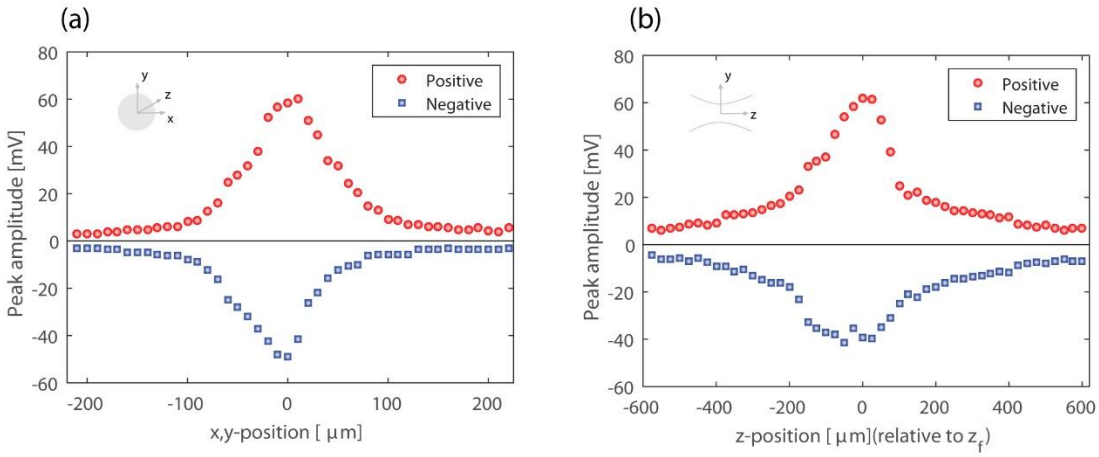

Fig. 6.2 Experimental characterization of LGFU. Peak pressure amplitudes (positive and negative) are measured and plotted (a) along the lateral and (b) the longitudinal axis.

For a frequency regime of >40 MHz, the acoustic attenuation starts to dominate the gain effect for both lenses. We characterized a focal spot profile by scanning the fiber-optic hydrophone at the focal zone (10-μm interval for the lateral characterization and 20-μm for the longitudinal) to measure pulsed ultrasound waveforms and determine peak pressure amplitudes at each position (Fig. 6.2(a) and (b)). A 6-dB focal spot width for the positive amplitude was 90 and 200 μm along the lateral (Fig. 2(a)) and the longitudinal axis (Fig. 6.2(b)), respectively. A ratio of the lateral to the longitudinal spot width (σ) was 90/200 ≈ 0.45 that is significantly larger than those of the high *f*-number lenses: σ = 0.19 (≈ 75/400) for f_N = 0.92 and σ = 0.15 (≈ 100/650) for f_N = 0.92 and 0.96. The increased ratio means that the focal spot is less elongated to the axial direction, and the shape is close to a sphere.

Figure 6.3(a) shows the efficiency of focused ultrasound generation in terms of the peak pressure amplitude versus the incident laser energy (*E*).

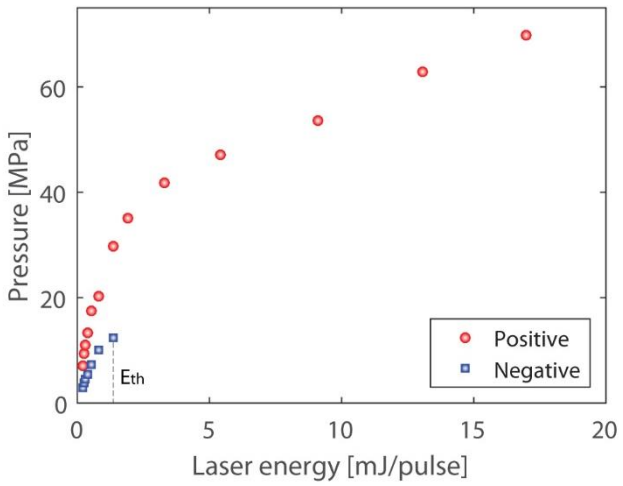

Fig. 6.3 Peak pressure amplitudes (positive and negative) versus the incident laser energy.

For low-energy optical excitation (E < 1 mJ/pulse), the positive peak pressure was linearly increased with a slope of ~20 MPa/mJ, and the negative peak pressure with a slope of ~10 MPa/mJ. The asymmetry in the peak amplitudes is due to nonlinear propagation of the pulsed waveform that leads to shock formation in the positive phase and an elongated trailing edge in the negative phase. Note that the nonlinear behavior appeared with a very low-energy input of E < 1 mJ/pulse as compared to the cases of other LGFU waveforms. In this laser energy regime, symmetric bipolar waveforms were obtained in the previous work [1], which is close to the time-derivative of an original Gaussian pulse shape [17]. This is due to tighter geometric focusing of our photoacoustic lens than the previous one, thus leading to nonlinear distortion in a lower optical energy regime.

6.3 Free-field Cavitation by Optoacoustic Transmitter with High Focal Gain

6.3.1 Shadowgraphs of boundary-free cavitation

We generated free-field cavitation without any supporting boundary in water. As shown in Fig. 6..4(a), free-field micro-bubble images were captured at different temporal moments by using the laser-flash shadowgraphy technique. Due to the high-contrast image acquisition, we could clearly determine the size of the bubble in each moment (Fig. 6.4(b)). At E = 14 mJ/pulse, the single micro-bubble was instantaneously produced upon

the arrival of LGFU which is simultaneously confirmed by the hydrophone signal. Then, the bubble grew, shrank, and then collapsed. The first image in Fig. 6.4(a) was obtained 1 μs after the LGFU had passed through the focus; it took only 1 μs for the bubble growth up to 18-μm radius. The growth process continued as shown by a series of images (Fig. 6.4(a)) together with the corresponding dimension marked in Fig. 6.4(b). In this example, the single micro-bubble prolonged during ~9 μs before its collapse.

6.3.2 Characterization of acoustic pulses by optoacoustic lens with high focal gain

We characterized on-boundary cavitation behaviors in detail by directly monitoring acoustic disturbance on the fiber-optic hydrophone and also by using a separate piezoelectric transducer in a passive manner.

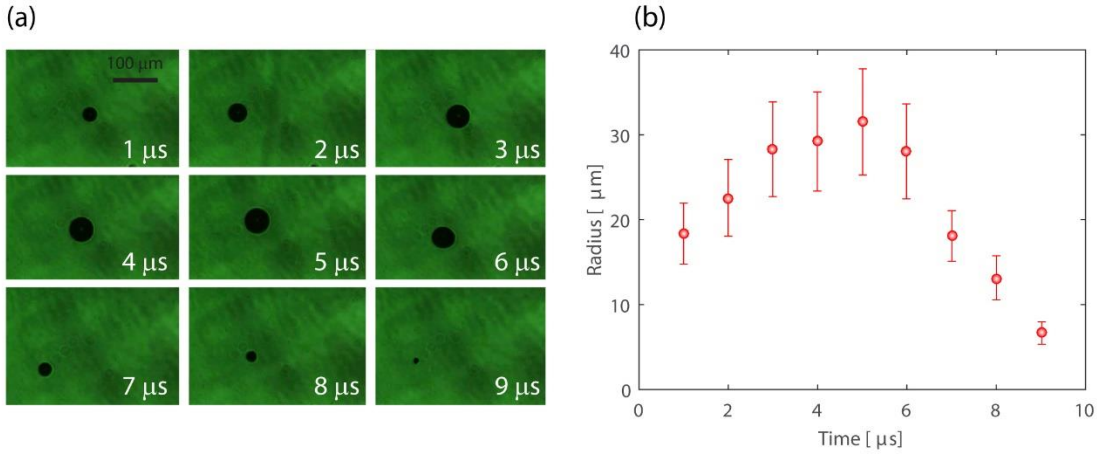

Fig. 6.4 (a) Free-field cavitation images obtained by high-speed laser-flash shadowgraphy (laser energy = 14 mJ/pulse; scale bar = 100 μm). The series of shadowgraphs show the process of bubble growth and shrinkage; (b) Micro-bubble radius measured from (a).
The maximum radius was obtained around 5 μs, which is approximately 31 μm (±6 μm).

Figure 4.5(a) shows a transient cavitation signal measured directly by the fiber-optic hydrophone. The measured transient signal is composed of an LGFU pulse immediately followed by cavitation-induced transients (labelled as Osc1 and Osc2). The duration bet ween bubble nucleation and the first collapse was denoted as 'OSC1', and the dur ation between the first and the second collapse by 'OSC2'. The pulsed LGFU signal is obtained by modulation in water density and then the refractive index at the fiber/water interface. The cavitation transients are produced by the disturbance of micro-bubbles bounded on the surface of the fiber-optic hydrophone (*i.e.* the core surface of the single-mode fiber).

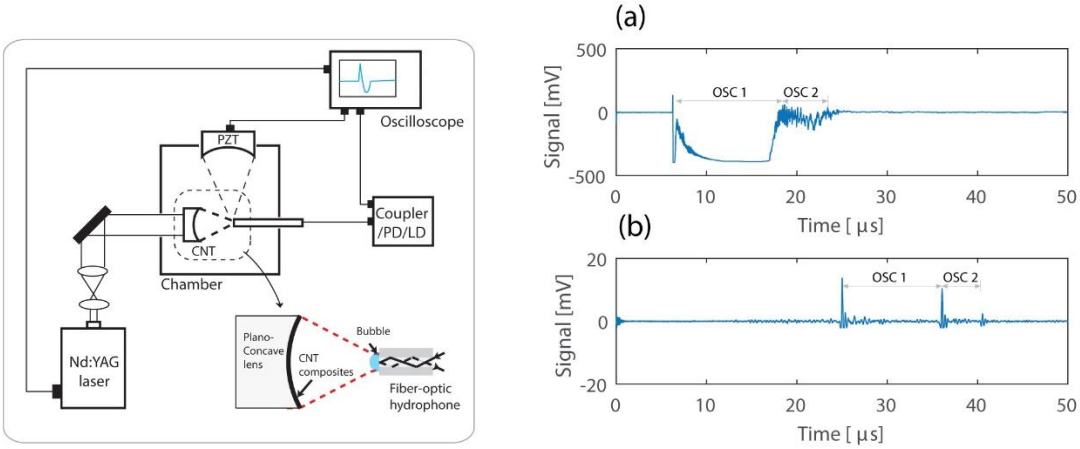

Fig. 6.5 In (b), the fiber-optic hydrophone tip was aligned to the focal point. The piezoelectric transducer (PZT) shown on the top is used to monitor on-boundary cavitation on the fiber surface (when the fiber-optic hydrophone is placed at the focus) and free-field cavitation (after the hydrophone is removed from the focal zone). Measurement of on-boundary cavitation (i.e. micro-bubbles are bound on the surface of fiber-optic hydrophone): (a) Transient cavitation signal measured directly by the fiber-optic hydrophone; (b) The same cavitation effect monitored by the piezoelectric transducer located away from the focal zone.

The latter aspect allows us to extract the bubble lifetime in terms of a temporal interval from the inception to the collapse. As the free-boundary bubbles are known to oscillate over time (repetition of growth and collapse) [20], two types of oscillations (Osc1 and Osc2) were observed in this study. A temporal period of the first oscillation (Osc1) was formed immediately after the negative peak pressure, which is followed by the second one (Osc2). As shown in Fig. 4.5(a), the second oscillation cycle (11 μs) was shorter than the first one (4.5 μs). This is due to the size of the second bubble that is smaller than the first one. We note that the second bubble is formed after energy loss through acoustic emission. Figure 4.5(b) shows the same cavitation effect monitored by the piezoelectric transducer located away from the focal zone. The piezoelectric transducer captured acoustic emissions from the cavitation zone. Each moment for the initial bubble inception, the first bubble collapse, and the second bubble collapse was labelled with **a**, **b**, and **c**, respectively. The bubble lifetime determined by the piezoelectric transducer (Fig. 4.5(b)) exactly agreed with the value obtained by the fiber-optic hydrophone (Fig. 4.5(a)).

The lifetime of free-field cavitation was measured with increasing the laser energy (Fig. 6.6(a)). Again, the lifetime from initial nucleation to collapse was labelled as Osc1 and then the interval between two collapse events as Osc2. As the focal pressure increases with the incident laser energy, the lifetimes (both Osc1 and Osc2) were elongated up to 11.5 and 5 μs at E = 15 mJ/pulse. The simultaneous increase of the maximum bubble radii was predicted by the Rayleigh model [72]. Then, the probability of cavitation inception (P) was determined by counting the number of cavitation

occurrence per a given number of LGFU pulses (Fig. 6.6(b)). A cavitation event per a single LGFU pulse (produced by a single laser pulse, not a pulse train) was observed by using the piezoelectric transducer. The single-pulse measurement was repeated 100 times (*i.e.* 100 pulses) for each probability point marked in Fig. 6.6(b). In our experiment, a pulse-to-pulse interval of LGFU was controlled to ~1 second, which means that a heating effect due to accumulated LGFU pulses is negligible. For LGFU excited at a low laser energy regime (E < 5 mJ), the free-field cavitation barely appeared with a few % in probability. The cavitation event was frequently observed as E > 10 mJ/pulse. The threshold for free-field cavitation (defined as P = 50%) was E ~ 12 mJ/pulse.

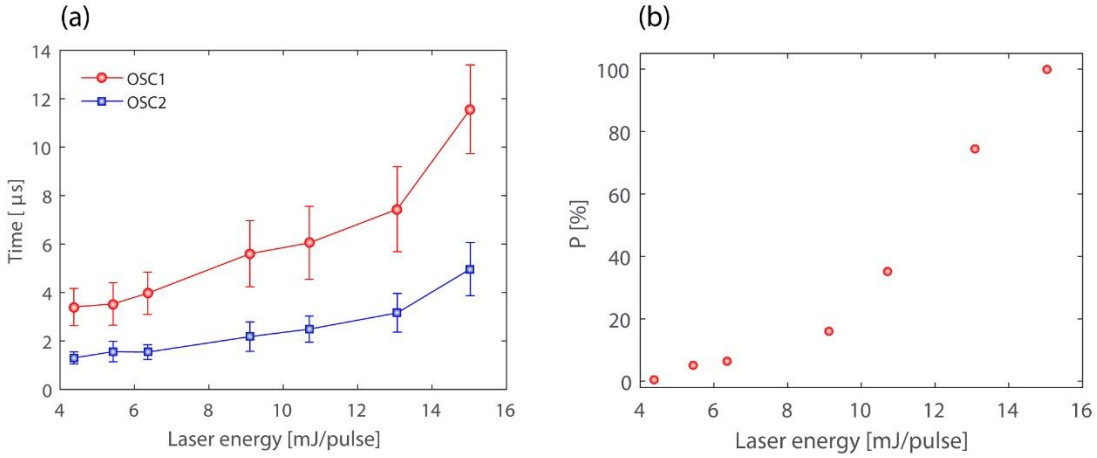

Fig. 6.6 (a) Lifetime and (b) probability of free-field cavitation measured with increasing the pulsed laser energy that is irradiated onto the optoacoustic lens. The piezoelectric transducer was used to measure the cavitation-induced transients: (a) The duration between bubble nucleation and the first collapse is denoted by 'OSC1', and the duration between the first and second collapse by 'OSC2'; (b) The probability was determined by counting the number of cavitation occurrence per 100 pulses. A single pressure pulse (excited with different laser energy) was used to produce a single event of free-field cavitation. The same single-pulse experiment was repeated 100 times to determine the probability.

Then, the probability was greatly increased with higher laser energy excitation than the threshold level: P = 100 % at E ~ 15 mJ/pulse.

Our photoacoustic lens exhibited a tight focal dimension not just upon the lateral plane and along the axial direction with the geometrical ratio, σ = 0.45, which is significantly larger than σ = 0.19 and 0.15 in other lenses with f_N = 0.92 and 0.96. For typical piezoelectric HIFU transducers, the ratio is even lower than 0.15. In addition, low MHz frequency operation leads to axial elongation in the spot shape over a few cm. This means that our lens is suitable for micro-ultrasonic treatment on a thin tissue layer with a few 100 μm thickness, greatly reducing unwanted damage over the surrounding region.

Our measurement shows that the threshold pressure for free-field cavitation is reasonably predictable from the on-boundary condition. At the onset of on-boundary cavitation (E = 1.5 mJ/pulse), the LGFU amplitude was 30 MPa for the peak positive and ~13 MPa for the peak negative (*i.e.* the measurable maximum tensile pressure just below the cavitation threshold). The cavitation threshold pressure agrees with the measured value elsewhere [1]. Note that the hydrophone detects the incident pressure only, while the cavitation is essentially formed by the spatio-temporal superposition of the incident and reflected LGFU (*i.e.* by almost doubled pressure amplitude) at a region slightly away from the reflection boundary [89]. Thus, without such hard boundary, free-field cavitation in water would require >26 MPa in the peak negative. In our experiment, the free-field cavitation required E = 12 mJ/pulse to produce LGFU with the peak positive of ~60 MPa (*i.e.* two folds of 30 MPa at E = 1.5 mJ/pulse) and then the estimated peak

negative of ~26 MPa by doubling the negative pressure at E = 1.5 mJ/pulse. This estimated threshold (26 MPa) agrees with a typical threshold level obtained in water [61].

6.4 Targeted Therapy of Animal Eyes by Boundary-free Caviation

The maximum bubble size is approximately 40 μm, which means that the minimum treatment spot should be less than the bubble diameter. As illustrated in Fig. 6.7(a), a tissue-mimicking gel is used as a test sample and the sample is scanned with respect to the fixed acoustic beam. Figure 6.7 shows cutting of tissue-mimicking gel with a thickness of 1 mm. After cutting, three dimensional shapes are removed from the gel. This approach is useful for cutting unwanted tissues and thus removing them.

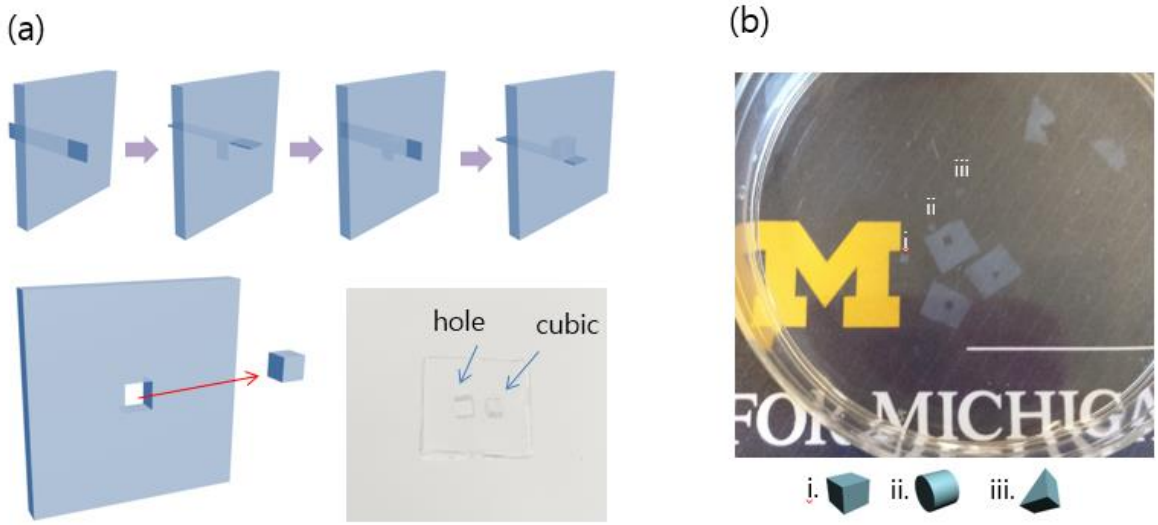

Fig 6.7 (a) Illustration of ultrasound-induced cutting. (b) Cutting of tissue mimicking gels with a thickness of 1 mm for shapes (cube: 1 mm in length, cylinder: 1 mm in diameter, and triangular prism: 1 mm in side length).

Figure 6.8 shows volumetric treatment that is realized by scanning a volume in stead of a surface. The scan region of x, y, and z direction are 0.5, 0.5, and 3 mm, respectively such that the treatment zone becomes sizable. First, the scan is carried in x-y plan for a specific z, which is repeated for the z range. Figure 6.8(b) shows the microscope images of the transparent gel after the ultrasound treatment. For a relatively large interval (∆x, ∆y, and ∆z=100 μm), as illustrated in Fig. 6.8(a), the treatment region is observed to consist of numerous holes.

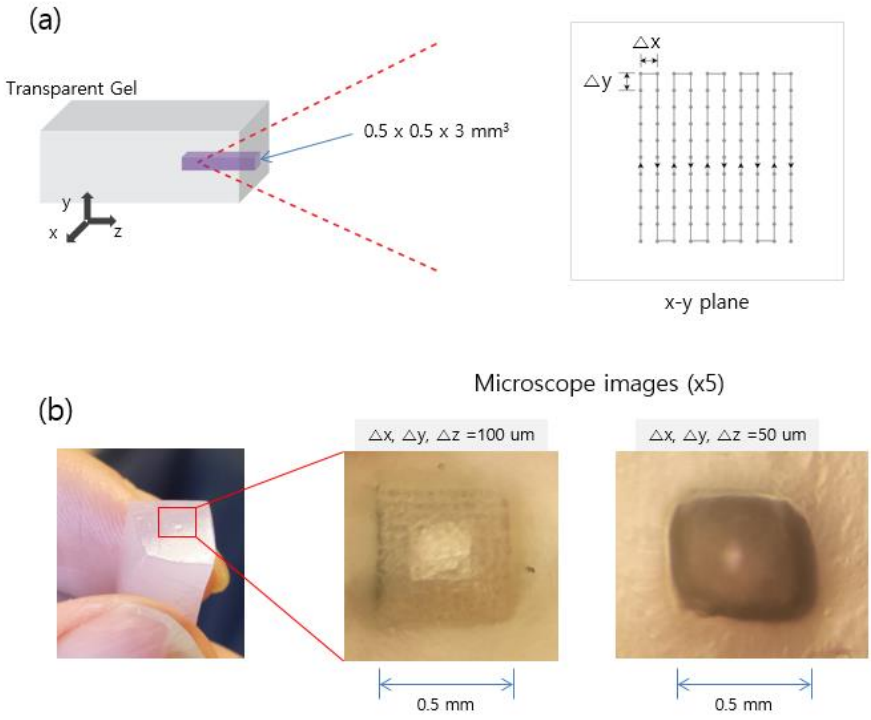

Fig. 6.8 (a) Transparent, tissue-mimicking gel is controlled by a three-axis motorized stage. The scan ranges of x, y, and z direction are 0.5, 0.5, and 3 mm, respectively. The scan is carried in x-y plan for a specific z. (b) The treated spot (0.5 x 0.5 mm^2) of the transparent gel. The magnified images show different scaning interval: a relatively large interval (∆x, ∆y, and ∆z=100 μm) and a small interval (∆x, ∆y, and ∆z=50 μm).

This is because the interval is large compared to the maximum bubble diameter. For moderate interval (Δx, Δy, and Δz=50 μm), the treatment is very effective, showing the ablated region.

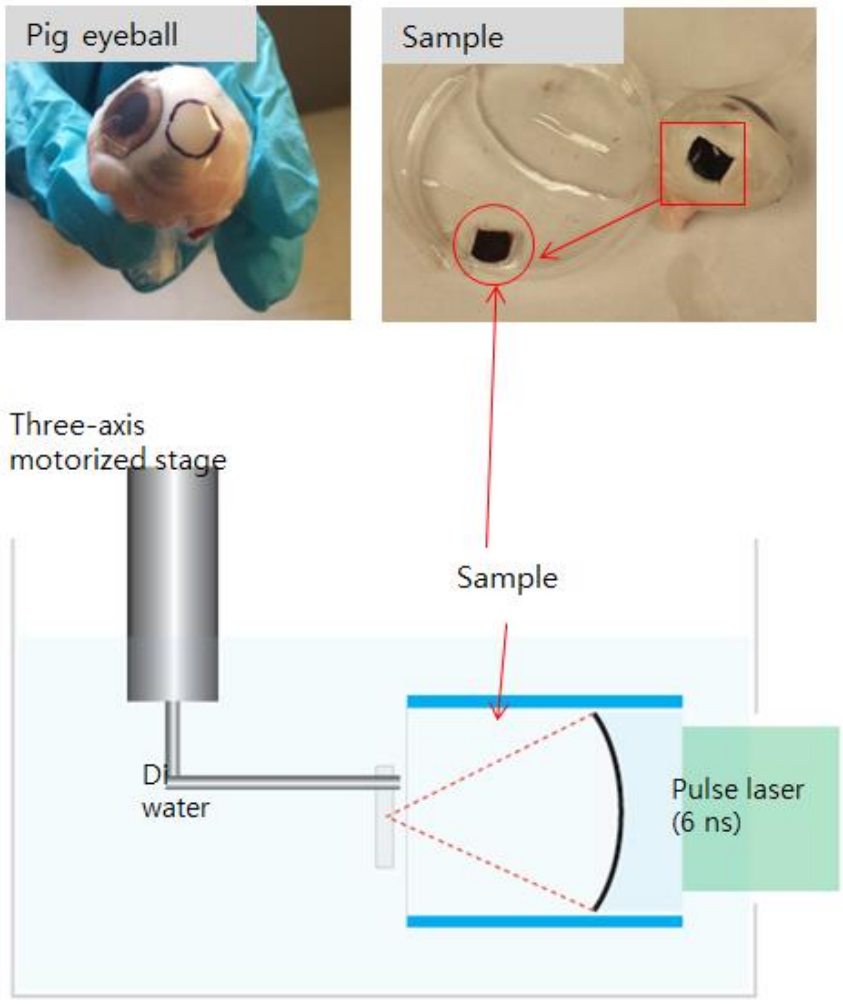

Fig. 6.9 Cavitation treatment for pig eye. The piece samples, obtained from pig eyeball, are mounted in a three-axis stage.

The pig eye is carefully cut into pieces which are then mounted to a three-axis motorized stage (Fig. 6.9). The sample consists of the thick white layer (sclera, a few millimeter) and the very thin black layer, where tumors start to grow. The sliced samples make it easy to mount and scan them.

Two square marks are observed after the cavitation treatment, as shown in Fig. 6.10. The marks are rarely identified until the sample is completely dried. By applying the acoustic wave directly to the black layer [Fig. 6.10(a)], the marks (0.5 x 0.5 mm^2) are carved at the laser energy same as that used in the gel experiment (E = 15 mJ/pulse). This experiment condition is not realistic, since the acoustic wave should penetrate through the thick white layer (sclera).

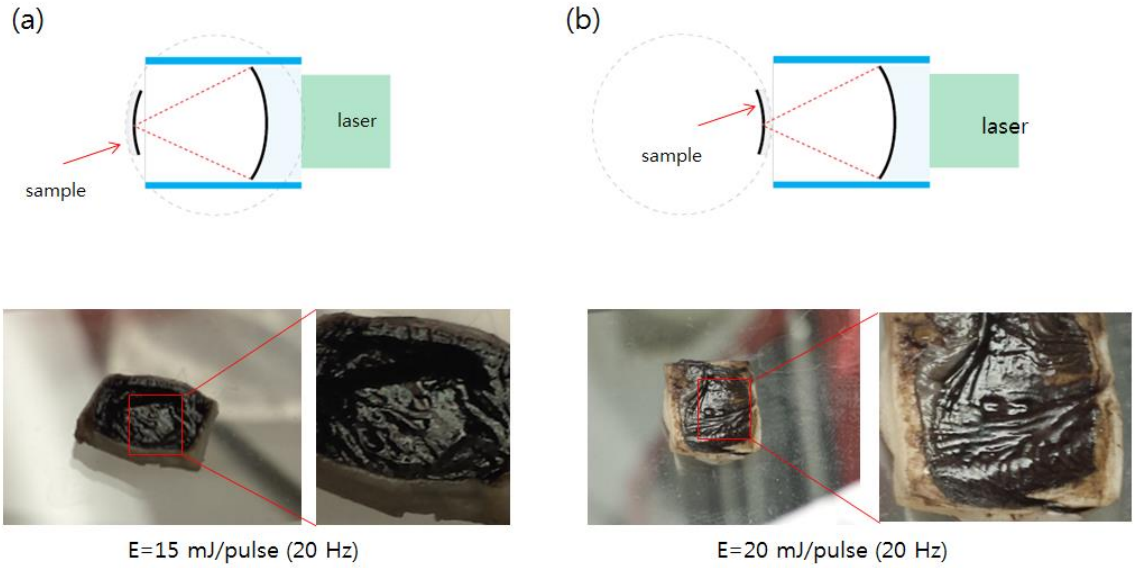

Fig. 6.10 Cavitation treatment for pig-eye samples. (a) Acoustic wave directly applied to the black layer at E = 15 mJ/pulse. (b) Acoustic wave passing through the white shell (sclera) to the black layer, requiring slightly higher laser energy (E = 20 mJ/pulse)

As shown in Fig. 6.10(b), the marks are made by using a slight high laser energy E = 20 mJ/pulse, because a thick layer of the sclera could cause sound reflection and attenuation.

6.5 Conclusion

We developed a low *f*-number photoacoustic lens that was designed to have a high effective focal gain of 220 at 15-MHz frequency. The lens allowed tight focusing not just upon the lateral plane but also along the longitudinal axis; each 6-dB focal width was 90 and 200 μm, respectively. The tight focal confinement together with the high geometric gain led to strong pressure amplitudes of 20 MPa in peak positive and 10 MPa in peak negative achieved with a very low laser energy of E = 1 mJ/pulse (also, 50 MPa (positive) with E = 7.5 mJ/pulse, and 70 MPa (positive) with E = 17 mJ/pulse). Due to the enhanced focal pressure, we could generate LGFU-induced cavitation on the detector boundary by using only E ~ 1.5 mJ/pulse. More importantly, free-field cavitation was even generated in water without any supporting boundary. Controllable cavitation with the probability of 50 % was realized at E ~ 12 mJ/pulse and 100 % at E ~ 15 mJ/pulse. Our characterization for the focal profile and the cavitation behaviors including threshold requirement provides useful information to develop photoacoustic lenses with various geometrical designs.

The LGFU system was applied to tissue therapy based on mechanical destruction, similar to histotripsy. After passing through the animal eyes, focused ultrasound is strong enough to produce cavitation. We confirmed the ablation of the eyes in a precise manner.

CHAPTER 7

Concluding Remarks and Suggestions for Future Work

7.1 Concluding Remarks

First, we have shown a polymer-metal film composite consisting of a thin metal absorber and adjacent transparent polymer layers. The proposed structure shows efficient photoacoustic conversion, which is comparable to those of the polymer-based composites containing light absorbing carbon fillers such as carbon black, carbon nanotube, and carbon fiber. The enhanced photoacoustic conversion is accomplished by reducing metal film thickness down to a few tens of nanometers and thus facilitating heat transfer from the metal film to the surrounding polymers. This work could show a design principle for a highly efficient optoacoustic transmitter.

Second, we have investigated the phase cancellation of photoacoustic pulses that is important for understanding photoacoustic generation. This cancellation effect has been overlooked, which could be critical under certain cases, e.g, planar absorbers subject to an air-backed boundary condition, two- and three- dimensional absorbers. This study could allow better understanding of photoacoustic generation. Moreover, we have demonstrated anomaly acoustic phase shift by focusing a short photoacoustic pulse (< 100 ns). After passing through focus, the polarity of a photoacoustic pulse is reversed. Also, we tried to provide an intuitive explanation of the phase shift. This observation

could benefit the understanding of the Gouy phase shift, which is poorly understood in optics.

Third, we have examined the interaction between a focused photoacoustic pulse and impedance mismatched interfaces. Photoacoustic pulses reflect from the impedance interfaces, and interfere with the rest of the incoming pulse. The interfered photoacoustic field varies depending on the acoustic impedance of the interfaces. For a sound hard boundary, controlled bubble generation, rather insensitive to surface heterogeneity, was demonstrated for potential applications, e.g., surface cleaning. On the other hand, for a sound soft boundary, nozzle-free liquid micro-jetting was demonstrated for applications, e.g., printing and drug injection.

Last, we show controlled cavitation and its application to targeted therapy by using a focused photoacoustic pulse. By employing a concave lens coated by an efficient optoacoustic composite, we are capable of producing high-amplitude acoustic pressure at a tight focal spot (<100 um). The small focal spot, comparable to cavitation zone, lead to controllable cavitation treatment. Also, the compact optoacoustic lens is good for treating small samples such as eyeballs.

7.2 Suggestions for Future Work

7.2.1 Metal-based photoacoustic contrast agent and photoacoustic pattern

We have demonstrated a highly efficient thin metal film-polymer composite by

facilitating heat transfer from a thin metal absorber to the adjacent polymer layers (see Chapter 2). This approach could be applicable for designing photoacoustic contrast agent. One possible route is to use metal nanoparticles coated with polymers. We can choose materials based on the Figure of Merit.

Metal-based photoacoustic pattern can be implemented in applications, e.g., photoacoustically guided insertion of a needle. By integrating the metal-based composite to the needle, we can monitor the needle deeply positioned in biological tissues, while using a laser fluence lower than the American National Standards Institute (ANSI) safety limit (20 mJ/cm^2).

7.2.2 Air-backed photoacoustic transmitter for strong monopolar pulse

Phase cancellation is responsible for significantly reduced photoacoustic amplitudes (see Chapter 3) for a planar absorber subject to an air-backed boundary (or sound soft boundary). However, the air-backed boundary can be used for producing a photoacoustic pulse with a monopolar shape. By mitigating the phase cancellation through the matching layer, a strong, monopolar photoacoustic pulse can be generated.

The planar air-backed transmitter can be extended to a focusing transmitter for monopolar pulses. This focused monopolar pulse (high negative pressure amplitude) could be utilized for cavitation therapy. It is known to be that the negative phase (or tensile component) induces cavitation. However, our current photoacoustic transmitters produce a bipolar pulse consisting of a leading positive phase and a following negative

phase; the positive phase is approximately twice larger than the negative phase. Thus, the strong monopolar pulse might be much effective in cavitation therapy, because the positive phase (compressive component) can cause unwanted mechanical damages.

7.2.3 Photoacoustic transmitter-integrated endoscope for cavitation therapy

The focused photoacoustic approach shows promise in targeted treatment (see Chapter 6). It would be very useful that this approach is combined with endoscopes. While conducting endoscopic imaging, we can simultaneously treat diseased tissues and cells. However, this approach could be challenging, because small photoacoustic transmitters (< 3 mm) are required to be integrated to endoscopes. If scaling down the photoacoustic transmitters, the focal gain is significantly reduced, thus decreasing photoacoustic pressure amplitudes. This challenge calls for more efficient photoacoustic transmitters. One possible way to address this challenge is that the damage threshold (or mechanical robustness) needs to be further increased for allowing much higher input optical energy, thus increasing the maximum achievable photoacoustic amplitudes.

References

[1] H. W. Baac, J. G. Ok, A. Maxwell, K. T. Lee, Y. C. Chen, A. J. Hart, Z. Xu, E. Yoon, and L. J. Guo, Scientific Reports **2**, 989 (2012).
[2] D. M. McCann and M. C. Forde, Ndt & E International **34**, 71 (2001).
[3] X. D. Wang, Y. J. Pang, G. Ku, X. Y. Xie, G. Stoica, and L. H. V. Wang, Nature Biotechnology **21**, 803 (2003).
[4] M. H. Xu and L. H. V. Wang, Review of Scientific Instruments **77**, 041101 (2006).
[5] T. Buma, M. Spisar, and M. O'Donnell, Applied Physics Letters **79**, 548 (2001).
[6] H. W. Baac, J. G. Ok, H. J. Park, T. Ling, S. L. Chen, A. J. Hart, and L. J. Guo, Applied Physics Letters **97**, 234104 (2010).
[7] B.-Y. Hsieh, J. Kim, J. Zhu, S. Li, X. Zhang, and X. Jiang, Applied Physics Letters **106**, 021902 (2015).
[8] H. W. Baac, T. Lee, and L. J. Guo, Biomedical Optics Express **4**, 1442 (2013).
[9] C. C. Coussios, C. H. Farny, G. Ter Haar, and R. A. Roy, International Journal of Hyperthermia **23**, 105 (2007).
[10] C. C. Coussios and R. A. Roy, Annual Review of Fluid Mechanics **40**, 395 (2008).
[11] Z. Xu, T. L. Hall, J. B. Fowlkes, and C. A. Cain, Journal of the Acoustical Society of America **122**, 229 (2007).
[12] Z. Xu, M. Raghavan, T. L. Hall, C. W. Chang, M. A. Mycek, J. B. Fowlkes, and C. A. Cain, Ieee Transactions on Ultrasonics Ferroelectrics and Frequency Control **54**, 2091 (2007).
[13] D. W. Ball, Spectroscopy **21**, 14 (2006).
[14] L. V. Wang, *Photoacoustic Imaging and Spectroscopy* (CRC Press, 2009).
[15] T. Lee, H. W. Baac, J. G. Ok, H. S. Youn, and L. J. Guo, Physical Review Applied **2** (2014).
[16] K. Maslov, H. F. Zhang, S. Hu, and L. V. Wang, Optics Letters **33**, 929 (2008).
[17] G. J. Diebold, T. Sun, and M. I. Khan, Physical Review Letters **67**, 3384 (1991).
[18] R. J. Colchester, C. A. Mosse, D. S. Bhachu, J. C. Bear, C. J. Carmalt, I. P. Parkin, B. E. Treeby, I. Papakonstantinou, and A. E. Desjardins, Applied Physics Letters **104**, 173502 (2014).
[19] S. H. Lee, M.-a. Park, J. J. Yoh, H. Song, E. Y. Jang, Y. H. Kim, S. Kang, and Y. S. Yoon, Applied Physics Letters **101**, 241909 (2012).
[20] H. W. Baac, J. Frampton, J. G. Ok, S. Takayama, and L. J. Guo, Journal of Biophotonics, 6 (2013).
[21] T. Mitcham, K. Homan, W. Frey, Y.-S. Chen, S. Emelianov, J. Hazle, and R. Bouchard, Journal of Biomedical Optics **18**, 056008 (2013).
[22] D. Kim, M. Ye, and C. P. Grigoropoulos, Applied Physics a-Materials Science & Processing **67**, 169 (1998).
[23] V. E. Gusev and A. A. Karabutov, *Laser Optoacoustics* (American Institute of Physics, New York, 1993).
[24] J. H. Bechtel, Journal of Applied Physics **46**, 1585 (1975).
[25] C. K. N. Patel and A. C. Tam, Reviews of Modern Physics **53**, 517 (1981).
[26] A. C. Tam, Reviews of Modern Physics **58**, 381 (1986).
[27] S.-L. Chen, Y.-C. Chang, C. Zhang, J. G. Ok, T. Ling, M. T. Mihnev, T. B. Norris, and L. J. Guo, Nature Photonics **8**, 537 (2014).
[28] W.-L. Ong, S. M. Rupich, D. V. Talapin, A. J. H. McGaughey, and J. A. Malen, Nature Materials **12**, 410 (2013).
[29] G. J. Diebold, M. I. Khan, and S. M. Park, Science **250**, 101 (1990).

[30] G. J. Diebold, Review of Scientific Instruments **74**, 801 (2003).
[31] D. Kim and C. P. Grigoropoulos, Applied Surface Science **127**, 53 (1998).
[32] T. Tyc, Optics Letters **37**, 924 (2012).
[33] A. B. Ruffin, J. V. Rudd, J. F. Whitaker, S. Feng, and H. G. Winful, Physical Review Letters **83**, 3410 (1999).
[34] P. Kuzel, M. A. Khazan, and J. Kroupa, Journal of the Optical Society of America B-Optical Physics **16**, 1795 (1999).
[35] R. W. McGowan, R. A. Cheville, and D. Grischkowsky, Applied Physics Letters **76**, 670 (2000).
[36] F. Lindner, G. G. Paulus, H. Walther, A. Baltuska, E. Goulielmakis, M. Lezius, and F. Krausz, Physical Review Letters **92**, 113001 (2004).
[37] J. Hamazaki, Y. Mineta, K. Oka, and R. Morita, Optics Express **14**, 8382 (2006).
[38] N. C. R. Holme, B. C. Daly, M. T. Myaing, and T. B. Norris, Applied Physics Letters **83**, 392 (2003).
[39] A. A. Kolomenskii, S. N. Jerebtsov, and H. A. Schuessler, Optics Letters **30**, 2019 (2005).
[40] P. Hariharan and P. A. Robinson, Journal of Modern Optics **43**, 219 (1996).
[41] S. M. Feng and H. G. Winful, Optics Letters **26**, 485 (2001).
[42] D. Subbarao, Optics Letters **20**, 2162 (1995).
[43] R. Simon and N. Mukunda, Physical Review Letters **70**, 880 (1993).
[44] R. W. Boyd, Journal of the Optical Society of America **70**, 877 (1980).
[45] M. F. Hamilton, Journal of the Acoustical Society of America **92**, 527 (1992).
[46] K. E. Froysa, J. N. Tjotta, and S. Tjotta, Journal of the Acoustical Society of America **93**, 80 (1993).
[47] T. Lee, D. Jang, D. Ahn, and D. Kim, Journal of Applied Physics **107**, 033112 (2010).
[48] M. O. Lamminen, H. W. Walker, and L. K. Weavers, Journal of Membrane Science **237**, 213 (2004).
[49] K. S. Suslick, Science **247**, 1439 (1990).
[50] E. B. Flint and K. S. Suslick, Science **253**, 1397 (1991).
[51] V. Belova, D. A. Gorin, D. G. Shchukin, and H. Mohwald, Angewandte Chemie-International Edition **49**, 7129 (2010).
[52] D. G. Shchukin, E. Skorb, V. Belova, and H. Moehwald, Advanced Materials **23**, 1922 (2011).
[53] V. Belova, T. Borodina, H. Mohwald, and D. G. Shchukin, Ultrasonics Sonochemistry **18**, 310 (2011).
[54] D. F. Rivas, A. Prosperetti, A. G. Zijlstra, D. Lohse, and H. J. G. E. Gardeniers, Angewandte Chemie-International Edition **49**, 9699 (2010).
[55] P. Prentice, A. Cuschierp, K. Dholakia, M. Prausnitz, and P. Campbell, Nature Physics **1**, 107 (2005).
[56] M. Arora, C. D. Ohl, and D. Lohse, Journal of the Acoustical Society of America **121**, 3432 (2007).
[57] N. Bremond, M. Arora, C. D. Ohl, and D. Lohse, Physical Review Letters **96**, 224501 (2006).
[58] B. M. Borkent, S. Gekle, A. Prosperetti, and D. Lohse, Physics of Fluids **21**, 102003 (2009).
[59] B. A. Rabkin, V. Zderic, and S. Vaezy, Ultrasound in Medicine and Biology **31**, 947 (2005).
[60] W. W. Roberts, T. L. Hall, K. Ives, J. S. Wolf, J. B. Fowlkes, and C. A. Cain, Journal of Urology **175**, 734 (2006).
[61] A. D. Maxwell, C. A. Cain, A. P. Duryea, L. Q. Yuan, H. S. Gurm, and Z. Xu, Ultrasound in Medicine and Biology **35**, 1982 (2009).

[62] E.-A. Brujan and Y. Matsumoto, Microfluidics and Nanofluidics **13**, 957 (2012).
[63] G. N. Sankin and V. S. Teslenko, Doklady Physics **48**, 665 (2003).
[64] M. L. Calvisi, J. I. Iloreta, and A. J. Szeri, Journal of Fluid Mechanics **616**, 63 (2008).
[65] C. E. Brennen, (Oxford University Press, 1995).
[66] J. D. Bernardin and I. Mudawar, Journal of Heat Transfer-Transactions of the Asme **124**, 864 (2002).
[67] H. G. Flynn, Journal of the Acoustical Society of America **58**, 1160 (1975).
[68] A. A. Atchley and A. Prosperetti, Journal of the Acoustical Society of America **86**, 1065 (1989).
[69] N. Bremond, M. Arora, S. M. Dammer, and D. Lohse, Physics of Fluids **18**, 121505 (2006).
[70] X. Zeng, X. L. Mao, R. Greif, and R. E. Russo, Applied Physics a-Materials Science & Processing **80**, 237 (2005).
[71] H. Chen, X. J. Li, M. X. Wan, and S. P. Wang, Ultrasonics **49**, 289 (2009).
[72] Rayleigh, Philosophical Magazine **34**, 94 (1917).
[73] S. Mitragotri, Nature Reviews Drug Discovery **5**, 543 (2006).
[74] M. R. Prausnitz and R. Langer, Nature Biotechnology **26**, 1261 (2008).
[75] F. Torrisi *et al.*, Acs Nano **6**, 2992 (2012).
[76] G. Percin, T. S. Lundgren, and B. T. Khuri-Yakub, Applied Physics Letters **73**, 2375 (1998).
[77] T.-H. Han and J. J. Yoh, Journal of Applied Physics **107**, 103110 (2010).
[78] D. A. Fletcher and D. V. Palanker, Applied Physics Letters **78**, 1933 (2001).
[79] P. H. Chen, W. C. Chen, and S. H. Chang, International Journal of Mechanical Sciences **39**, 683 (1997).
[80] A. Antkowiak, N. Bremond, S. Le Dizes, and E. Villermaux, Journal of Fluid Mechanics **577**, 241 (2007).
[81] S. Gekle, J. Manuel Gordillo, D. van der Meer, and D. Lohse, Physical Review Letters **102**, 034502 (2009).
[82] Y. Tagawa, N. Oudalov, C. W. Visser, I. R. Peters, D. van der Meer, C. Sun, A. Prosperetti, and D. Lohse, Physical Review X **2**, 031002 (2012).
[83] S. A. Elrod, B. Hadimioglu, B. T. Khuriyakub, E. G. Rawson, E. Richley, C. F. Quate, N. N. Mansour, and T. S. Lundgren, Journal of Applied Physics **65**, 3441 (1989).
[84] S. T. Thoroddsen, K. Takehara, T. G. Etoh, and C. D. Ohl, Physics of Fluids **21**, 112101 (2009).
[85] A. Patrascioiu, J. M. Fernandez-Pradas, J. L. Morenza, and P. Serra, Applied Surface Science **302**, 303 (2014).
[86] A. Patrascioiu, J. M. Fernandez-Pradas, A. Palla-Papavlu, J. L. Morenza, and P. Serra, Microfluidics and Nanofluidics **16**, 55 (2014).
[87] Y. Tomita, P. B. Robinson, R. P. Tong, and J. R. Blake, Journal of Fluid Mechanics **466**, 259 (2002).
[88] B. Karri, S. R. G. Avila, Y. C. Loke, S. J. O'Shea, E. Klaseboer, B. C. Khoo, and C.-D. Ohl, Physical Review E **85**, 015303 (2012).
[89] T. Lee, H. W. Baac, J. G. Ok, H. S. Youn, and L. J. Guo, Physical Review Applied **3**, 044007 (2015).
[90] R. E. Apfel and C. K. Holland, Ultrasound in Medicine and Biology **17**, 179 (1991).
[91] A. D. Maxwell, C. A. Cain, T. L. Hall, J. B. Fowlkes, and Z. Xu, Ultrasound in Medicine and Biology **39**, 449 (2013).
[92] R. S. C. Cobbold, *Foundations of Biomedical Ultrasound* (Oxford University Press, 2007), 1 edn.